Experimental and Numerical Investigation of Solar Airflow Windows

Experimental and Numerical Investigation of Solar Airflow Windows

By

Kelton Friedrich, B. Mech. Eng. & Mgmt.

A Thesis

Submitted to the School of Graduate Studies

in Partial Fulfillment of the Requirements

for the Degree

Master of Applied Science

McMaster University

Hamilton, Ontario, Canada

MASTER OF APPLIED SCIENCE (2011) McMaster University

(Mechanical Engineering) Hamilton, Ontario

TITLE: Experimental and Numerical Investigation of Solar Airflow Windows

AUTHOR: Kelton Friedrich, B. Mech. Eng. & Mgmt.

(McMaster University)

SUPERVISOR: Dr. Mohamed S. Hamed

NUMBER OF PAGES: 132

Abstract

Solar thermosiphons integrated into the thermal envelop of buildings has been studied for their potential to take advantage of solar energy in heating buildings. The annual performance of solar thermosiphons cannot currently be predicted with the correlations from previous research. Also, no work has been done on the supply mode of a solar thermosiphon even though it has the potential to provide heating and fresh ventilation air. An investigation was done with the goal of developing a numerical model that could predict the performance of the supply mode of a solar thermosiphon. The numerical model included infrared thermal radiation and conduction through the glass, phenomenon which had not been used in previous numerical models. To validate the numerical model a novel steady state experiment was developed. This experiment included radiation as the heat source and the ability to vary geometric lengths. The performance parameters of mass flow rate and thermal efficiency were comparable between the numerical predictions and experimental results. However, due to uncertainties in the current experimental setup, full validation of the numerical model was not possible. These uncertainties would have to be addressed before the numerical model that was developed can be fully validated and used for generating correlations. After consideration of practical implementation constrains, it was shown that it was easier to implement the indoor air curtain mode of a solar thermosiphon than the supply mode. The indoor air curtain mode provides the same amount of energy from solar radiation to heat a building as the supply mode of a solar thermosiphon.

Acknowledgements

I would like to thank all the technicians in the department, Joe, JP, Ron, Mark and Jim for their help and advice.

I would also like to thank Michael Kish for his help in getting the experiment designed.

I also need to thank all the guys in the CFD lab, from when I started and up till now, the brainstorming really helped this work happen.

I also need to send my gratitude to Dr. Mohamed S. Hamed and Dr. Ghandi Razaqpur for their support and guidance.

I need to thank Simon Foo of Public Works and Government Services Canada for allowing this work to happen through funding.

Table of Contents

List of Tables:

List of Figures:

List of Symbols:

SYMBOL	DESCRIPTION	UNITS
A_n	Calibration coefficient	$\frac{1}{V}$
C_p	Specific heat capacity	$\frac{J}{kg^oC}$
B	Spacing between glass and absorbing wall	m
e	Measured voltage	V
E	Inlet and outlet height	m
$f()$	manufacturer provided calibration function	—
g	Gravitational acceleration	$\frac{m}{s^2}$
Gr_H	Grashof number based on wall heating	—
Gr_A	Grashof number based on air temperature	—
h	Convection heat transfer coefficient	$\frac{W}{m^{2^o}C}$
H	Total cavity height	m
k	Thermal conductivity	$\frac{W}{m^oC}$
L	Spacing between glass and illumination system	m
$\dot{m}$	Mass flow rate	$\frac{kg}{s}$
Nu_H	Nusselt number based on height	—

p	Measured atmospheric pressure	kPa
Pr	Prandtl number	—
q	Heat flux	$\frac{W}{m^2}$
r	Relative humidity	%
R	Calculated result	—
Ra_H	Rayleigh number based on height	—
Re	Reynolds number	—
$T_{@exit}$	Air temperature surrounding exit	^oC
$T_{@inlet}$	Air temperature surrounding inlet	^oC
T_{exit}	Mass flow averaged exit air temperature	^oC
T_{inlet}	Mass flow averaged inlet air temperature	^oC
T_w	Uniform temperature of wall	^oC
T_∞	Temperature of fluid far from wall	^oC
$u( )$	Uncertainty in ( )	—
V	Velocity	$\frac{m}{s}$
$\bar{V}$	Area averaged velocity	$\frac{m}{s}$
W_n	n^{th} variable	—

α	Thermal diffusivity	$\frac{m^2}{s}$
β	Thermal expansion coefficient	$\frac{1}{^oC}$
ν	Kinematic viscosity	$\frac{m^2}{s}$
μ	Dynamic viscosity	$\frac{kg}{m\,s}$
ρ	Density	$\frac{kg}{m^3}$

Chapter 1

1. Introduction

1.1 Background

The concern of human impact on the environment has become more prevalent in the past decades. It is understood that fossil fuel use has an adverse effect on the environment, and currently fossil fuels make up a considerable amount of energy used in developed countries. Buildings are known to use 40% of primary energy used in North America and western Europe documented in Natural Resources Canada's Energy Use Data Handbook (2008).

The goal of net zero energy buildings (NZEB) was seriously considered in North America in the 1970's do due the rise in oil prices. NZEB is the reduction of fossil fuel derived energy in the operation of buildings and is achieved by conservation measures or replacing fossil fuels with renewable energy sources incident on the building. With rising fossil fuel prices and the more publicized connection between fossil fuel use and climate change, achieving NZEB has become a prominent goal in building design and is the long term goal of such professional associations as the American Society of Heating, Refrigeration and Air-Conditioning Engineers (ASHRAE). Renewable technologies utilized in achieving NZEB include wind turbines, geothermal heat pumps but more commonly are passive and active solar technologies.

Active methods of utilizing solar energy incident on a building include photovoltaic electrical generation, pump driven solar hot water and hot air collection systems.

Passive technologies include shading, natural day lighting, natural ventilation and air heating. Passive air heating is the focus of this work.

It is desirable if a passive technology can make use of the solar radiation incident on a building to not only provide heating, but also supply fresh air as well. Fresh air is required as humans release carbon dioxide when they breath, and the high carbon dioxide concentration exhaled air needs to be replaced with air with a lower carbon dioxide concentration from outside. This has led to the investigation of solar thermosiphons, which can provide heating and ventilation by using buoyancy to drive the airflow through them. There are four operating modes of solar thermosiphons implemented on buildings and will be discussed in detail in the following section. A Solar Airflow Window (SAW) is able to switch between the different modes of a solar thermosiphon, so is not restricted to operating in just one mode when constructed like current solar thermosiphons. The focus of this work has been on the supply mode which can provide natural ventilation at the same time as warming air as it enters the building.

The information that is useful to implementation of SAWs in buildings is finding the performance of the system, so the potential savings can be estimated. The performance will depend on many parameters including the climate, the location on the building, the construction materials, the geometry and other factors such as mechanical ventilation and wind. The weather will change throughout the day, and from season to season, so it is not possible to use a single operating condition to indicate the yearly performance of the SAW. To have a better prediction of the performance of SAWs a year round simulation would be required that utilizes hourly weather data. Such simulations are not feasible by solving with Computational Fluid Dynamics (CFD) software as the time period is far too long, resulting in very long simulations. What is more desirable is to

have correlations relating important weather data to the performance of the SAW. In this way traditional building energy simulation software programs that do hour by hour simulations can represent a SAW as a single node, and solve the correlation by inputting the hourly weather data, and find the hourly performance. So one of the requirements is to find a correlation for a SAW performance based on weather data. With these correlations and a building energy simulation program, predictions of the annual energy saving potential can be made for SAWs used in a given building for a given location.

It is also desirable to find the optimal performance of SAWs. This will result in the fastest payback period making the SAW more feasible than operating at non-optimal performance. The climate of a given location has a great impact on the performance of a SAW and although is not controllable the climate still needs to be considered when finding the optimal performance. Other parameters that have a impact on the performance, such as the geometry and material properties are at the discretion of the designer. So there is a need to find SAW performance data for a given geometry for varying climatic conditions, so that the data can be used in a yearly building energy simulation, and thus find the optimal configuration of a SAW for a given location.

Given the time consuming nature of setting up and taking measurements with experiments, as well their variability in results, it is often much simpler to setup a numerical simulation. Changing parameters in numerical models are typically much easier to do than in experiments. This is why numerical models are often preferred to experiments. The drawback to numerical models is that without some form of validation, their results cannot be trusted as the assumptions used in the numerical model may not capture the phenomenon investigated properly.

The cumulative goal would be to have a validated numerical CFD model that would allow for a parametric study over a wide range of variables including weather, geometry, material properties and external pressure forces. From this parametric study correlations could be developed over the typical operation range. Using these correlations and hour by hour building energy simulations, accurate predictions of the system could be obtained allowing for easy comparison of energy savings with other technologies.

1.2 Types of Solar Thermosiphons

In its simplest form, a solar thermosiphon is a cavity made of two vertical parallel plates. One plate is made of a glazing material that transmits solar radiation, allowing the radiation to strike the second parallel plate, which heats up as it absorbs the radiation. Consequently, the air next to the absorbing plate is heated. This heated air then rises, as hotter air is less dense relative to colder air. This mechanism induces a thermally driven flow between the two parallel plates. Where the air is drawn in from at the bottom of the parallel plates and where the air exits at the top determines the classification of the thermosiphon. The four modes of a solar thermosiphon can be seen in Figure 1.1.

In the indoor air curtain mode, air that enters the bottom of the solar thermosiphon comes from inside the building, and exits out the top of the solar thermosiphon going back inside the building. A Trombe Wall operates in the indoor air curtain mode, and has the benefit of heating the air within the building passively. Due to this heating potential the Trombe Wall has been investigated considerably. In the outdoor air curtain mode, the air enters from the outside and exits to the outside, with the only benefit of cooling the absorbing wall. This allows the energy absorbed in summer

time to be exhausted to the outside air rather than traveling by conduction through the walls to heat the conditioned space when it is not desired. Since shading can prevent solar radiation from being absorbed in a solar thermosiphon, the outdoor air curtain mode has not be researched extensively. The exhaust mode of a solar thermosiphon is when the air enters the bottom of the cavity from the inside and exits at the top to the outside, removing air from

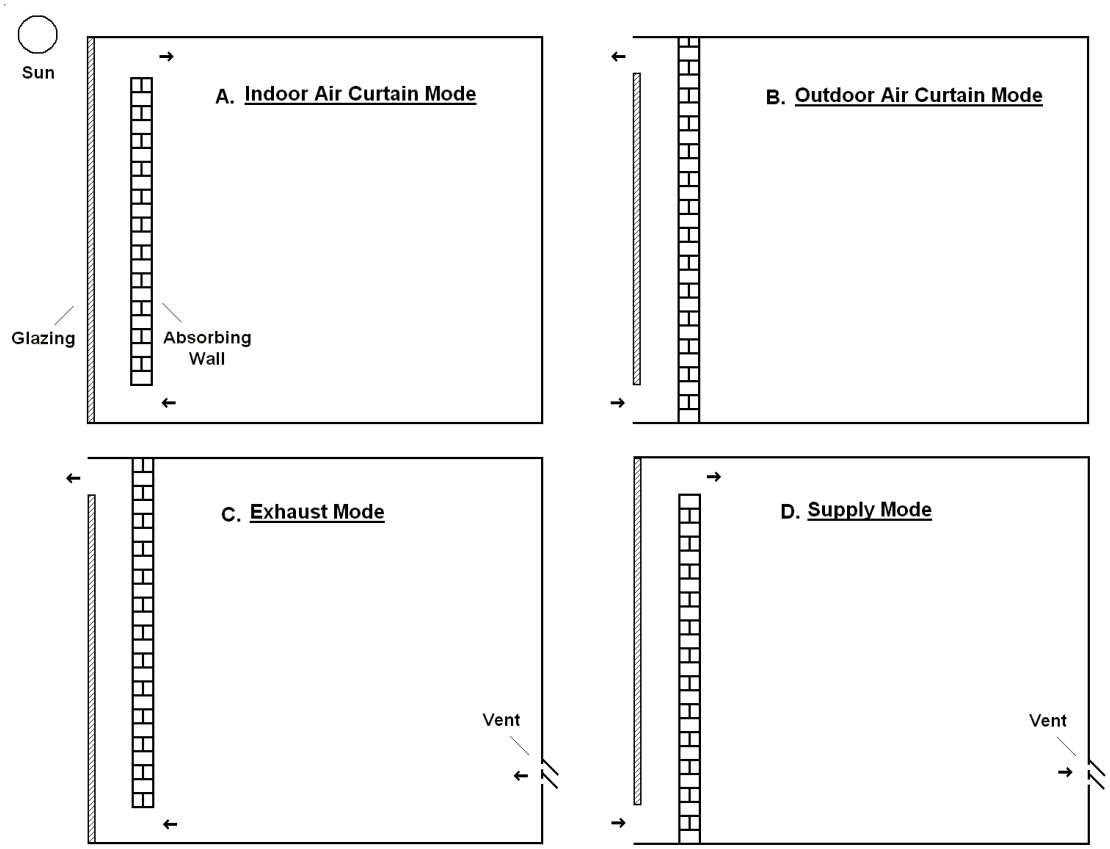

Figure 1.1: Modes of Solar Thermosiphons: A. Indoor Air Curtain, B. Outdoor Air Curtain, C. Exhaust, D. Supply

the building provided fresh air can enter the building through an inlet vent located somewhere else in the building. The solar chimney operates on this mode and has been

well studied because of the benefit of the natural ventilation it provides. The supply mode of a solar thermosiphon occurs when air enters the bottom from the outside, and exits the top into the building, again providing natural ventilation if there is an exhaust vent allowing air to leave somewhere else in the building. The supply mode offers the most benefit of all four modes as it provides natural ventilation as well as heating of the building. However, practical implementation reasons have prevented wide scale use of the supply mode, primarily that when solar radiation is not heating the system, the supply mode can run backwards cooling interior air and removing hot air out of the building.

The selecting one of the four different modes of a solar thermosiphon depends on the temperature of the outside air relative to the inside air, and if ventilation is required within the building. In the winter time when the outside air is colder than the inside air, and heating is required, the indoor air curtain and supply modes have the potential to provide heating from solar radiation, the supply mode also offers the benefit of natural ventilation. In the summer time when the outside temperature is above the desired inside temperature the solar thermosiphon cannot provide any form of cooling, so the only benefit that can be derived comes in the form of natural ventilation. The exhaust mode is best in the summer time as is provides ventilation but does not increase the temperature of the air entering the building beyond the outside temperature like the supply mode would. So depending on the climate the solar thermosiphon is used in only certain modes can offset external energy used in the building and for most climates switching modes between summer and winter is most beneficial.

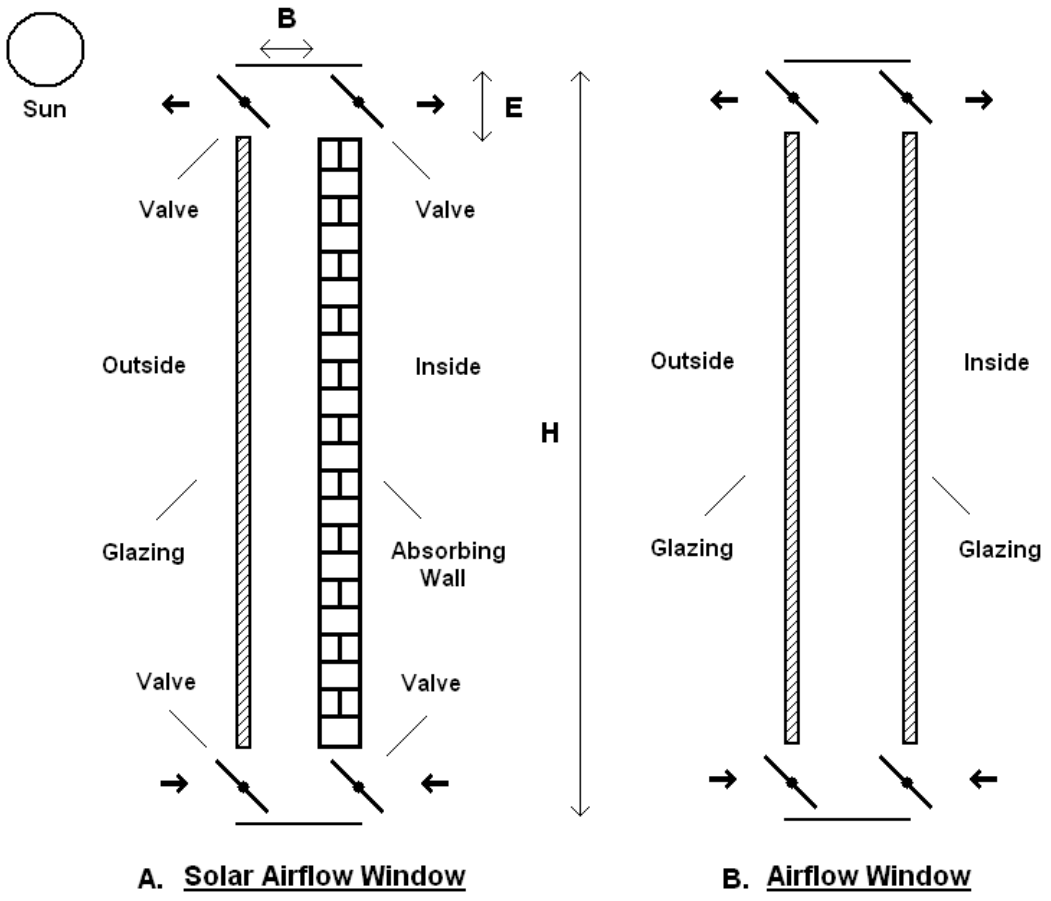

Figure 1.2: A. Solar Airflow Window, B. Airflow Window

SAW are solar building thermosiphons that can run in one or multiple operating modes, providing benefits year round instead of just in one season. A schematic of a SAW showing the valves which allow operation in all four solar thermosiphon modes can be seen in Figure 1.2 A. The focus of this study has been on the supply mode as it has the most potential, and if not otherwise stated when referring to a SAW it shall be

assumed to be operating in supply mode. Contrary to what the name implies, a SAW does not necessarily provide day lighting like a traditional window does. As with all solar thermosiphons, a glazed surface on the outside is required to let solar radiation in. So from the outside of the building the glazing, which is typically standard window glass, makes a SAW looks like a traditional window, however light does not penetrate into the occupied space as it is absorbed on the opaque wall directly behind the glass. An airflow window can be made by changing the absorbing wall to glass as seen in Figure 1.2 B. The seconded glazed surface allows light through the cavity to the inside of the building allowing the airflow window to function as a traditional window. However, by adding the second glazed surface the preheating potential of the system is greatly reduced. This makes the airflow windows unlikely to provided heated air at low radiation levels, and reduces airflow window's potential for ventilation. The benefit of day lighting from airflow windows, that cannot be provided by SAW, may out weight the loss in ventilation potential in certain applications. SAW and airflow windows can have the same heating potential in the winter time as the radiation that passes through an airflow window will be absorbed by objects in the building, heating the inside of the building. The drawback to a airflow window is that in the summer time all radiation still enters the building, heating it up when that is not the desired effect. A SAW can be switched to a mode that will vent the radiation absorbed to the outside in the summer, reducing heating in the building.

1.3 Buoyancy Effects

To understand solar thermosiphons, a understanding of the fundamental forces driving them is required. Less dense fluids have less gravitational force pulling them

down, and will rise relative to more dense fluids. The hydrostatic force acting on a fluid particle can be described by:

$$P = \rho g H$$

For solar thermosiphons, the force that drives the system can be found by comparing the hydrostatic force developed in the cavity to that developed outside of the cavity.

$$P = \Delta \rho g H$$

Gravity can be assumed to remain constant so this means the driving force in a solar thermosiphon can be controlled by changing the density difference or the height of the cavity. Air follows the ideal gas law at atmospheric pressures and temperatures, so the density of air can be reduced by increasing the temperature at the same pressure. So the hotter the air becomes in the solar thermosiphon cavity relative to the outside, the larger the pressure force will be to drive the flow through the cavity.

1.4 Pressure Drop Effects

As with any internal flow system there is resistance to flow due to friction. In forced convection what are typically called major losses, the losses from friction with fluid shearing past the cavity walls, are actually quite small in this natural convection case, as the velocities in the cavity are very small. What are called minor losses, pressure drop caused by flow converging or diverging through inlets and outlets as well as flow changing direction around bends, are larger in this natural convection case, as the number of inlets, outlets and bends is large relative to the total height of the cavity. Increasing the spacing between parallel plates, B, increases the cross sectional area.

The average velocity decreases as the cross sectional area increases. Typically the decrease in average velocity reduces the pressure drop. So the increase in cross sectional area is typically more than the reduction in average velocity so the flow rate increases with a larger B spacing. However, once a certain B spacing is reached for a given driving hydrostatic pressure, circulation within the cavity, typically starting from the inlets and outlets, becomes larger resulting in more inlet and exit pressure drop. Bigger than this B value the mass flow rate will decrease for a given driving hydrostatic pressure due to the increase in pressure drop. So the optimal B spacing for mass flow rate is defined by the combination of major and minor pressure losses that give the lowest pressure drop for the given hydrostatic pressure. The size of the inlet and outlet, E, also effects the major and minor pressure drop and like B has an optimal value for highest mass flow rate. For a given driving hydrostatic pressure both B and E would need to be optimized together to get the highest mass flow rate through the cavity.

1.5 Radiation and Optical Properties

Since the system is driven by solar radiation, radiation heat transfer will be discussed. When solar radiation strikes the outside surface of the glazing, it can be reflected, transmitted or absorbed on the surface. The relative amounts of this depend on the material properties, incident angle, and the wave length of the source radiation. The solar radiation that is reflected off the outside surface is the first source of loss in the system. The radiation that gets absorbed at the outside surface, acts as heat source at the surface, heating the glass, from here the heat can travel by conduction through the glass to the inside, or be lost by convection to the outside air or by infrared radiation to

the outside surroundings. A distinction has to be made between the solar radiation that has a much shorter wave length, and thermal radiation emitted by a surface at a much lower temperature with long wave lengths in the infrared spectrum, as optical properties can and do change for different wave lengths. Some of the solar radiation that is being transmitted through the glass, is absorbed while passing through the glass. For constant material properties this is typically a liner decrease in the transmitted radiation with the thickness of glass. This solar radiation that gets absorbed while being transmitted acts as volumetric heating in the glass. Again this heat can be conducted through the glass to the inside or outside of the glass, the later results in losses to the outside. Once the transmitted solar radiation has made its first pass through the glass it strikes the second surface, the inside of the pane of glass. Here again it can be reflected, transmitted or absorbed on the inner surface. That which is reflected is sent back though the glass, part of it being absorbed as it goes back toward the outer surface, once again acting as volume heating of the glass. Upon striking the outside surface, the same three options are available, however that which is transmitted is sent out and lost to the surroundings, and that which is reflected in sent back into the glass. It can quickly be seen that the radiation can be reflected between surfaces indefinitely. However, each pass through the glass results in some being absorbed, and not all is reflected back at the surfaces, and after a few passes back and forth the original radiation becomes dissipated till it is insignificant. The solar radiation from the first incidence on the inside surface that was absorbed as heat on the inside surface, can be transferred to the inside of the cavity by convection and infrared radiation, or travel by conduction through the glass to be lost to the outside. The solar radiation that is transmitted through the inside surface of the glass can travel uninhibited, as air does not measurably absorb or scatter solar radiation in the

small gap, to the absorbing wall. Since the absorbing wall is opaque there is only two options, one is be absorbed at the surface, the other be reflected back to the glass pane. That which is reflected from the absorbing surface is not necessarily lost, as the indefinite reflection between the absorbing wall and glass pane happen. As mentioned before it only takes a few reflections for the intensity to become negligible. The solar radiation energy that is absorbed at the absorbing surface, becomes a surface heat flux, and can either be conducted away from the surface, typically into the building, transmitted as infrared radiation to the glass plane, again not necessarily lost, or be transferred by convection to the air in the cavity which is the desired form of the energy.

As demonstrated above the solar radiation conversion to thermal energy in the form of warm air is quite complex in a single glazed solar thermosiphon. The perpetual reflections for different wave lengths make it quite tedious to find the total radiation transmitted through the glass. However, by use of geometric series and adding the effect of all the systems together the total system transmission and absorption coefficients can be found as derived in Duffie and Beckman (1974). The product of these two terms, which make up the optical efficiency, multiplied by the incident solar radiation on the outside of the glass, will give the total solar radiation that gets converted into heat at the absorbing wall. Changing the absorbing wall and glass optical properties will change the system coefficients. To improve the optical efficiency, it is better to have glass that is less reflective, more transmittance, with a low surface and volumetric absorption, and to have a high absorbing surface absorptivity. The optical efficiency results in losses that are typically larger than the losses from convection and infrared radiation off the outside of the glass. For a industry standard single 6 mm thick pane of clear float glass the system transmittance is around 0.80. Coupled with absorbing surface with an

absorptivity typically achievable with black paint of 0.90, the optical efficiency of the system is 72%, meaning a quarter of the incoming energy is lost due to optical properties. Switching to a double pane insulating glazing unit drastically reduces the conduction losses through the glazing by the addition of the air gap between the panes. However, the additional pane also adds extra reflection surfaces and glass to absorb solar radiation, reducing the system transmittance to typically 0.60. So the question becomes does the reduction in conduction losses through the glass make up for the reduction in optical efficiency for double pane windows? Given that conduction losses are temperature differential driven, and optical properties are not, only in cases where there is extreme difference between inside and outside temperatures, would the savings from reduced conduction losses overcome the reduction in optical efficiency of a double pane window.

Not only do windows optical properties depend on wave length of the incoming radiation but also on the incident angle. If not specifically mentioned the values given assume the optical properties of glass when the radiation is perpendicular to the surface, or 90^0. The reflectivity and transmittance of glass do not change from the perpendicular value much until values greater than 50^0 from perpendicular, however they change drastically after this point, with the glass becoming perfectly reflective at 90^0 from perpendicular, or when parallel to the surface. For the low attitude of the sun during the winter, south facing vertical surfaces would have incident angles less than 50^0. So it would only be in the summer time that the incident angle may become large enough to reduce the radiation entering the system.

Now that the optical properties have been discussed for the solar radiation wavelengths, the infrared radiation losses from the heated surfaces should be analysed.

Every surface emits radiation depending on temperature it is at and the emissivity. The surface temperature determines the wave length and the intensity, the emissivity determines the intensity relative to a black body surface. If the surface is surrounded by other surfaces at the same temperature, the amount of radiation emitted to the other surfaces will equal what is received from them and there will be no net transfer of heat. However, if the temperature is greater than the other surfaces, heat will be transferred from the warm surface to the cooler surfaces based on the absolute temperature to the fourth power difference. For the low absolute temperatures, and small temperature differentials, this heat transfer is very small compared to forced convection cases, and typically negligible. Natural convection heat transfer is also very small compared to forced convection, and since natural convection is the only form of convection in solar thermosiphons, neglecting wind on the outer surface, infrared radiation heat transfer is no longer negligible. In fact with low enough natural convection, radiation losses may be larger than natural convection. This is especially important when looking at the heat transfer from the warm absorbing surface to what can be the cold glass surface. The air right next to the absorbing wall is warm from being heated at the lower sections, so the temperature differential between the air and the absorbing wall may not be as large as the temperature differential driving radiation exchange between the absorbing wall and the glass. The same can also be said for the outer glass surface. Here the surface temperature of the ground and the sky can be colder than the air temperature that is in contact with the outside of the glass. The a clear sky is cooler than a cloudy sky because it does not emit radiation back. However, this infrared radiation is at a different wave length then the solar, so there can different optical properties for this radiation. Probably the most significant is the fact that glass is opaque to infrared radiation. This means that

no infrared radiation is transmitted through it. At the surface of the glass either the infrared radiation is reflected or is to be absorbed. Uncoated glass has high absorptivity in the infrared spectrum. So all losses below the solar spectrum from the inside of the cavity must be conducted through the glass, and cannot be transmitted and lost.

The difference in optical properties based on wave length can be taken advantage of by spectrally selective materials, simply meaning they have different optical properties at different wave length source radiation. Low emissivity coatings on windows are an example of these. The low emissivity coating allows solar radiation, which is at a much shorter wave length, to pass right through it, there by not effecting the solar optical properties of the glass. At the infrared wave length the coating is very reflective, and not very absorptive. As fundamentally proven in radiation heat transfer the absorptivity at a given wave length is also equal to the emissivity if the surface was to emit at that wavelength. So the low emissivity coating changes the infrared emissivity of glass, which is the wave length it would emit around room temperature, from being high to being low. So this coating will reduce the radiation heat loss off a surface that is near room temperature compared to uncoated glass. So this allows for the higher optical efficiency of glass in the solar spectrum to be maintained while reducing the infrared losses through the glass. Although the commercial application has been to apply this coating to windows, in the solar thermosiphon case, applying the coating on the absorbing surface could be just as beneficial as there would be less heat transferred from the absorbing wall to the glass that could then be lost to the surroundings.

Not to be forgotten in the heat transfer analysis is the energy absorbed on surface of the glass and also throughout the volume. As with the absorbing surface if the inside surface of the glass is warmer than the air going passed it, it will warm the air and

contribute to the useful output energy. Of course the temperature of the glass depends on the convection and radiation heat transfer on both sides of the glass, the conduction through it, and the volumetric heating. For the supply and outdoor air curtain mode, where the air enters at the same cold temperature as the outside air, at the bottom before the air in the cavity has traveled upwards and warmed up the glass will transfer some heating to the inside fluid. The colder the outside air temperature gets compared to the inside, the more energy will be conducted through the glass to the outside surroundings. With a cold enough surroundings, all the energy absorbed in the glass will be conducted to the outside, and the glass inside temperature will become below the temperature of the air on the inside of the cavity. Outside temperatures below this will remove useful energy from the hot air in the cavity. However, the energy absorbed in the glass is not completely lost as it does heat the glass to a higher temperature than the glass would be without the heating being there, thereby reducing the temperature differential between the glass and the inside cavity, reducing the losses out of the inside. So heating of the glass is better than the energy being reflected out of the system.

1.6 Thermal Efficiency Effects

To understand the energy efficiency of a solar thermosiphon, as with any thermal system, one must understand the energy transfer in the system. Efficiency can be defined as the useful energy out divided by the total energy in. For the solar thermosiphons the total energy in is the solar radiation that falls on the outside surface of the cavity. For the supply and indoor air curtain mode the useful energy is the energy that leaves the cavity in the heated air. This is defined as the following.

$$q_{usefull} = \dot{m} C_p (T_{exit} - T_{inlet})$$

The difference between the total energy in, and the useful energy is losses to the surroundings. As mentioned in the radiation heat transfer discussion due to the solar optical properties of the system the lowest amount of energy lost due to reflection with standard glass is about one quarter of the incident radiation. The rest of the solar radiation gets absorbed and converted into heat. The remaining losses come from this heat being conducted, convected or emitted to the surroundings. With good insulation losses to the inside of the building can be ignored. In the winter time losses through the wall to the inside of the building would be beneficial. In summer time losses to the inside of the building would be detrimental. The losses to the outside air would be determined by the infrared optical properties, the outside convection coefficient, and the temperature difference between the glass and the air. The outside convection coefficient and air temperature is beyond the control of the designer. The optical properties are set with the material selection. Only the glass temperature is something the designer might have control over outside of material selection. The glass temperature controlled by how well the system conducts heat through the glass. On the inside of the cavity, besides material selection, the only thing the designer has control over is the convection coefficient on the inside of the glass. The inside convection coefficient is related to the fluid flow on the inside of the cavity, which can be controlled by geometry, which is at the designers discretion. Given that the thermal efficiency of the system is so dependent on material properties, for heights of the cavity where the flow becomes turbulent, the configuration of the geometry is not likely to have a larger impact on the thermal efficiency.

What also can be taken from this analysis is that the optimal geometrical configuration for the highest mass flow rate is not likely to be the same optimal

geometrical configuration for the thermal efficiency. So for solar thermoshipon modes that are for heating, the supply and indoor air curtain modes, the optimal geometrical configuration will be different than modes for ventilation, the exhaust mode.

1.7 Dimensionless Analysis

To non-dimensionalize the setup and allow for scalability, dimensionless groups are applied to physical problems. For solar thermosiphons, the ratio of buoyant forces to momentum and thermal diffusivity is important and can be characterised by the Rayleigh number. The Rayleigh Number is found by multiplying the Grashof number and the Prandtl number. The Grashof number is the ratio of buoyancy forces to forces of viscosity. The Prandtl number is the ratio between momentum diffusivity and thermal diffusivity. There are two forms on the Grashof number, one for constant temperature walls, the other is called the modified Grashof number for constant heat flux applied to walls.

$$Ra_H = \mathrm{Pr}\, Gr_H$$

$$\mathrm{Pr} = \frac{\nu}{\alpha} = \frac{C_p \mu}{\kappa}$$

$$Gr_H = \frac{g\beta(T_W - T_\infty)H^3}{\nu^2},\ Gr_H = \frac{g\beta q H^4}{\nu^2 \kappa}$$

One of the primary uses of the Rayleigh number is it allows the prediction of when the flow will change from laminar to turbulent. However, the Rayleigh number is very specific to the geometry case considered, and the flow pattern and correlations used for a single flat plate for a given Rayleigh number, will not be the same as the flow pattern in a parallel plate cavity. Also a asymmetric heated parallel plate cavity will not give the same flow pattern as a symmetric heated parallel plate cavity with the same Rayleigh

number. So comparisons across different boundary conditions is not straight forward, and one cannot simply rely on the absolute value of the Rayleigh number alone to indicate the flow pattern.

Some other dimensionless values that could indicate system performance are the aspect ratios. The spacing between the parallel plates to total height, B/H, and the height of the inlet and outlet to the total height, E/H, are examples of influential aspect ratios. The Grashof number comparing the buoyant forces due to the difference in temperature of the air that enters the inlet and the air that the flow exits into, and the viscous forces would represent a parameter that has a large impact on the system.

$$Gr_A = \frac{g\beta(T_{@inlet} - T_{@exit})H^3}{\nu^2}$$

When there is a pressure difference applied by some external forces such as wind, the system will start to become a more typical forced convection case and the Reynolds number will start to become important.

$$Re = \frac{\rho \bar{V} B}{\mu}$$

Many past researchers focused on the Nusselt number, which is the ratio of convective heat transfer to conductive heat transfer. This was not discussed in the current work as it is not as it is not used as a performance metric for solar thermosiphons.

$$Nu_H = \frac{hH}{k}$$

1.8 Literature Review

A solar thermosiphon is a differentially heated open cavity. Therefore, research related to predicting performance of solar thermosiphons can be traced back to work of natural convection over a single heated vertical plate and flow between a differentially heated parallel plate open cavities. Different combinations of boundary conditions were applied, such as constant heat flux, constant temperature or perfectly insulated plates. The next progression was to consider the effect of the location of the inlets and outlets. Analytical, numerical and experimental work was carried out throughout this progression trying to improve the capability to predict the performance of solar thermosiphons.

1.9 Past Experimental Work

The first experimental work with configurations and boundary conditions similar to solar thermosiphons was work on differentially heated parallel plate cavities, with the focus of finding the convection heat transfer coefficient, h (Ayinde, Said and Habib 2006). To study the performance parameters more related to solar thermosiphons, mainly mass flow rate and thermal efficiency, the same differentially heated open cavities were studied, but with additional measuring capabilities (Chen et al. (2003), Burek and Habeb (2007), Ryan and Burek (2010)). Changing the location of the inlets and outlets to model practically implemented solar thermosiphons was the next progression (Trombe Wall by La Pica et al. (1993), Solar chimney by Bouchair (1994)). The previously mentioned work was all done at steady state, in laboratories using electric heaters. Work was also done on practically implemented solar thermosiphons

that were integrated into the side of a building, utilizing real weather conditions and true solar radiation (Onbasioglu and Egrican (2002), Hernandez et al. (2006)).

Although the practically implemented solar thermosiphons would seem to be the best way to find the performance of solar thermosiphons, the results found from these experiments were limited to thermosiphons of the same size, construction materials and connected to buildings of the similar ventilation properties. This is because the boundary conditions were transient, which are to expected for real weather conditions. Therefore it was not possible to separate the affect of changing material properties and geometrical configurations from the changing weather conditions. Given these limitations of practically implemented solar thermosiphons the focus of the current work is on steady state experiments, as these allow for accurately finding the effect on changing one parameter.

La Pica et al. (1993) investigated a Tombe Wall configuration. The one plate was 6 mm thick silvered glass to reduce infrared radiation heat transfer. The other plate was made of electric heaters that allowed varying the uniform heat flux from 48 to 317 W/m^2. The cavity had a single height of 2.6 m but the aspect ratio of B/H was varied between 0.029, 0.048 and 0.065. The data was collected once the system reached steady state. This included keeping a roughly constant room temperature that the air was drawn in from at the bottom and exited into at the top. This setup allowed development of empirical correlations for the convection coefficient, h, and the mass flow rate through the cavity. No correlations were presented for the thermal efficiency, however, enough data was presented to find the thermal efficiency. As expected the mass flow rate and heat transfer increase with increasing heat flux and B/H ratio.

Burek and Habeb (2007) considered a parallel plate cavity. The one parallel plate was transparent Perspex. The other parallel plate was made of electric heaters that allowed varying the uniform heat flux from 200 to 1000 W/m^2. The cavity had a single height of 1.0 m but the aspect ratio of B/H was varied between 0.02 to 0.11. The data was collected once the system reached steady state, which took roughly 3 to 5 hours. The room temperature varied no more than 2 ^{o}C during this time. This experiment allowed development of empirical correlations for the thermal efficiency and the mass flow rate through the cavity. The trends for mass flow rate and thermal efficiency were similar to those found by La Pica et al. (1993).

Ryan and Burek (2010) continued on the work of Burek and Habeb (2007) by adding heights of 0.5 m and 2.0 m along with the 1.0 m height. These new cavities were constructed of the same material as the 1.0 m height, and the experimental methodology was the same. This allowed getting empirical correlations for the thermal efficiency and the mass flow rate accounting for height, a parameter not experimental measured before. The mass flow rate was related to height by $H^{0.6}$. Since the exponent of height for the mass flow rate correlation is less than unity, two cavities of one meter height will provided more flow rate than a single cavity of two meter height, give all other conditions are the same.

During this work it was also noted that after increasing the B/H ratio beyond 0.2, the flow rate began to decrease from previously increasing. This was very similar to the results found by Bouchair (1994) who noticed a switch in the trend of the mass flow rate increasing with B/H ratio to decreasing when the B/H ratio was increased beyond 0.15. This would indicate there existed a optimal B/H ratio for mass flow rate.

What is interesting to note is that thermal infrared radiation from the absorbing surface to the glazed surface was recognized in the experiments, due to an increase in temperature on the glazed surface but was not quantified. The effect of different outside and inside temperature was not a varied parameter to find out its effect on the system performance.

So since past experimental setup ups were never constructed in supply mode, and simplifying assumptions were used, the predictive capabilities of the correlations found when applied to SAWs is not likely to be very accurate and could be improved.

1.10 Past Numerical Work

Originally laminar studies were the focus of numerical work on solar thermosiphons (recent work being da Silva and Gosselin (2005)). However, due to the height of most operational solar thermosiphons the flow becomes turbulent and numerical modeling work was done to account for this (Fedorov and Viskanta (1997), Badr et al. (2006), Zamora and Kaiser (2009) and Zamora and Kaiser (2010)).

Zamora and Kaiser investigated both a solar chimney (2009) and Tombe Wall (2010) configuration numerically. They included both laminar and turbulent flow regimes in their work. The Fluent finite volume commercial CFD software was used as the numerical code. The low-Re k-ω model was used as the turbulence model. The uniform wall temperature and uniform heat flux were applied symmetrically and asymmetrically as the parallel plate boundary conditions. All other walls were treated adiabatic, so there was no ability to account for the heat loss through what would be the glazing surface. No form of radiation heat transfer was considered.

Zamora and Kaiser did a parametric analysis to find the optimal mass flow and convection heat transfer coefficient by changing the Rayleigh number and the B/H ratio. The convection heat transfer coefficient and mass flow rate increased with increased B/H ratio. Zamora and Kaiser found numerically that there was an mass flow optimal B/H spacing that depended on Rayleigh number, and started at above 0.1 for laminar($Ra= 1 \times 10^5$) and dropped to below 0.1 for turbulent flows ($Ra= 1 \times 10^{12}$). One of the limitations of numerical work done by Zamora and Kaiser is they only give the result based on Rayleigh number and have no indication of the height of the cavity, which Ryan and Burek (2010) proved was important to consider on its own.

Zamora and Kaiser's work, along with all of the past steady state experimental work, was done with the same air temperature at the inlet and outlet. This is the boundary conditions for the indoor air curtain mode but not the supply or exhaust mode. The supply or exhaust mode will have the inlet temperature colder than the air temperature at the exit, making these system thermally stratified. As some previous researchers, such as Ryan and Burek (2010) and Gan (2006), pointed out in their recommendations for future work that the difference in temperature at inlet and exit should be considered.

As seen from the above discussion a considerable amount of research has been done on differentially heated parallel plate cavities. However, many simplifying assumptions were made, reducing the accuracy of the correlations developed from previous research when applied directly to real solar thermosiphons, particularly the SAW in supply mode. The next step is to include more real parameters, to get a more realistic model.

1.11 Objectives of Present Research

Based on the knowledge gaps identified in the prior literature review of solar thermosiphons, the following are the objectives of the current work:

1) Develop a numerical model to include real world parameters not considered before, such as conduction through the glazing surface and radiation heat transfer in a solar thermosiphon in the supply mode configuration.

2) Construct a experiment which will give results to validate the numerical model.

3) Develop correlations from the results to predict the mass flow in a solar thermosiphon based on changing the heat flux and B/H aspect ratio.

4) Draw conclusions from the results about the operation of the supply mode of a solar thermosiphon in practice.

Chapter 2

2. Experimental Investigation

2.1 Experimental Setup

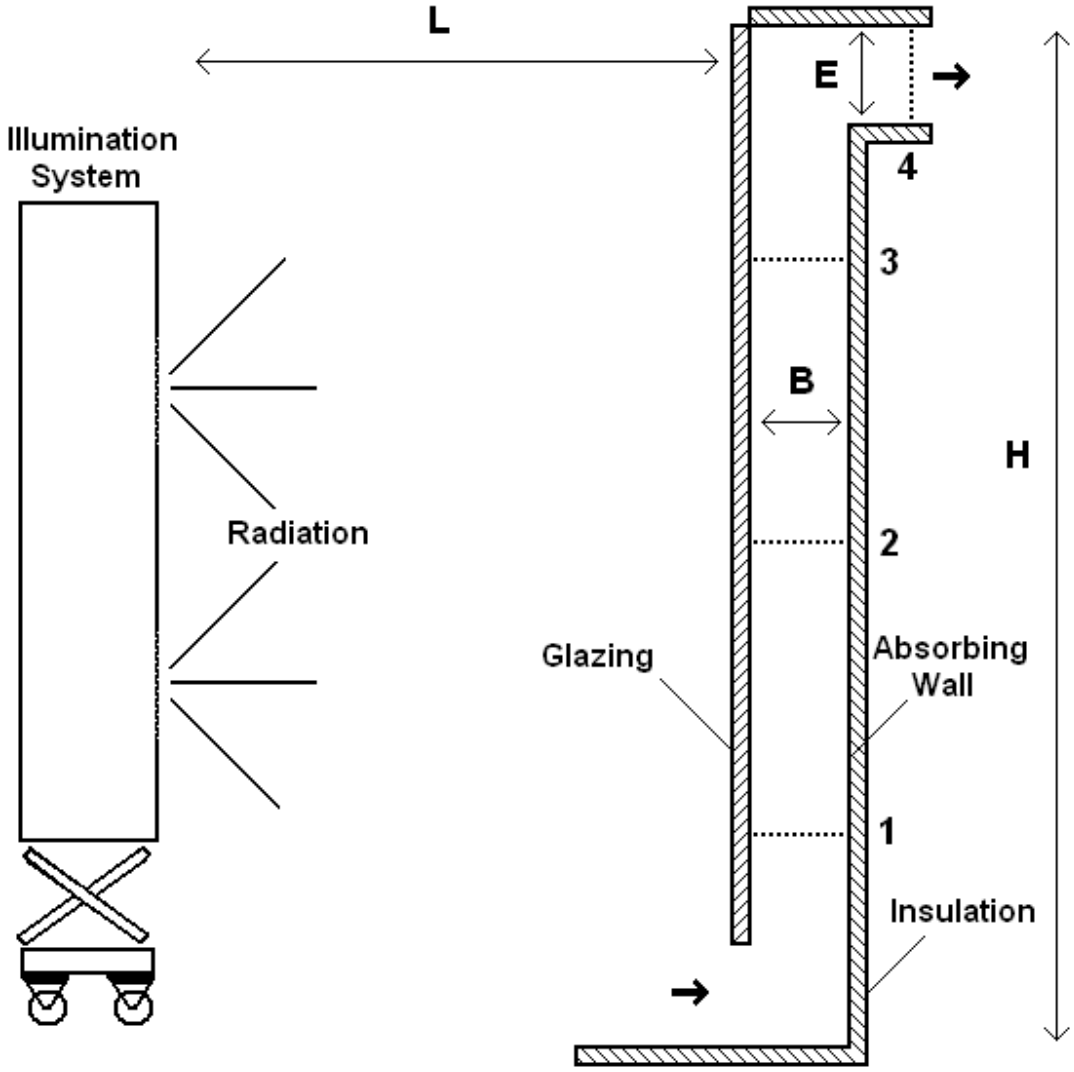

Figure 2.1: Experimental Setup

To accomplish the goal of validating the numerical model a novel experimental apparatus was constructed and can be seen in Figure 2.1. The configuration of the solar thermosiphon was in supply mode and radiation was used as the heat source, features not implemented before by previous researchers. The apparatus also allowed for variation of parameters that previous researchers found to have a affect on the performance of solar thermosiphons. These parameters that can be varied include the parallel plate spacing aspect ratio, B/H, the inlet and outlet height aspect ratio, E/H, and the radiation intensity. The optical properties of the system can changed by changing the type of glass and putting a different coating on the absorbing surface.

Due to the radiation intensity varying throughout the day in a real application, it is necessary to investigate this effect in the experiment. The heat flux in the current set up can be varied by varying the distance between the cavity and the radiation source. Two heat flux levels were selected for the current work to model the supply mode in winter in a Canadian climate. This was accomplished by consideration a south facing window in Ottawa, Canada, in January. The heat fluxes considered were the max heat flux during a day, and an average heat flux over the daylight hours, both on a perfectly clear day. These values correspond to roughly 600 W/m^2 and 380 W/m^2, and were calculated based on standard solar resource calculations as seen in Duffie and Beckman (1974).

2.2 Structural Frame

A custom structural frame was made to hold the various components in place to replicate a solar thermosiphon in supply mode. Softwood lumber was used to construct the frame. Sheet metal was used for the absorbing surface as it is what ventilation ducts

are construed from. Insulation was placed behind the sheet metal to reduce heat losses off the back. A one inch thick Expanded Polystyrene board, R-3.75, with a reflective radiant barrier facing the sheet metal was used.

The stationary cavity height of 1 meter was selected. This was because the location on a wall of a building that has the greatest potential for solar thermosiphons is spandrel areas. Spandrel areas typically range from 0.4-1.5 meters high depending on the architectural design, and 1 meter height falls in the middle of this height range.

A bottom ledge was added to allow adjusting the spacing between the absorbing wall and the glass. 40 cm was selected as the length of the bottom ledge from the absorbing wall, as one continuous piece would cover the entire bottom of the structural frame.

5.0 cm, 10.0 cm and 15.0 cm were the uniform nominal spacing between the absorbing wall and the glass, B. This gives three B/H aspect ratios of 0.044, 0.089, 0.133. They were selected cause they are uniform increases in the minimum aspect ratio, and also the max aspect ratio that can be obtained with the current measuring equipment.

2.3 Window Frame

To reduce the size and hence weight of the window frame compared to commercial window frames, a custom window frame had to be made. The overlap of the window frame on edge of the glass is 1/4", giving a 98.75 cm by 98.75 cm area of glass that solar radiation can pass through.

Due to the window frame, the inlet is shorter than the outlet by 5.0 cm. For the current work the inlet height was set at 7.5 cm and the outlet height at 12.5 cm, given an inlet and outlet ratio of 0.067 and 0.111, respectively. This was done to be a equal compromise of offsetting the extra height of the window frame.

Standard 6 mm thick float glass without an emissivity coating was the glazing used in the current work. The radiation properties of standard float glass is well known and can be looked up. The coating applied to the absorbing surface in the current work was flat black BBQ paint. This paint was selected as it was known to be stable at temperature much higher than those experienced in solar thermosiphons. A test sample of the absorbing surface was measured for its emissive properties in both the solar and near room temperature spectrums. It was found that the emissivity for a test sample was the same as typical black paint for both spectrums at 0.87 for the long wave, room temperature spectrum, and 0.94 for the short wave, solar spectrum. The testing method used a Gier-Dunkel MS251 Solar Reflectometer and a Gier-Dunkel DB100 Infra-Red Reflectometer following the American Society for Testing and Materials (ASTM) standard testing procedure.

2.4 Illumination System

The desired radiation source would have the same intensity for every wavelength as that comes from the sun and passes through the earth's atmosphere. This requires a black body source at the same temperature as the sun surface (5777 ^{o}K) that has the radiation pass through a 1.5 air mass filter, which is the standard filter to remove the intensities of the wavelengths that the earth's atmosphere absorbs or reflects. However,

getting a radiation source with exact spectrum as the sun proved difficult. A custom illumination system was purchased as it was the most economical way to simulate radiation from the sun. The illumination system could provide over a meter squared area an average of 1000 W/m^2. Quarts Tungsten Halogen(QTH) light bulbs were used which have black body spectral properties of 3000 ^{o}K to 3300 ^{o}K.

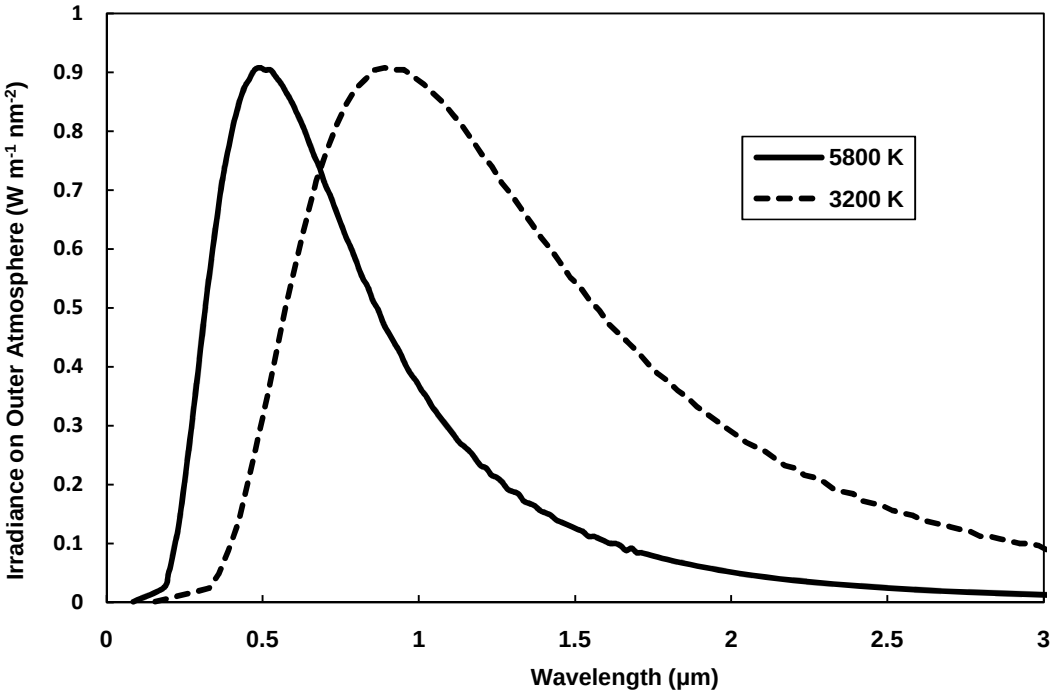

Figure 2.2: Spectral Distribution of Solar and Black Body Temperature of 3200 ^{o}K

As seen in the Figure 2.2 the QTH light bulbs have a black body spectrum that has less intensity in the visible spectrum than solar radiation. For the purpose of current experiment, radiation energy is converted into thermal energy, and if material properties are uniform across all wavelengths, as long as the same amount of total energy coming from the source was the same as would be from the sun, we would not be worried about the source radiation intensity with wavelength. However, real surfaces do have optical

properties that change with wavelength. For the experiment the two surfaces of importance are the absorbing surface and the glass. The absorbing surface had been painted with flat back paint, which has a consistently high absorptivity across all wavelengths and therefore is not sensitive to the source spectrum. The optical properties of glass are more sensitive to the radiation spectrum, particularly the fact that glass is opaque to long wavelength radiation, and has high transmittances to short wavelength radiation. The spectrum of a black body source at 3200 ^{o}K has most of its energy in wavelengths that glass still transmits at. So using the QTH light bulbs, although a different spectrum, will still give close to the same thermal results as a true solar source.

The four QTH light bulbs acted as point sources with light diverging from them. This resulted in the non-uniform heating pattern seen in Figure 2.3. There are hot spots directly in front of the light bulbs and the intensity decreases with radial distance from these hot spots. The intensity from the bulbs overlap in the center of the illuminated area. This cause a higher heat flux in the center of the cavity relative to the sides and the top and bottom. The non-uniform heating pattern results in a non-uniform flow, as the center receives more energy and reaches higher absorbing surface temperatures, inducing more flow in the center of the cavity relative to the sides.

It was only after the purchase of the current illumination system that it was found out that National Research Council of Canada has part ownership of the only large scale solar simulator in North America, capable of illuminating over a two meter squared area at 1000 W/m^2. Using this is a possible option for future work, to validate the findings of the current illumination system.

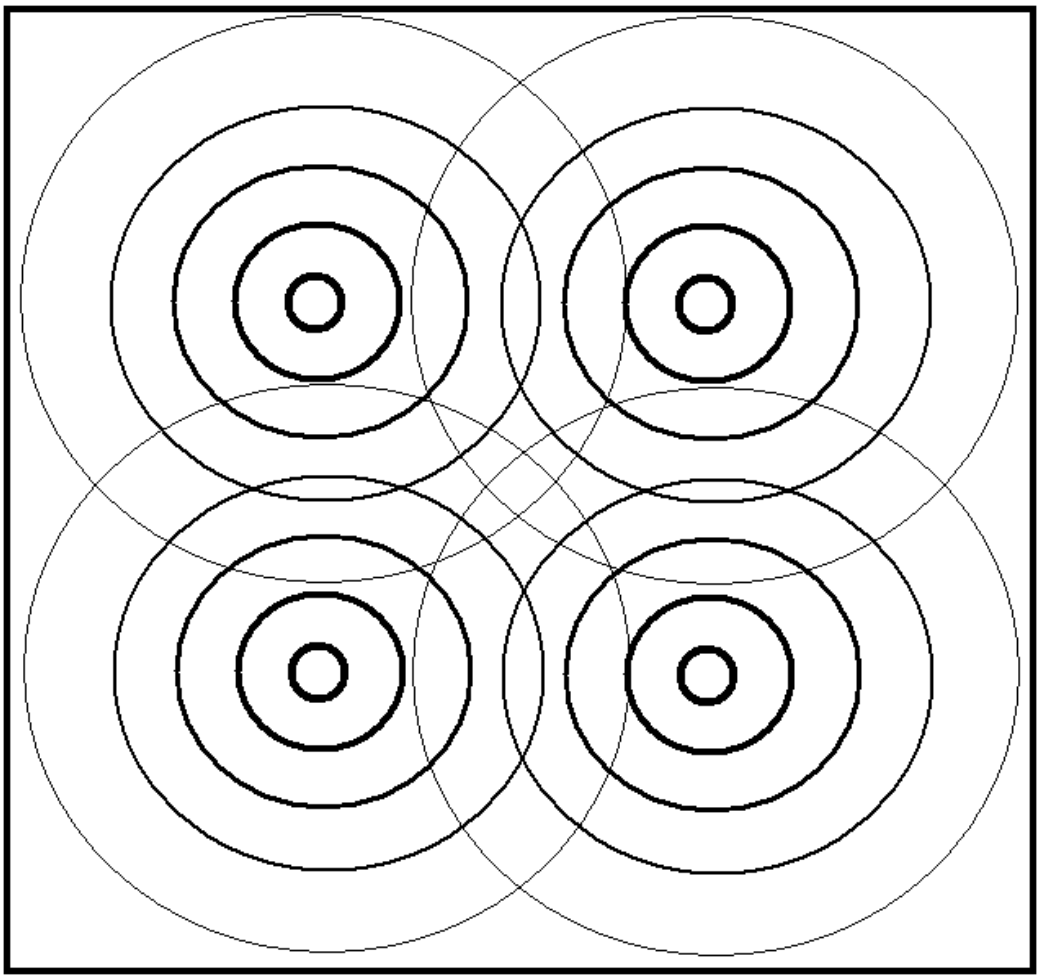

Figure 2.3: Over lapping heat flux intensities on the illuminated surface from the four bulbs used in illumination system

2.5 Pyranometer

Along with a radiation source comes the need to measure the intensity from the source. A solar pyranometer was selected as the measurement device primarily from its ease of use and applicability to the problem. A Hukseflux LP02, ISO second class, was the unit selected. It is not as accurate as the first class, but it provides the same

functionality. The units accurate operational range is 305-2800 nm, which contains the majority of the energy for the solar spectrum. A two dimensional square grid with 9 cm spacing between the pyranometer measurement locations was used to find the heat flux intensity over the illuminated square meter surface.

2.6 Data Acquisition System

Voltage readings from pyranometer, thermocouple and velocity probe measuring devices were gathered with a Hydra Data Logger Series II. Interchangeable input cards that had 20 channels were purchased to allow for easy switching between different measurement components rather than rewiring them every time. There was over 60 thermocouples, and it was not possible to read all at the same instant. Steady state experiments were done so that temperatures and velocities gathered at different times could be assumed to be constant over the test. Steady state was considered achieved when the temperature measurements on the absorbing wall did not increase by 0.5 ^{o}C in a 10 min period. After the air measurements were taken, the temperature of the absorbing wall was checked again and in most cases the temperature had gone up less than 1 ^{o}C from when steady state was assumed to be reached. The increases greater than this were associated with the ambient room temperature increasing from the start of steady state.

2.7 Temperature Measurements

The four locations in the center of the cavity that the air temperature was measured at can be seen in Figure 2.1, indicated by the dotted lines. Also in order to

validate the numerical model, temperature profiles on the center line of the vertical surfaces were collected. Thermocouples were selected as the measurement method due to their inexpensiveness and flexibility. Type T thermocouples were selected as they have the lowest uncertainty at the temperatures that were measured. The thermocouples were hand made by welding the 0.5 mm diameter wire together, resulting in diameters of 2 mm at the junction.

To measure the temperatures on the surfaces, thermocouples were attached with clear tape. Tiny strips of tin foil were placed in front of the thermocouples on the glass to shade them from the solar radiation. The room air temperature was measured with 5 thermocouples. A paper tube cover was put around these thermocouples so that the air currents could not blow directly on them, but the air could flow down the tube as the air temperature changed in the room. It was found that the room temperature could vary considerably, with a range of 18 ^{o}C to 26 ^{o}C noticed for different days. During a experiment the room temperature could vary 2 ^{o}C in a few hours.

The bottom ledge was heated up by the illumination system in front of the cavity inlet, and hence heated up the air in front of the inlet. So the air that was actually drawn into the cavity was warmer than the measured room temperature. A spot measurement was taken to confirm there was an increasing in the inlet temperature above the measured ambient temperature. However, the shading device use to shield the thermocouple from solar radiation disturbed the inlet flow pattern and this spot measurement does not represent the mass flow averaged inlet air temperature. Measurement of mass flow averaged inlet air temperature could not be taken as the experimental apparatus was not set up to measure the air temperature and the velocity at this location.

A single thermocouple was used to measure the air temperature in the cavity. To be confident in the results obtained, measurements were taken with time once steady state was reached, and the average of these used to state the temperature at that spatial location. By comparing the standard deviation, it was found that 50, one second interval readings, had the same standard deviation as higher number of readings, so this was the number of readings collected for all spatial points. For a given spatial location, the standard deviation never went greater than 0.2 ^{o}C, giving confidence that the average value was very consistent. As for the spatial resolution, this was adjusted from 1 mm to 5 mm depending on the temperature gradient in the area. In general it was found that the temperature did not vary greatly across the gap, even close to the absorbing wall. One of the reasons for not being able to capture high temperature gradients at the wall is likely due to the conduction down the thermocouple wire from the tip. One of the other issues that could lead to uncertainty with the temperature profiles is the sealing of the thermocouple probe, although care was taken to reduce this. The thermocouple use to measure the air temperature profile contacted the glass for the last reading.

Shading from direct radiation from the illumination system was provided for the velocity and air temperature profile measurements. Other forms of radiation were allowed to be incident on the thermocouple, including reflected solar radiation and emitted long wave radiation.

2.8 Velocity Measurements

The four locations that the velocity was measured at can be seen in Figure 2.1, indicated by the dotted lines The velocity measurements were taken with a

ComfortSense probe. The probe is omnidirectional, meaning it can measure the velocity at almost any direction the air flows towards it due to its spherical shape. Some of the benefits of the ComfortSense hotwire probe is that it has a temperature sensor built in and is factory calibrated to almost near zero velocities. Some of the limits of the ComfortSense probe are that it is 3 mm in diameter, making it hard to capture the high velocity gradients close to the wall, and it only has a frequency response of 2 Hz, making it unable to get turbulent properties. Also the built in temperature sensor is 3.5 cm behind the velocity probe, along the axial length. Therefore, the built in temperature sensor does not measure in the same vicinity as the velocity probe. The ComfortSense probe cannot get a full temperature profile when traversing from one side of the channel to the other as the velocity probe would have to go through the glass for the temperature probe to traverse the whole length of the cavity.

A Microsoft Office Excel spread sheet was provided from the suppler, that allowed conversion of the output voltage for both the velocity and temperature from the probe to the respective values, as well as a final correction to the velocity value for the effect of temperature, pressure and humidity. The details of the conversion can be seen in Appendix A. Also supplied with the probe was the calibration data required for the conversion.

Due to the turbulent nature of the flow, noticed by the variations in measured velocity, time averaging the measured velocity was done to represent the mean velocity at a spatial location. Following in the work of previous researchers (Ryan and Burek 2010) it was decided to use 100 samples per spatial location. The time per spatial location was less than 2 minutes with a second between every reading. It should be noted that the mean of a first hundred samples could be 5% different than the mean of

the second hundred samples, resulting in quite the variability in velocity. This is also seen in the standard deviation of the velocity reaching 35% of the mean value in the flow close to the absorbing wall. For the lowest horizontal profile, Location 1, in the region where smoke visualisation of the flow by previous researchers La Pica et al. (1993) indicated recirculation, the standard deviation is higher than the mean velocity found. One would have hoped that for this region the mean velocity would have went close to zero, and then gone back up again. This would have indicated a switch from upward to downward flow. With the current experimental results, which has no clear indication of a switch from upward to downward flow, which may be a sign that the recirculation zone is constantly changing in size. This would make it hard to compare the current experimental work at this location to steady state numerical results that predict a single size recirculation zone. As would be expected the downward velocities in the cavity are shown as positive absolute velocities when measured with the velocity probe. Hence the mass flow rate for the lowest horizontal profile, Location 1, turns out to be higher than all the other mass flow rates in found in the cavity.

Measurements at near zero velocities are very uncertain with hotwire probes. One of the phenomenon of hot wires is the natural convection flows they cause due to their overheat. So due to natural convection there is always some velocity going past the probe, even in what would be still air. The manufacture limit of ± 0.02 m/s uncertainty only applies down to 0.05 m/s. However, the calibration data that came with the velocity probe goes down to 0.0027 m/s. The problem comes in the regions close to the wall and in recirculation zones. In these regions many of the readings would be below 0.05 m/s, and the question becomes what value should be put in for this reading. If zero is put in for everything below 0.05 m/s, the mean will be lowered, increasing the standard

deviation of the readings artificially. So to reduce this lowering bias error, it was decided to use the calibration curve down to 0.0027 m/s, and only values under 0.0027 m/s would a zero reading be used. It is understood that the accuracy is not going to be good for measurements under 0.05 m/s, but this mentioned method will have less bias to it than putting in zero for all readings below 0.05 m/s.

Time averaging to find the mean value of the velocity was done by converting all 100 measured velocity voltages at a spatial location into a velocity, then average over all the velocities to get the mean velocity. The spatial resolution was varied depending on the velocity gradient. Near the absorbing wall the velocity goes from zero to reaching its maximum 2 to 3 cm off the wall. In this region the spacing was typically 1 to 2 mm, outside this region the spacing was increased to a maximum of 5 mm. The probe is 3 mm in diameter, so the spatial resolution is often less than the size of the probe, but the probe gives a measurement of averaged the heat lost over the diameter of the probe. So there will be additional uncertainty in the high velocity gradients, as one edge of the probe will experience one velocity and the opposite edge would experience a different. To not damage the velocity probe, it was not contacted with the glass surface.

2.9 Calibration

2.9.1. Pyranometer

The pyranometer came factory calibrated. There was a linear calibration of 14.8 μV per W/m^2, which is valid from 0 to 2000 W/m^2.

2.9.2. ComfortSense Probe

The ComfortSense probe came factory calibrated as well. The calibration curve is a nonlinear relation between the velocity and temperature.

2.9.3. Thermocouples

A Hoskin RTD was used to perform a two point check on the thermocouples. The RTD had a 0 to 200 ^{o}C range with 1/10 DIN accuracy, giving a max error of ±0.08 ^{o}C at 100 ^{o}C. Two calibration points were used and were achieved by a ice bath and a boiling bath. For the ice bath both the RTD and built in type T calibration curve on the Hydra Series II for all thermocouples gave a reading of 0.0 ^{o}C. For the boiling bath the RTD was reading 100.0^{o} C, most thermocouples with the built in calibration curve gave this as well, however a few gave higher reading with the max being 100.3^{o} C. Given that only two points were taken, a linear curve would fit perfectly. But the built in calibration curve is not linear, so it was expected the built in calibration curve would perform much better than a linear one, so the build in calibration curve in the Hydra Series II was used for all the thermocouple readings.

2.10 Uncertainty Analysis

The uncertainty for each measurement device was approximated using the manufactures data along with accounting for experiment dependant uncertainty. These independent uncertainties are then propagated through the respective equations to find the uncertainty of the dependant variable.

The equation for propagation of uncertainty is:

$$u(R) = \left[\left(u(\mathrm{W}_1)\frac{\partial \mathrm{R}}{\partial \mathrm{W}_1}\right)^2 + \left(u(\mathrm{W}_2)\frac{\partial \mathrm{R}}{\partial \mathrm{W}_2}\right)^2 + \cdots + \left(u(\mathrm{W}_\mathrm{n})\frac{\partial \mathrm{R}}{\partial \mathrm{W}_\mathrm{n}}\right)^2\right]^{1/2}$$

Where: u()=uncertainty in ( ), R= calculated result, and Wn=nth variable.

Using uncertainly values of ±0.02 m/s for velocity, ±1.0 ^{o}C for air temperature measurements, ±0.0001 m for spatial distances, and ±10% for the pyranometer readings the propagated uncertainty could be calculated. Looking at the example case of 600 W/m^2 on the outer surface and a 10 cm spacing behind the glass the following uncertainty was found and represents the propagated uncertainty for the other experiments as well. The uncertainty in of the total mass flow was ±7%. The calculated efficiency, described in the results section, was found to have a uncertainty of ±35%.

Chapter 3

3. Experimental Results

3.1 Experimental Results

The general experimental setup along with the location of where the air velocity and temperature measurements were taken in the cavity are shown in the Figure 3.1. Locations 1, 2 and 3 are located 20 cm, 50 cm and 80 cm from the bottom ledge, respectively. Location 4 is located 8.5 cm from the absorbing surface, and can be referred to as the exit profile.

The different experimental configurations considered in this study are summarized in Table 3.1. The first parameter changed was the space between the illumination system and the outside of the glass, L, resulting in a change in the heat flux incident on the outer surface. The second parameter changed was the spacing between the inside of the glass and the absorbing wall, B, changing the aspect ratio of B/H in the cavity. All other geometrical parameters remained constant in all experiments conducted. In Table 3.1., the average vertical center line heat flux incident on the absorbing surface can be seen to decrease with increasing B/H ratio. This is due to the fact that radiation diverged as the distance between the absorbing surface and the illumination system increased.

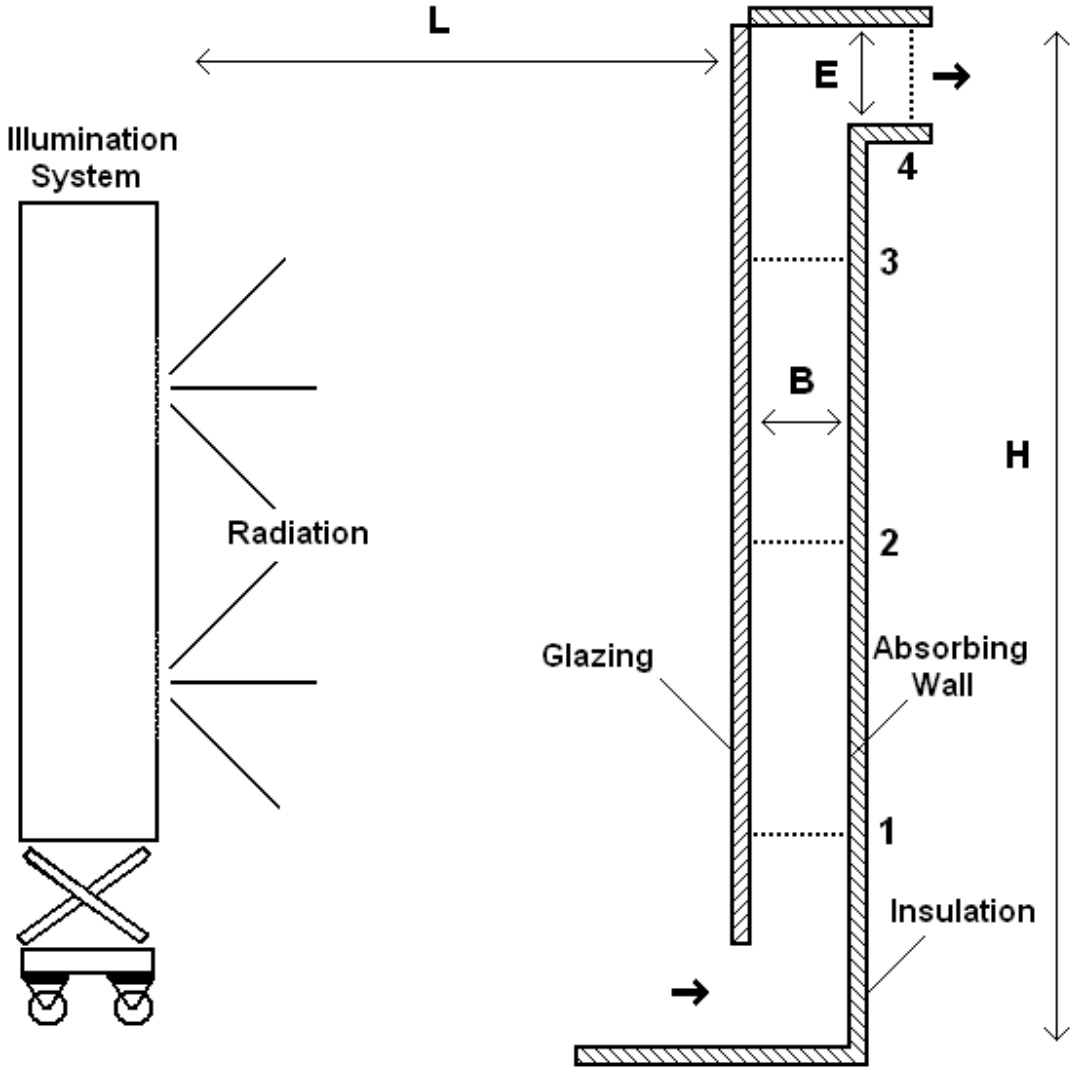

Figure 3.1: Experimental Setup

Due to the reflective sides and high absorptivity of the painted surfaces, it is assumed that once solar radiation enters the cavity, the majority of it will stay in the cavity. So, for a constant L spacing and increasing B, the total energy in should be roughly the same. However, the radiation energy will be spread over more area as the

top and bottom ledge surface area increases with increasing B. This results in the decreasing heat flux incident on the absorbing surface.

Table 3.1: Experiment Configuration

Experiment	B/H	L (m)	Avg Vertical Heat Flux Outside Glass (W/m^2)	Avg Vertical Heat Flux Absorbing Surface (W/m^2)
1	0.044	1	600	430
2	0.089	1	600	402
3	0.133	1	600	387
4	0.044	1.38	380	276
5	0.089	1.38	380	258
6	0.133	1.38	380	250

Pyranometer measurements on the two dimensional vertical surface were taken in front of the glass for the two L distances used to calculated the total energy incident on the system. The same measurements were taken behind the glass for all six experiments to calculate the total energy incident on the absorbing surface. Pyranometer measurements were also taken on a horizontal plane to find the energy incident upon the ground and bottom ledge in front of the and behind the inlet. The horizontal readings were a line taken in the center. Tables and plots of all these values a listed Appendix B.

As mentioned in the literature review the first loss of energy comes from the optical properties of the system. The ratio of the radiation measured behind the glass to what is incident on the front of the glass is the optical efficiency of the glass. Figure 3.2 shows the optical efficiency based on the average heat flux incident on the vertical center line of

the glass. The optical efficiency decreased with increasing the B/H aspect ratio. This is due to the increase in surface area of the cavity that the radiation is spread over.

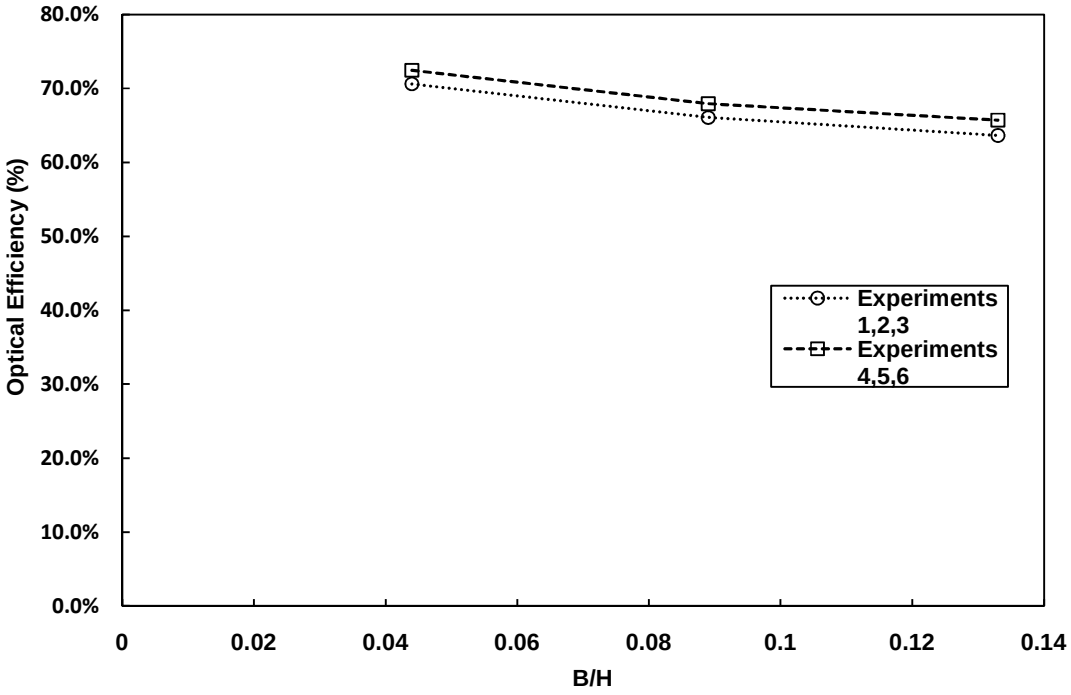

Figure 3.2: Optical efficiency vs. B/H aspect ratio for each experiment

The velocity and air temperature profiles for the four locations are shown for all six experiments in Figures 3.3 -3.14.

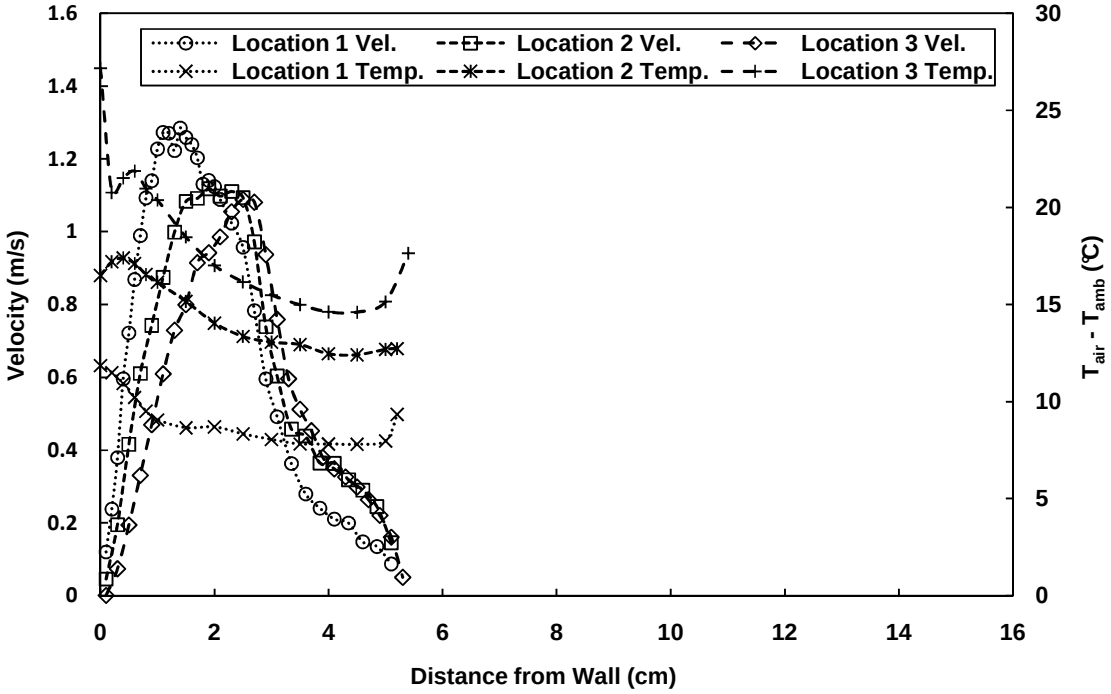

Figure 3.3: Horizontal velocity and temperature profiles for Experiment 1

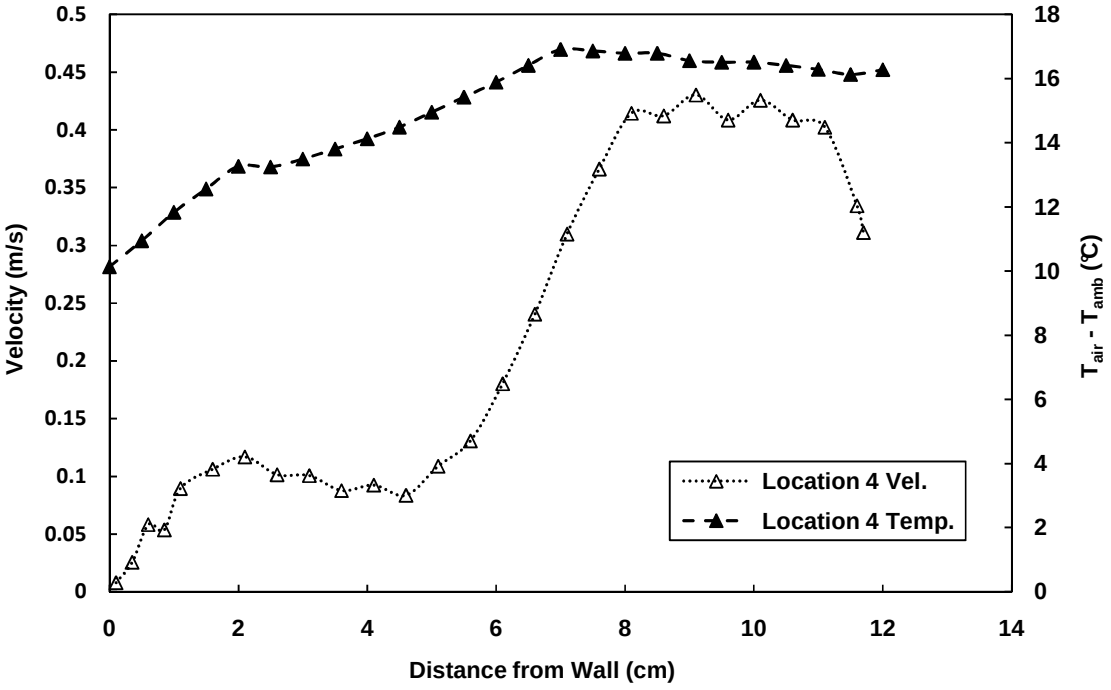

Figure 3.4: Vertical velocity and temperature profiles for Experiment 1

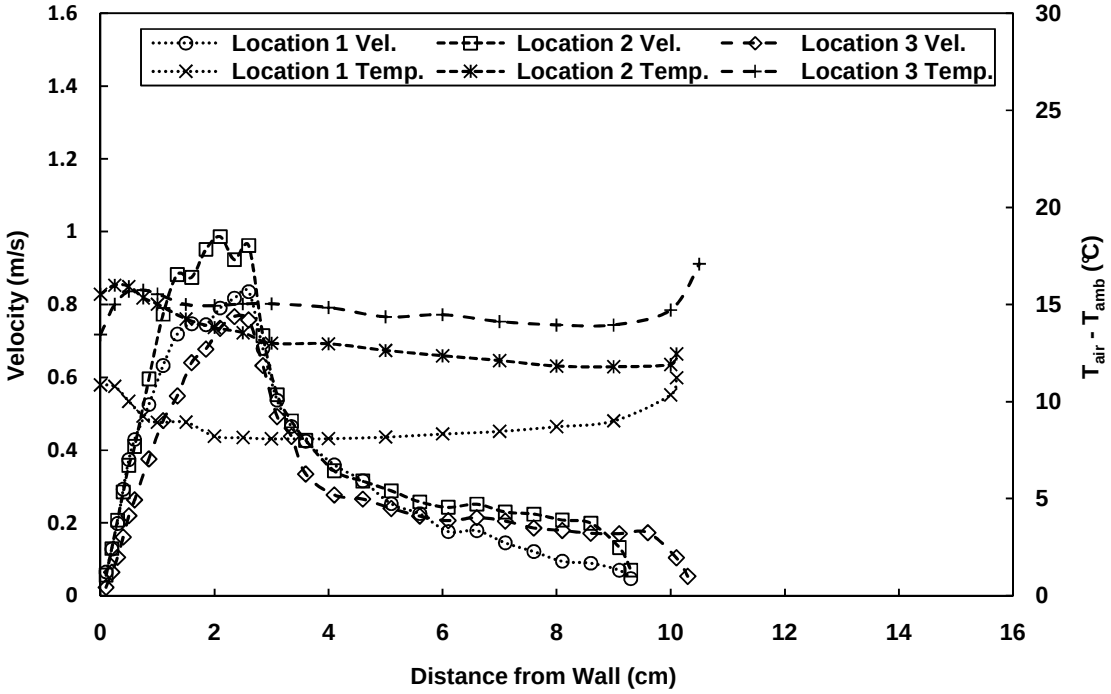

Figure 3.5: Horizontal velocity and temperature profiles for Experiment 2

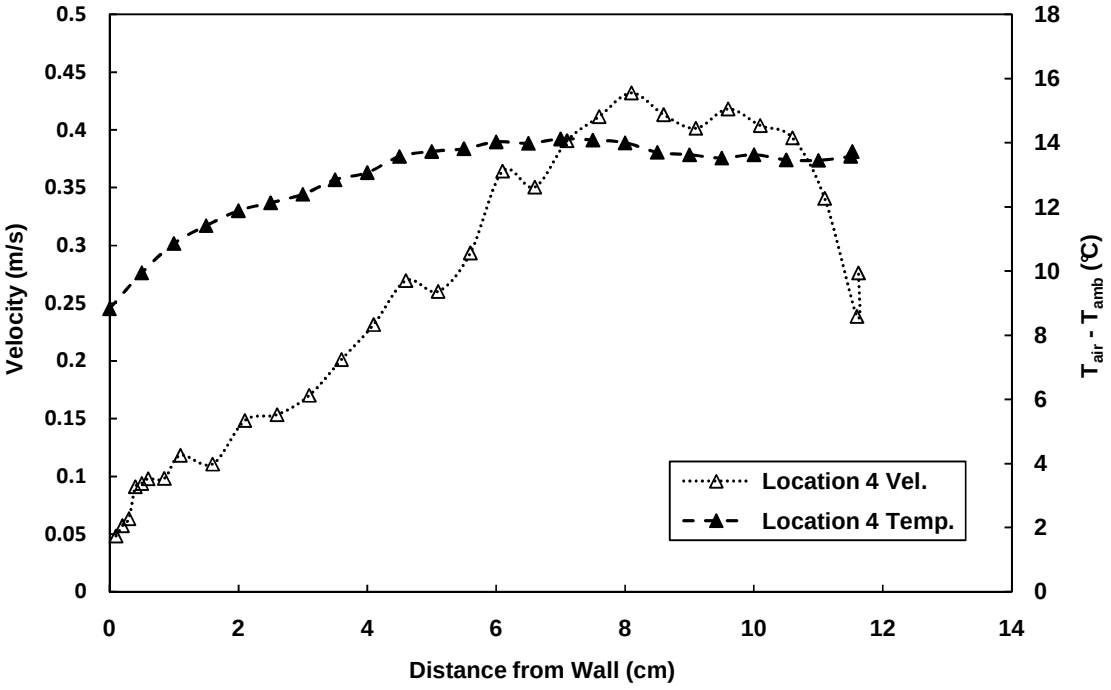

Figure 3.6: Vertical velocity and temperature profiles for Experiment 2

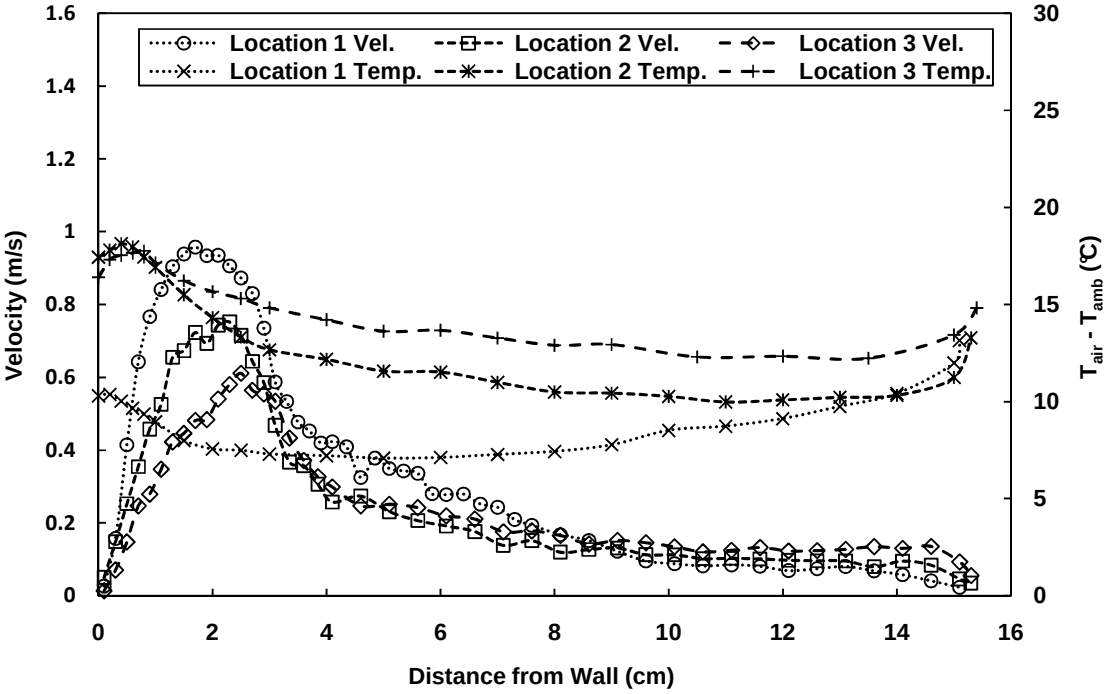

Figure 3.7: Horizontal velocity and temperature profiles for Experiment 3

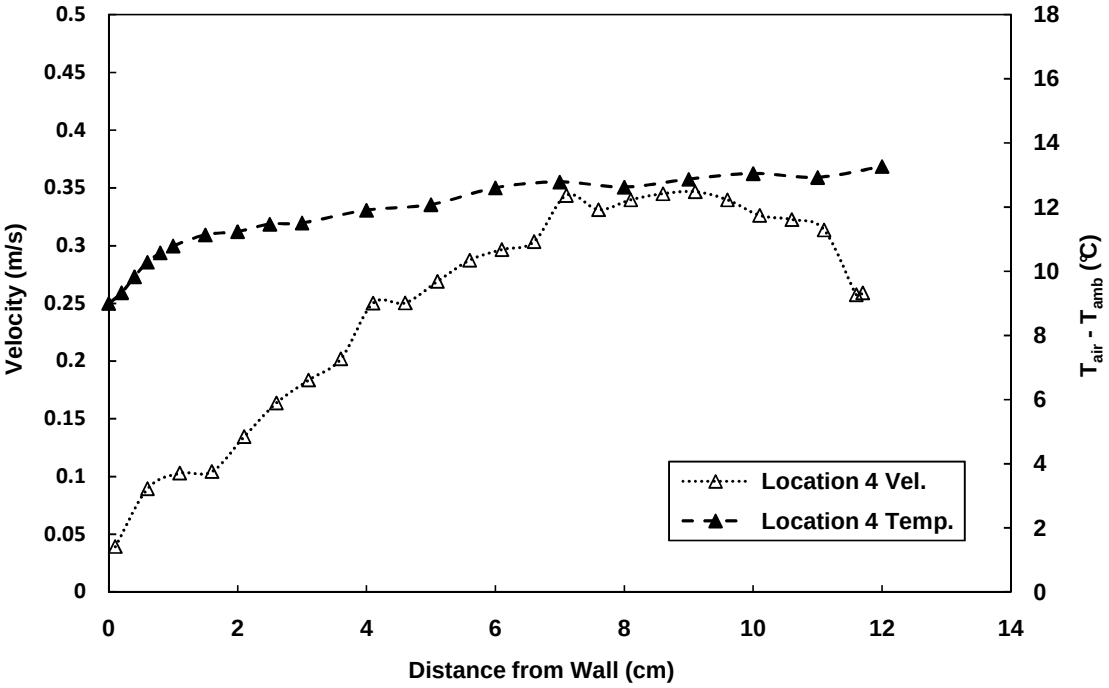

Figure 3.8: Vertical velocity and temperature profiles for Experiment 3

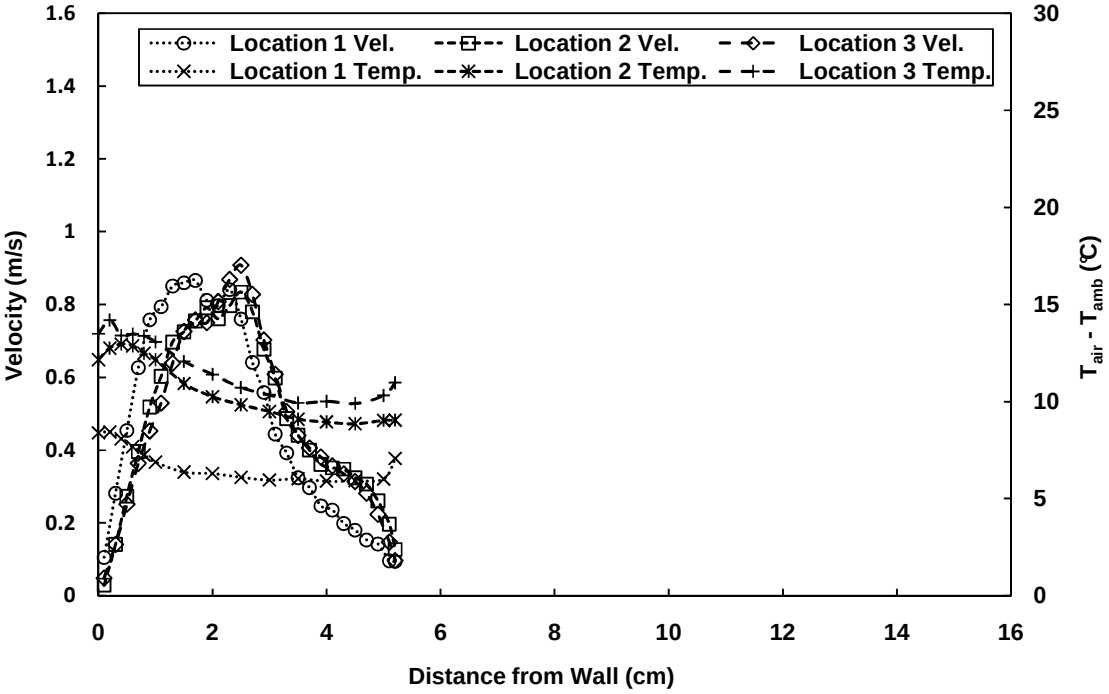

Figure 3.9: Horizontal velocity and temperature profiles for Experiment 4

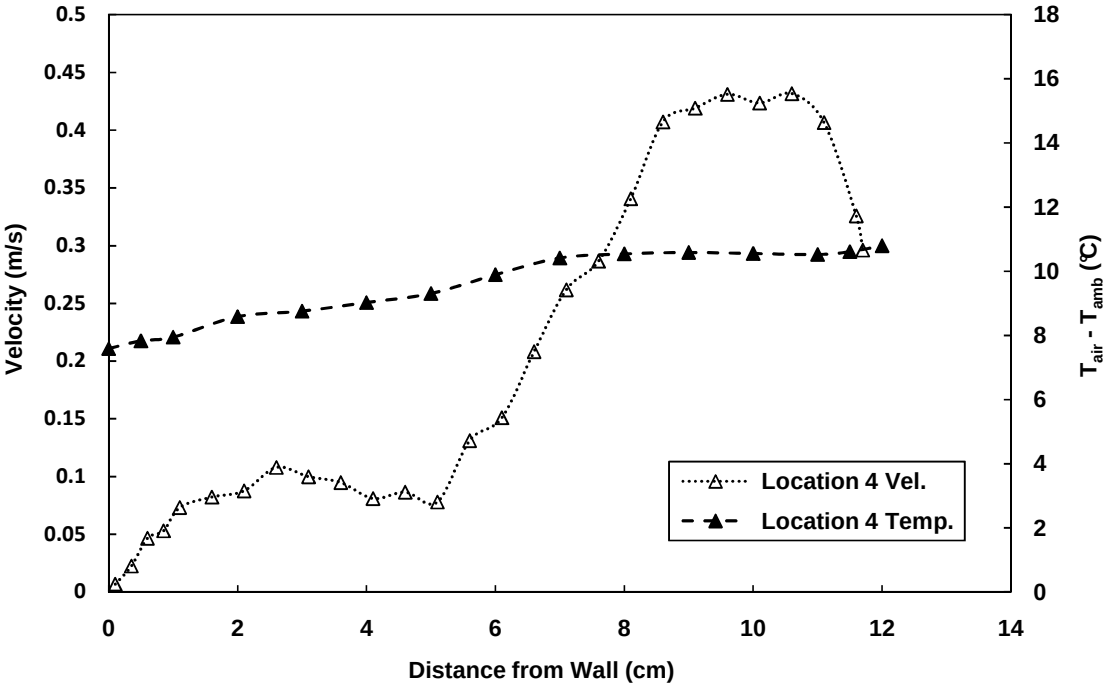

Figure 3.10: Vertical velocity and temperature profiles for Experiment 4

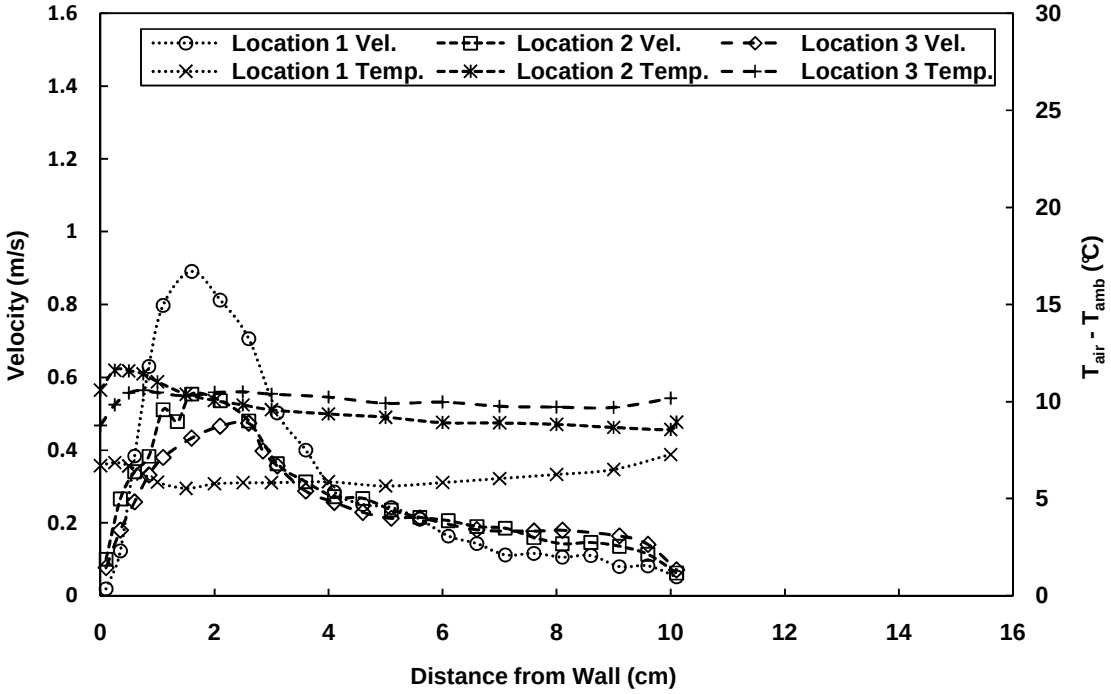

Figure 3.11: Horizontal velocity and temperature profiles for Experiment 5

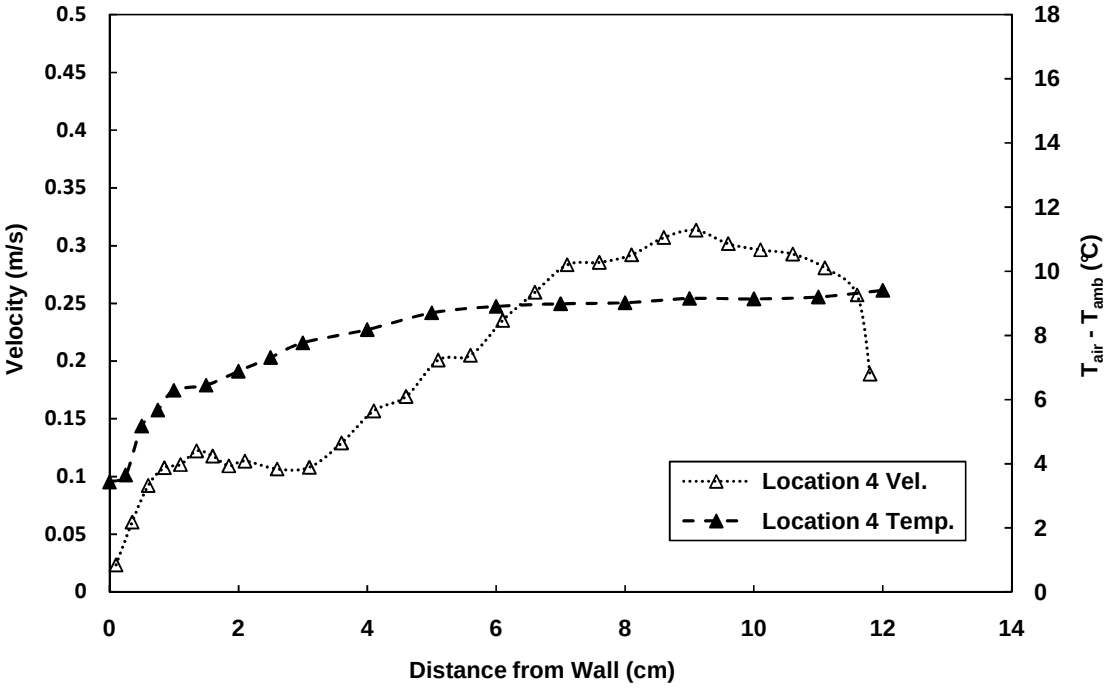

Figure 3.12: Vertical velocity and temperature profiles for Experiment 5

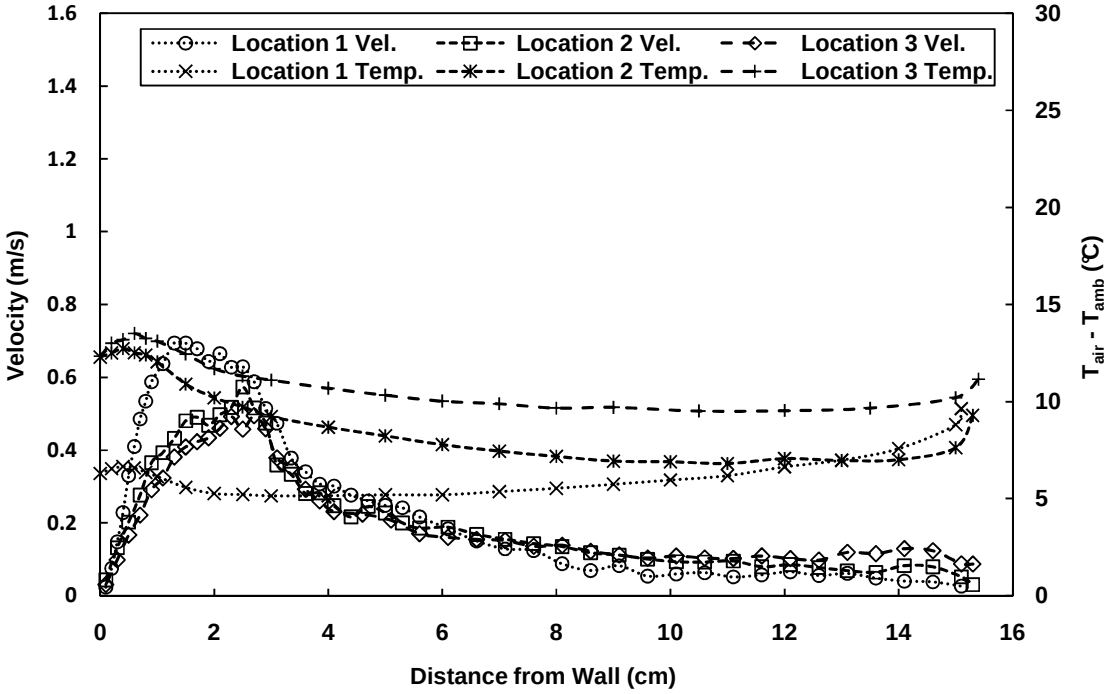

Figure 3.13: Horizontal velocity and temperature profiles for Experiment 6

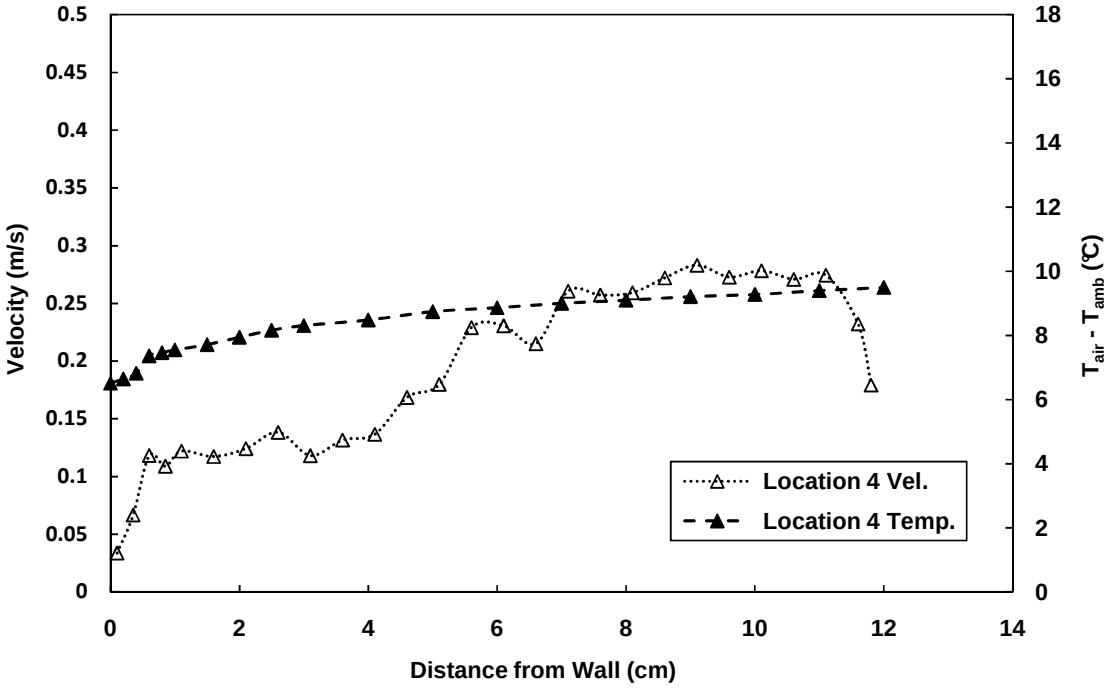

Figure 3.14: Vertical velocity and temperature profiles for Experiment 6

Figures 3.3 - 3.14 indicate velocity increases to a maximum a few centimetres away from absorbing wall and decreases after this going towards the glass surface. The peak velocity occurred at Location 1. This is likely due to the recirculation zone occurring at the inlet so that more flow needs to pass by the absorbing wall to balance the mass flow rate. The peaks at Locations 2 and 3 are further from the absorbing wall. The maximum velocity decreases as the B/H aspect ratio is increased, as there is more area for the flow to pass through.

As expected, the air temperature inside the cavity increase as the air passes upward through the cavity. The air temperature peaked close to the hot absorbing wall, decreased moving towards the glass wall, and increased right at the glass wall. This increase at the glass wall indicates that some of the solar radiation energy absorbed in the glass has transferred to the air inside the cavity.

The dimensional comparison makes it hard to directly compare results as the gap spacing changed. To make direct comparison easier, variation of the dimensionless velocity, $V/V_{average}$, as a function of the dimensionless spacing, X/B, are shown in Figure 3.15 at Location 3. This location was selected because it is the least influenced by recirculation, so the assumption of upward vertical velocity was most accurate at this location. The spacing was made dimensionless by dividing the spacing by the gap spacing, B, of the experiment. The velocity was made dimensionless by dividing the velocity by the mass flow averaged velocity calculated for each experiment.

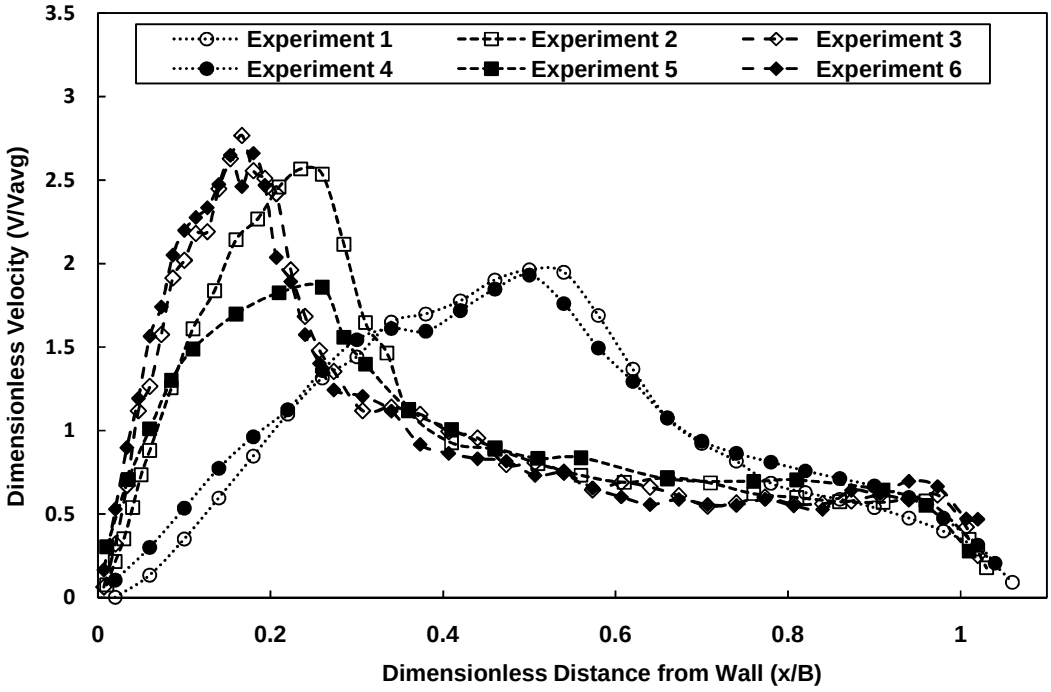

Figure 3.15: Dimensionless velocity, characterized by the mass flow average velocity of each experiment, vs. dimensionless distance from the absorbing wall, characterized by B, at Location 3

The mass flow rate for each experiment is compared at every location in Table 3.2. One of the reasons for the difference in the calculated mass flow rate is that the hot wire probe only measures the absolute value of the air velocity. So, if the flow is not perpendicular to the profile line, or if the flow is going in the opposite direction to the assumed direction, the integration of the velocity profile would be larger mass flow rate than what should be measured.

Table 3.2: Mass flow rate (Kg/s per m width)

Experiment	Location 1	Location 2	Location 3	Location 4
1	0.0384	0.0367	0.0329	0.0304
2	0.0378	0.0442	0.0361	0.0375
3	0.0519	0.0399	0.0390	0.0337
4	0.0297	0.0296	0.0293	0.0288
5	0.0372	0.0315	0.0289	0.0284
6	0.0374	0.0334	0.0330	0.0273

There is considerable variation in the calculated mass flow rate at each location for the experiments. More confidence could be put in the results if the mass flow rate calculated at each location for an experiment where the same like the results of Experiment 4. Numerical results predicted recirculation at Locations 1 and 4. With the absolute velocity measured in the experiment, it could be expected that the calculated mass flow rates at Locations 1 and 4 would be larger than locations without recirculation. However, Locations 1 and 4 do not always have higher mass flow rates than Locations 2 and 3, so recirculation alone cannot account for the differences. In fact Location 4 had the lowest mass flow rate in five out of the six experiments. The likely cause of Location 4 having a lower flow rate is the three dimensional effects caused by the illumination system. In Locations 1, 2 and 3 the energy intensity added was greatest in the center where the measurement was taken. The mass flow rate would be higher in the center as there is more energy to drive the flow in the center than at the sides. On the top horizontal ledge no energy is added and the flow would mix if there was turbulence. The high velocity fluid in the center would be go to the sizes and the slower velocity fluid at

the sides would go to the center. The net result is that the fluid velocity would become more uniform, reducing the velocity in the center and increasing it along the sides. So this three dimensional effect would cause the mass flow rate at Location 3, where a more energy is added, to be higher than Location 4 where mixing has caused the mass flow rate in the center to be lower. Except for Experiment 2, all the calculated mass flow rates are largest at Location 1 and decrease through Location 2 and 3 and is smallest at Location 4. This trend in the results could be due to the three dimensional effects of non-uniform heating from the illumination system.

To give an single value of the calculated mass flow rate for each experiment to represent the mass flow rate for the average centered vertical heat flux applied uniformly in a cavity, the average of the mass flow rates calculated for Locations 2 and 3 was used for calculating the mass flow rate for each experiment, except for Experiment 2. Only Locations 2 and 3 were used as they were very similar and did not appear to be effected by recirculation. The three dimensional effects would make the mass flow rates calculated at Locations 2 and 3 be lower than the case with uniform heating on the entire absorbing surface. For Experiment 2 only the mass flow rate calculated at Location 3 was used. This is due to mass flow rate calculated for Location 2 having such a higher value compared to any of the other locations for Experiment 2.

The variation of the mass flow rate as a function of the B/H aspect ratio is shown in Figure 3.16. Following the expected trend, the mass flow rate increased with increasing the aspect ratio. These results are in good agreement with previous experimental work by Bouchair (1994) where the maximum mass flow rate occurred at B/H aspect ratios greater than 0.15.

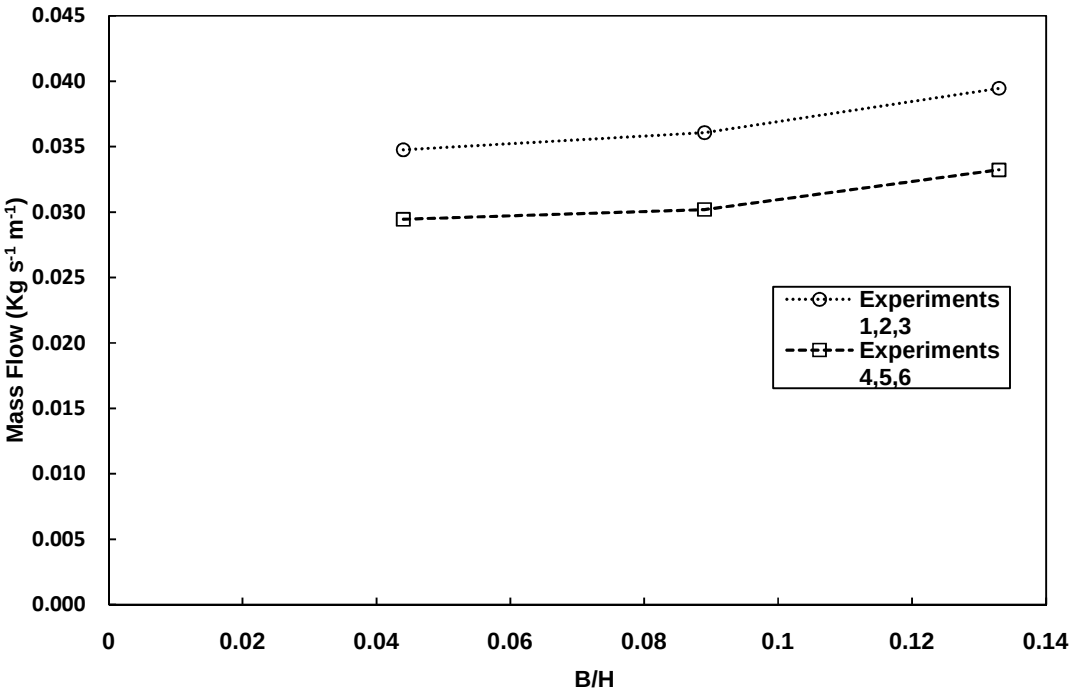

Figure 3.16: Mass flow rate per m width vs. B/H aspect ratio for each experiment

The variation in T_{exit}-T_{amb} as a function of the B/H aspect ratio is shown in Figure 3.17. The T_{exit}-T_{amb} decreases as the B/H aspect ratio goes up. This is because the mass flow does up as the B/H aspect ratio goes up and there is more mass to be heated by the nearly constant input energy.

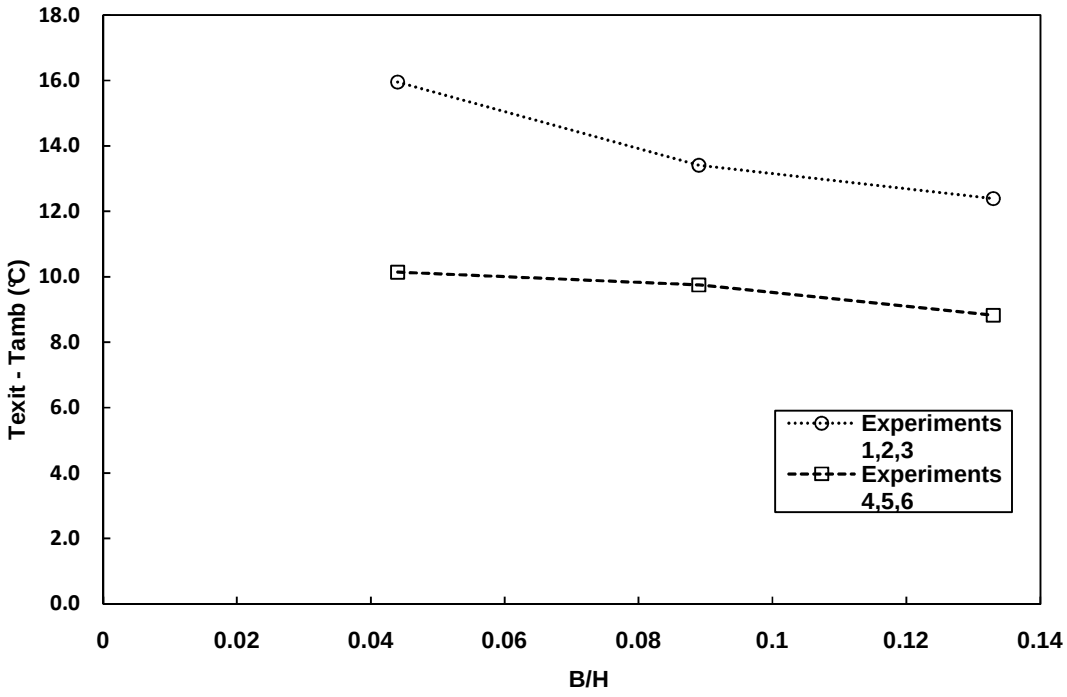

Figure 3.17: Increase of mass flow average exit air temperature above ambient vs. B/H for each experiment

The thermal efficiency as a function of the B/H aspect ratio is shown in Figure 3.18. This calculated efficiency is not the efficiency of the cavity alone. The ambient temperature was used in the calculation and not the inlet temperature, as the inlet temperature could not be measured. So the thermal efficiency calculated includes the energy added due to the heating of the bottom ledge. The thermal efficiency was constant for all the experiments except Experiment 1. Near constant thermal efficiency for varying B/H aspect ratio was also found in previous experimental work of Ryan and Burek (2010). The difference between the thermal efficiency of Experiment 1 and the other experiments is well within calculated uncertainly of the thermal efficiency which is ±35%.

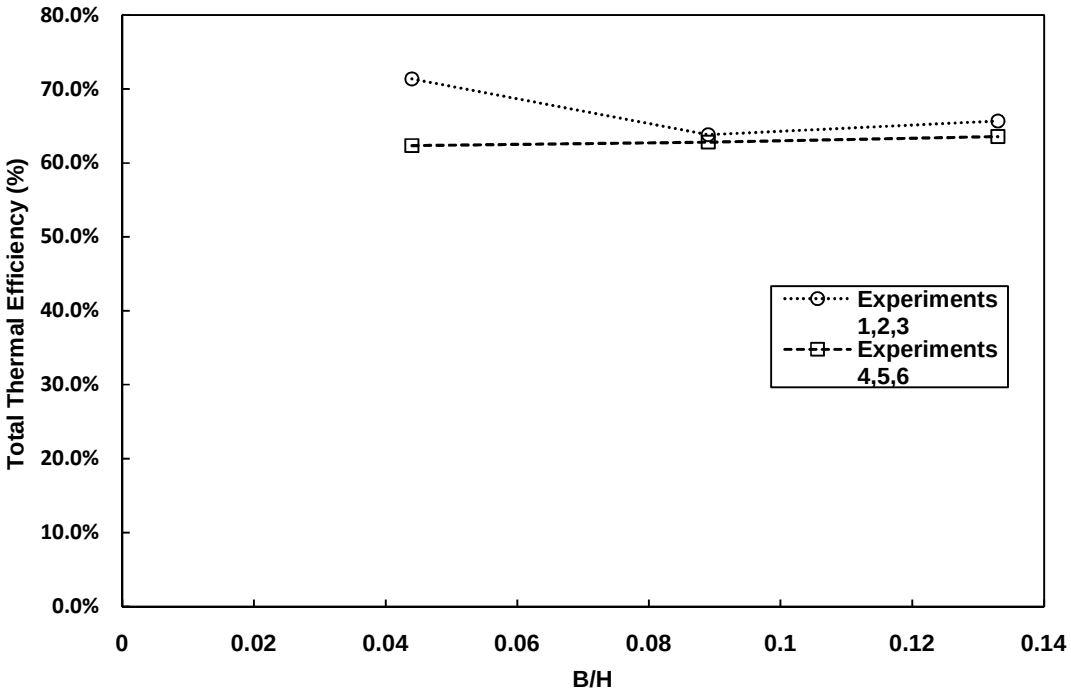

Figure 3.18: Total thermal efficiency including energy added to bottom ledge vs. B/H for each experiment

3.2 Comparison with Previous Experimental Work

The experimental results are compared to previous experimental work shown in Figure 3.19. This was done by using the correlations developed from previous experimental work. The heat flux incident on the absorbing wall in the current experiment was used in the correlations to be comparable with experiments that just used electric heaters behind the absorbing wall.

The work of La Pica et al. (1993) was used as it was an experimental setup of a indoor air curtain which has the most similar boundary conditions as the current experimental work. Ryan and Burek's (2010) work was used as it is the most

comprehensive study to date, allowing for adjustment of the height to be included. However, Ryan and Burek (2010) work was on the parallel plate channel and does not included flow bending around inlets and exits like the current setup.

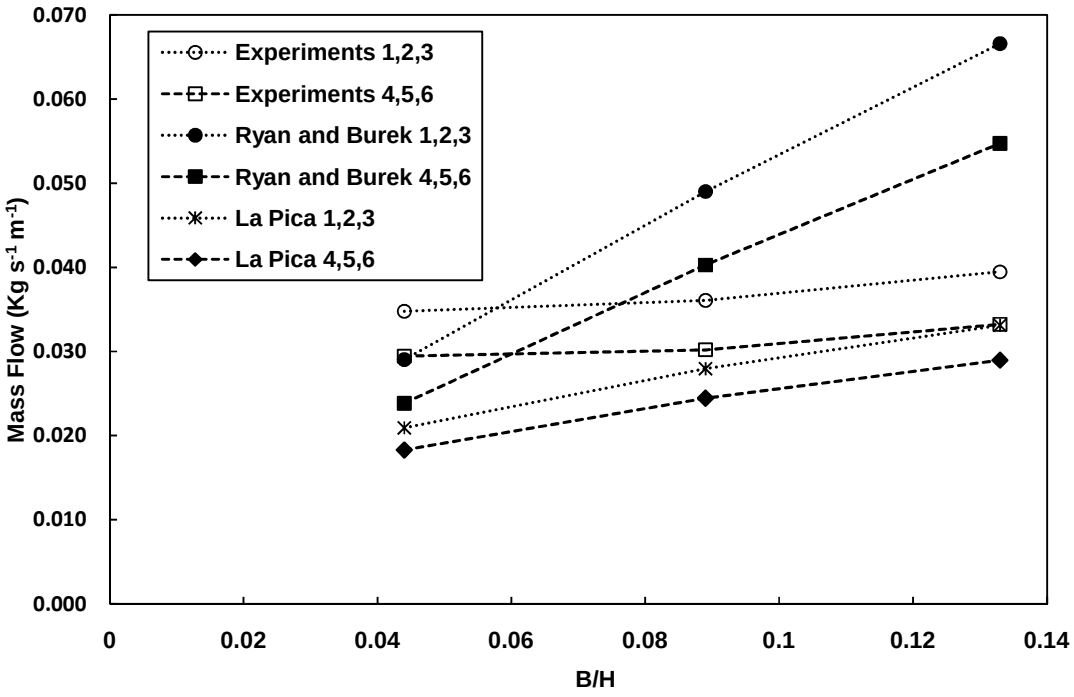

Figure 3.19: Comparison with previous experimental researchers of Ryan and Burek (2010) and La Pica et al. (1993)

The trend for increasing mass flow rate with increasing B/H aspect ratio and heat flux can be seen in all the results. What is different is the magnitude and the slopes of the lines. La Pica et al. has a lower flow rate at the low B/H aspect ratios compared to the current work. The preheating of the air on the bottom ledge in the current work, which results in higher flow rates compared to the cases without preheating, could account for the difference between the current work and the results of La Pica et al. La Pica et al. did not have any preheating in their experiment. Without preheating in the

current experiment the flow rate for the current work would decrease and be closer to La Pica et al. results, which would be expected as the configuration is very similar. Due to the three dimensional effects of non-uniform heating in the current work, it would be expected that the current experimental results would gave a lower mass flow rate than La Pica et al.'s results with uniform heating. However, inlet pressure drop effects would be different as La Pica et al.'s experiment had an inlet cavity, where as the current work only has a bottom ledge before the inlet.

Since Ryan and Burek's experimental setup was for a parallel plate cavity the mass flow rate should be higher as there was no turning of the flow to increase pressure drop like the current setup. The current work having a higher mass flow rate than Ryan and Burek at the 0.044 B/H aspect ratios could be due to the preheating in the current work which increases the flow rate. The steeper slope of Ryan and Burek's work is likely related to the parallel pate configuration that has no turns for the inlet and outlet and hence lower pressure drop. So after accounting for the differences in experimental setups, the current work compares well with that of Ryan and Burek.

The similarity between the current results and the indoor air curtain results of La Pica et al. (1993) validate the assumption used by previous researchers that electric heaters could be used to simulate the absorbing wall heat flux. However, the incident radiation on the outside of the glass cannot be use directly in their correlations. The incident radiation must first be multiplied by the optical efficiency of the glazing and absorbing wall system being used, the result of which is the heat flux absorbed on the back wall.

3.3 Correlation Developed from the Current Experimental work

The flow rate correlation based on current work of a solar thermosiphon in the supply mode is:

$$Re = 0.02609\ {Ra_H}^{0.402} \left(\frac{B}{H}\right)^{0.108}$$

The correlation coefficient R^2 is 0.95, showing very good fit with the experimental data. This correlation will only accurately predict the flow rate in setups with the same boundary conditions. This correlation would over predict the flow rate in real solar thermosiphons in supply mode, as the inlet temperature in the real case is lower than the air temperature at the outlet. Due to the preheating of the inlet air in the current experiment, the correlation developed from those results has limited applicability to even the indoor air curtain, which has the boundary conditions closest to the current experimental setup.

La Pica et al.'s (1993) flow rate correlation for a Trombe Wall:

$$Re = 0.5014\ {Ra_H}^{0.3148} \left(\frac{B}{H}\right)^{0.418}$$

Ryan and Burek's (2010) flow rate correlation for a differentially heated parallel plate cavity:

$$Re = 0.0348\ {Ra_H}^{0.459} \left(\frac{B}{H}\right)^{0.756} \left(\frac{H}{H_0}\right)^{-0.480}$$

Where H_0 is a reference height of 1.0 m.

The current work's correlation is similar to the pass correlations, as one would expect due to the similarity in boundary conditions. The biggest difference being the power of the B/H aspect ratio. The small sensitivity of this value in the current work could

be the result of the preheating of the incoming air on the bottom ledge, increasing the mass flow rate regardless of the B/H aspect ratio.

Chapter 4

4. Numerical Investigation

4.1 Development of the Numerical Model

The commercial CFD software program of ANSYS CFX was used to develop a two-dimensional numerical model. Simplifying the problem so that a numerical model can be developed is required. The following section outlines the assumptions made to develop the numerical model. A diagram of the computational domain can be seen in Figure 4.1 a).

4.2 Constant Density Assumption

The Boussinesq approximation was used to model the effect of buoyancy on the momentum equations. Constant properties of air at 25^{o}C was used in the fluid model. Using constant air properties and the Boussinesq approximation allows for keeping density constant which was found to cause convergence issues when left as a variable. Given the small change in temperature of the bulk fluid in the experiment, the density variation is small and therefore can be neglected.

4.3 Glass and Fluid Domains

Previous numerical researchers have used a single surface to model the glass. However, as mentioned in the literature review, this does not allow for accurately accounting for the effect of the glass on the heat transfer in the cavity. For the current

work, a glass domain is interfaced with the fluid domain. An interface between the two domains is required to conserve the energy exchange between them.

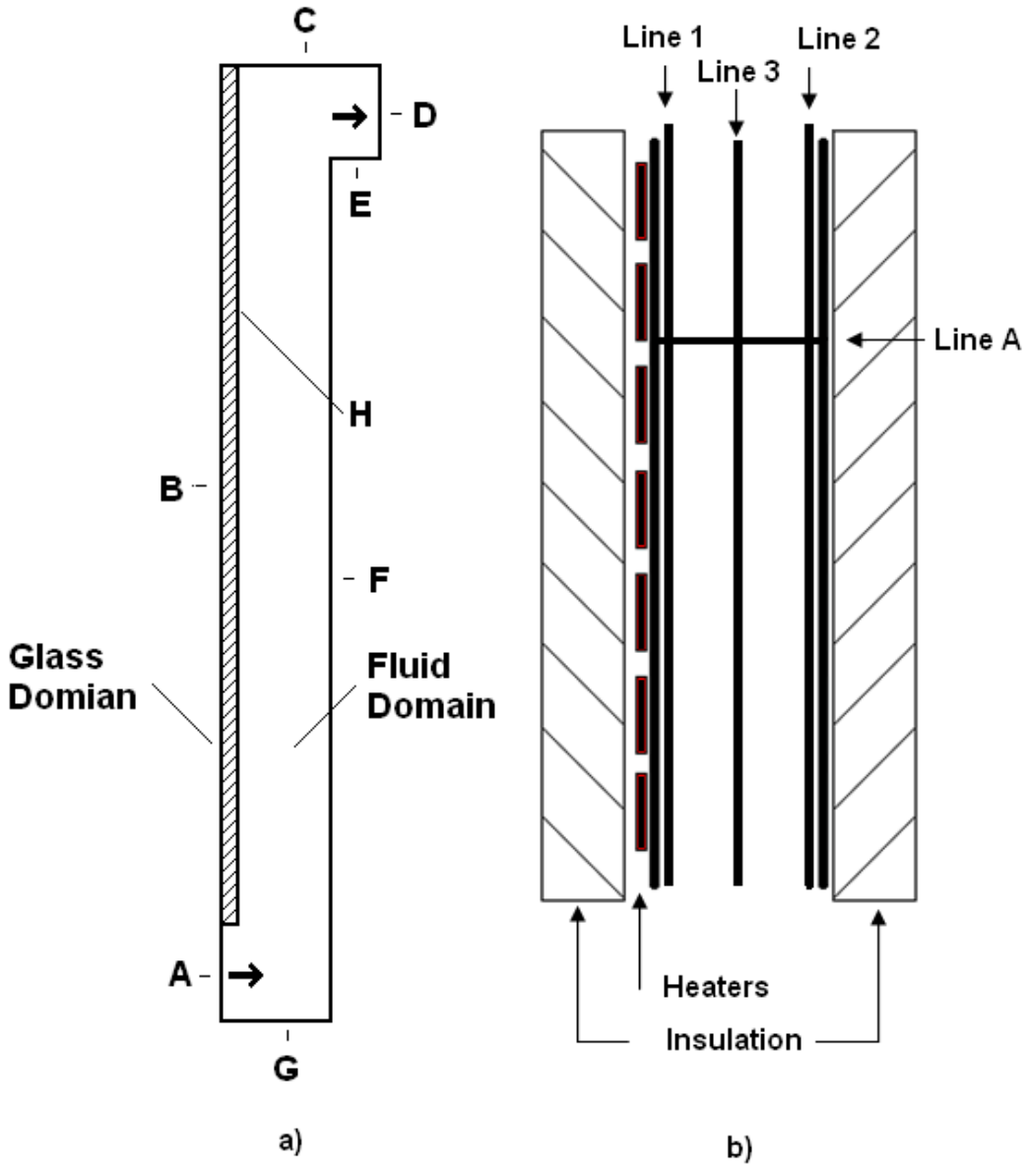

Figure 4.1: a) Numerical computational domain with alphabetic labelling of boundaries b) Experimental setup of Chen et al. (2003)

4.4 The Turbulence Model

The Shear Stress Transport (SST) model developed by Menter (1994) was used. The SST model is known to be a robust model for predicting flow separation and reattachment compared to the standard k-ε model. As with all two equation models the SST model assumes flows are isotropic. Buoyancy is an anisotropic effect on turbulence. The SST model still proved to be a accurate prediction of the flow, as seen by the validation discussed at the end of this chapter.

4.5 The Infrared Radiation Model

One of the large improvements of this work from previous numerical work is the inclusion of thermal infrared radiation modeling. The solar spectrum radiation was not included in the model. Due to the small heat transfer from natural convection, infrared radiation can be a considerable portion of the heat transfer between the warm absorbing wall and the glass surface. This is very important to model as this will greatly affect the losses through the glass surface to the outside.

The discreet transfer method was used to model the surface to surface radiation heat transfer inside the fluid domain. The air was considered a not participating medium. With the discreet transfer method, view factors between nodes are calculated at the start of the simulation. This is done by discreet rays. The higher the number of rays used, the more accurate the results are. However, the higher the number of rays used the longer the computational time. The number of rays was set to 8 for all simulations. This was suggested by ANSYS as a first approximation. It proved to be accurate as seen by the validation of the numerical model. A uniform gray body spectral model was use. This is

because the measured emissivity's, which were described in the experimental setup chapter, are a weighted average of the infrared spectrum. Again one should note that the measured short wave length optical properties can be quite different than the long wave length properties. This is particularly important for glass, as glass is transparent in the solar spectrum but is opaque and highly emissive in the infrared spectrum.

4.6 Validation of the Numerical Model using Data from Past Research

To check the validity of the numerical model, the numerical results were compared to experimetnal results reported in Chen et al. (2003). A diagram of the parallel plate experimental setup of Chen et al. (2003) can be seen in Figure 4.1 b). The cavity had a height of 1.5 m and the cavity B/H aspect ratio could be adjusted from 0.07 to 0.4. A representative case of a 400 W/m^2 heat flux applied on the heated side with a B/H aspect ratio of 0.26 was used for validation. A comparison between the numerically calculated temperature and the experimental data along the height of the cavity for the three lines vertical lines shown in Figure 4.1 b) can be seen in Figure 4.2. Good agreement can be seen for the temperature profiles. A comparison between the numerically calculated velocity and the experimental data along horizontal line A shown in Figure 4.1 b) can be seen in Figure 4.3. Again the numerical predicted the experimental data accurately. Chen et al. (2003) did not provided mass flow or thermal efficiency in their results.

So although the numerical model performed well in predicting the results of the experimental case of a parallel plate cavity, there was considerable concern over the

models accuracy when trying to predict a more realistic case of the supply mode. This lead to the development of the current supply mode experiment.

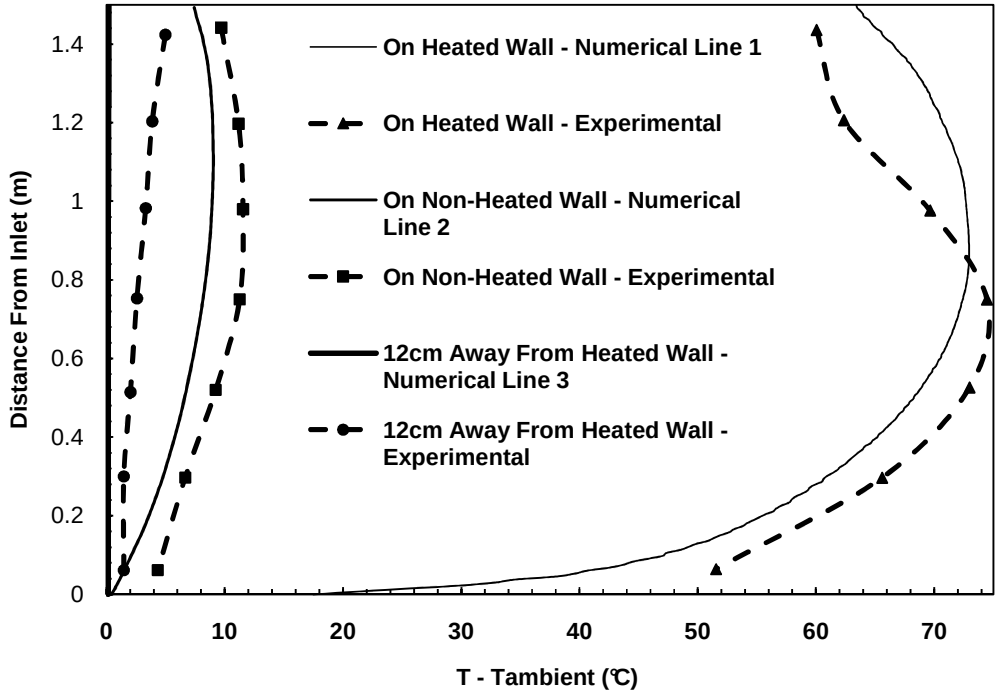

Figure 4.2: Vertical temperature difference along channel height at three different locations comparing experimental work of Chen et al. (2003) and current numerical model

4.7 Model Verification

Using the current experiment's data with a vertical centerline average of 600 W/m^2 on the outside of the glass and a B/H ratio of 0.089, independence tests were done. The convergence criterion was increase from a minimum root mean squared (RMS) change in velocity from one iteration to the next of 1 x 10^{-4} to 1 x 10^{-5} and there was a difference of less that 1% in the mass flow rate. This gives confidence that a RMS of 1 x 10^{-4} will give results independent of the convergence. A finer mesh with 576,000 nodes with the

same Y+ value of the first node of 1.5, was compared against the original 180,000 nodes case. The difference in mass flow was less than 2%, allowing use of the original mesh with confidence that finer meshes will not change the results. It should be noted that a unstructured mesh was used with 5 inflated layers off all wall surfaces and can be seen in Appendix C.

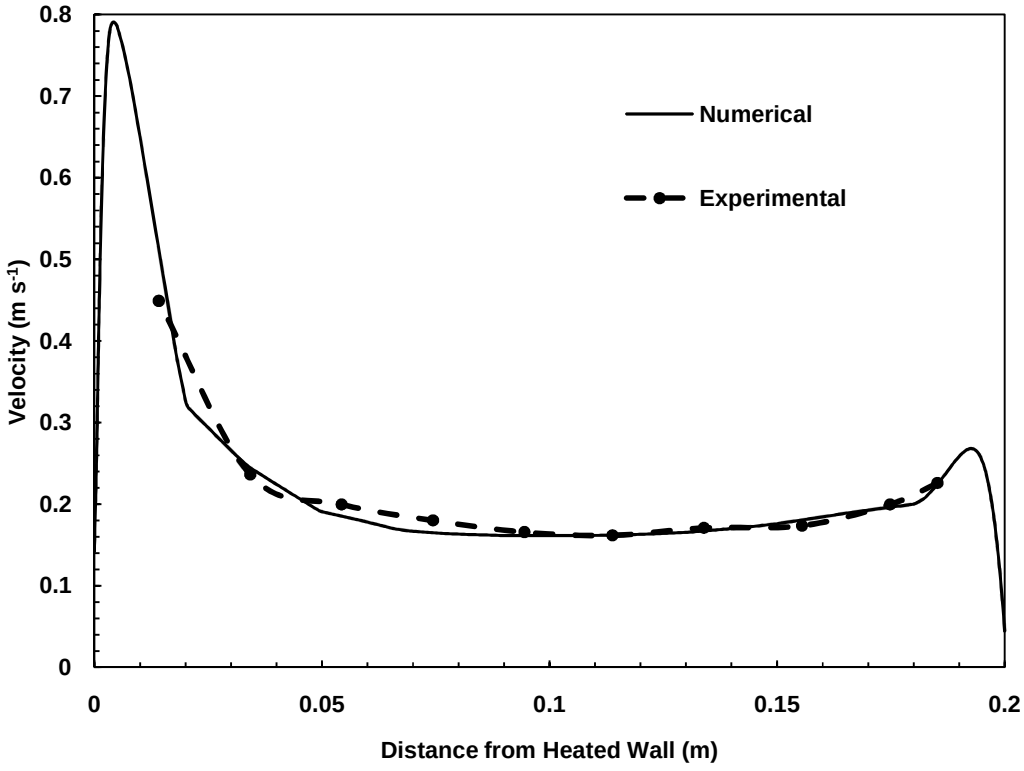

Figure 4.3: Velocity across gap, 1100 mm above the inlet comparing experimental work of Chen et al. (2003) and current numerical model

4.8 Boundary Conditions in the Numerical Model

The following boundary conditions were applied in the numerical model to simulate the conditions imposed on the current experimental setup. Both the inlet and outlet, boundaries A and D in Figure 4.1 a), were set as openings with the same uniform reference pressure of one atmosphere to allow recirculation. Initially a constant air temperature of 25 ^{o}C was applied at the inlet and exit, boundaries A and D in Figure 4.1 a). The inlet temperature was then increased relative to the temperature at the exit. The reasoning for this will be explained in the following section.

All the walls of the fluid domain, boundaries C, E, F and G in Figure 4.1 a), were assumed to be perfectly insulated, so that there was no losses off the back of them. This assumption is not correct, but a value for the heat flux loss is not known. This needs to be investigated in the future, so that accurate values can be used.

To model the incident solar radiation on the absorbing wall, boundary F in Figure 4.1 a), a parabolic equation that best fits the vertical centerline pyranometer readings for behind the glass was used. The pyranometer readings can be found in Appendix B. To impose heating in the glass domain to account for the absorption of solar radiation of the glass, 10% multiplied by the average measured heat flux on the vertical centerline on the outside of the glass was used. A heat flux was applied to the bottom ledge, boundary G in Figure 4.1 a), and was the average pyranometer measurements taken along the bottom edge. The thermal conductivity of the glass was set as 0.81 W/(m ^{o}C) .

The outside glass surface, boundary B in Figure 4.1 a), was bounded by a heat transfer coefficient of 5 W/(m^{2} ^{o}C) and was selected as this is the natural convection heat transfer coefficient used for flat plate solar collectors in no wind conditions as seen in Duffie and Beckman (1974). The outside air temperature applied along with the outside

heat transfer coefficient was the selected inlet temperature. This selection of values for outside heat transfer and outside air temperature is very subjective and needs further measurements, which were beyond the capabilities of the current experiment, in the future to validate these assumptions.

The emissivity of the walls, boundaries C, E, F and G in Figure 4.1 a), was 0.87, the value found for black paint in the long wave length spectrum. The emissivity of glass, boundary H in Figure 4.1 a), used was 0.85, again found experimentally. The inlet and outlet, boundaries A and D in Figure 4.1 a), infrared radiation effects were set to be determined by the local fluid temperature.

4.9 Model Validation using Current Experimental Data

4.9.1. Comparison between numerical and experimental results

Numerical results were compared with experimental data from the six experimental configurations. A comparison between the numerically predicted and the experimentally found mass flow rate for the inlet and outlet being the same temperature can be seen in Table 4.1. The mass flow was consistently lower for the numerical case than the experimental data. A large part of this difference could be due to the inlet air in the experiment being warmer than the measured ambient air temperature as discussed in the previous chapter. However, the three dimensional effects of non-uniform heating from the illumination system and other uncertainties could also attribute to the difference. The numerical horizontal and vertical velocity profiles for the case where the inlet temperature equals the ambient for all six experiments can be seen in Appendix D.

Velocity vectors on top of a temperature contour can also be seen for all six experiments in Appendix D.

Table 4.1: Experimental and numerical mass flow comparison for $T_{inlet} = T_{amb}$

Experiment	Mass Flow Experimental (Kg s^{-1} m^{-1})	Mass Flow Numerical (Kg s^{-1} m^{-1})	Difference (%)
1	0.0348	0.0196	44
2	0.0361	0.0184	49
3	0.0395	0.0186	53
4	0.0295	0.0171	42
5	0.0302	0.0160	47
6	0.0332	0.0165	50

4.9.2. Effect of the Inlet Air Temperature on the Numerical Results

It is known the inlet air temperature is above that of the measured ambient air in the experimental due to the bottom ledge outside of the cavity being heated by the illumination system. However, an accurate value of the inlet could not be found from the current set up. A investigation was done numerically to account for the increase in the inlet temperature above the ambient. The investigation was done by changing the inlet air temperature in the numerical simulations to be higher than that of the ambient exit temperature. A comparison between the velocity profiles of the experimental and various numerical simulations that had different inlet temperatures can be seen in Figure 4.4.

Experimental location 3, the highest horizontal profile and least likely to be effected by recirculation, was selected for comparison on Experiment 6. The inlet temperature was increase by a degree Celsius until the mass flow rate of the numerical was higher than what was found experimentally. For Experiment 6, this occurred at the numerical inlet temperature being higher than the ambient room temperature by 3 ^{o}C, so that the numerically predicted increase in inlet temperature is between 2 ^{o}C to 3 ^{o}C for this case. Figure 4.4 shows what is representative of all the numerical predictions for all the experimental configurations considered, that the velocity peak is much closer to the absorbing wall than the experimental results found. Also the numerical predicted a peak at the glass surface, but the experimental results do not show an increase in velocity at the glass surface. The increase in inlet temperature does not change the location or the magnitude of the velocity peaks in the numerical simulation, but rather increases the velocity of the fluid in the middle of the channel. This brings the numerical simulation velocity in the middle much closer to what was measured in the experiment. One can see from the comparisons of mass flow rate that a few degree temperature change at the inlet can have a large impact on the flow rate, with a 3 ^{o}C increase more than doubling the mass flow rate compared to case with the inlet temperature equalling the ambient.

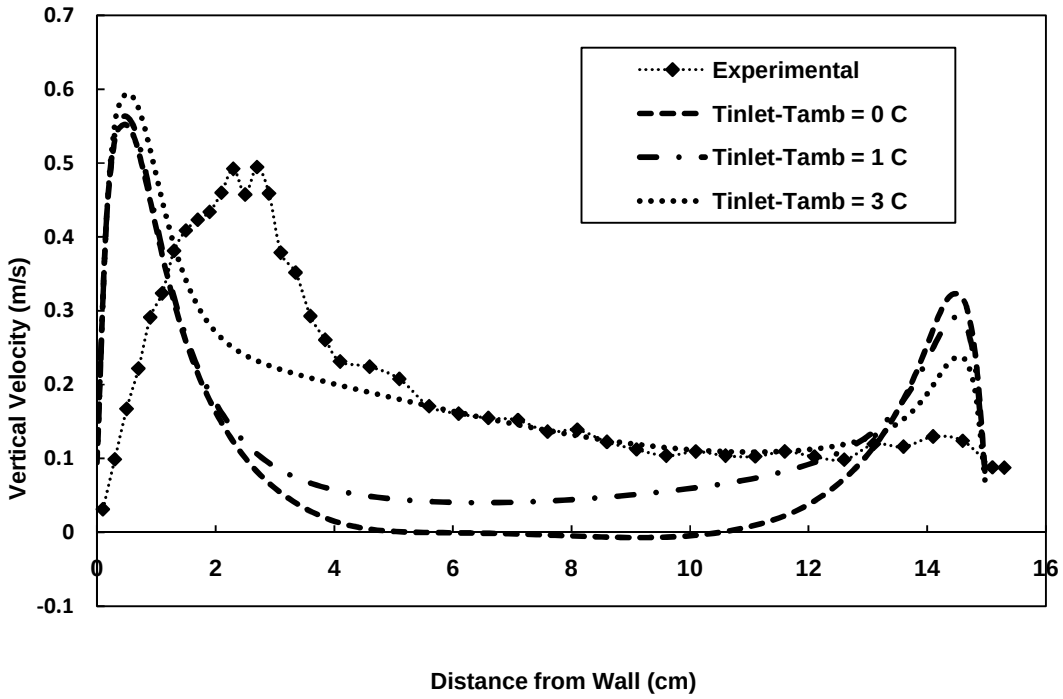

Figure 4.4: Velocity comparison at Location 3, for Experiment 6, between the experimental, with a 0.0332 Kg/s per m width mass flow, and the numerical simulation, with T_{inlet} - T_{amb} equalling 0 ^{o}C, 1 ^{o}C and 3 ^{o}C, having 0.0165, 0.0225 and 0.0344 Kg/s per m width mass flow respectively

A comparison between the numerical temperature and velocity profiles for the case when the inlet temperature as the same as the ambient and when the inlet temperature was increased to match the mass flow rate between the numerical and experimental for Experiment 6 is seen in Figure 4.5 - 4.8. The velocity profiles change as the case with the inlet temperature higher than the ambient has a higher mass flow rate. The temperature profiles keep the same shape but shift up in the case with the inlet temperature higher than the ambient. A comparison of the velocity vectors on top of a temperature contour for the two cases for Experiment 6 can be seen between Figure 4.9

and Figure 4.10. The velocity vectors for the case with the inlet temperature equalling the ambient are largest close to the vertical walls and near zero in the middle of the vertical channel. The velocity vectors for the case with the inlet temperature higher than the ambient are more uniform in magnitude across the vertical channel.

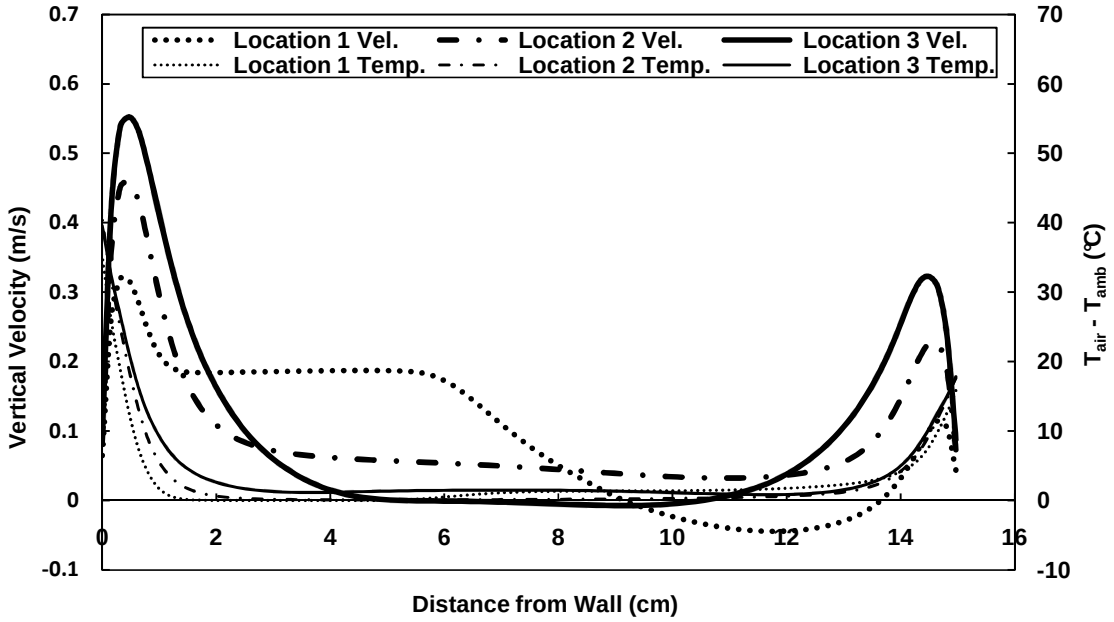

Figure 4.5: Numerical horizontal velocity and temperature profiles for Experiment 6, B/H = 0.133, outside vertical center average heat flux = 380 W/m^2, $T_{inlet} = T_{ambient}$

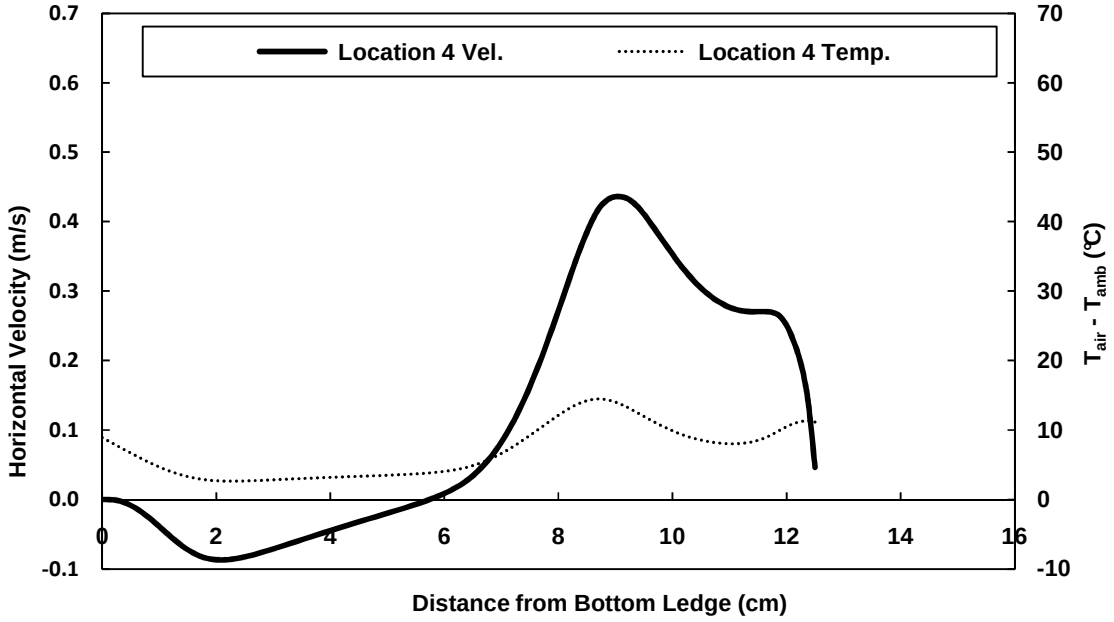

Figure 4.6 Numerical vertical velocity and temperature profiles for Experiment 6, B/H = 0.133, outside vertical center average heat flux = 380 W/m^2, $T_{inlet} = T_{ambient}$

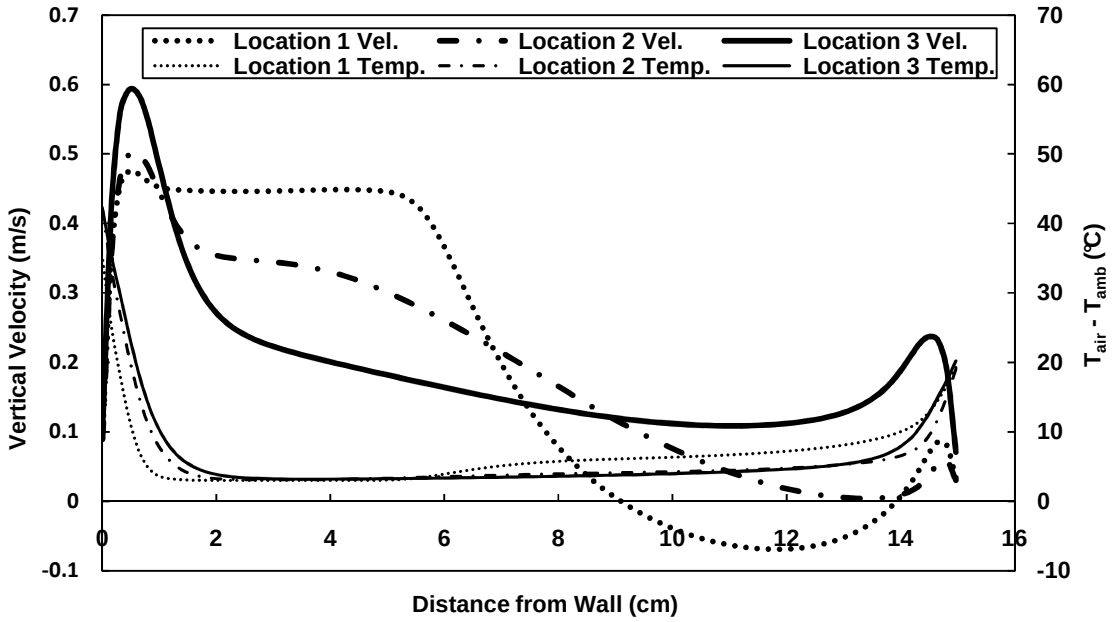

Figure 4.7: Numerical horizontal velocity and temperature profiles for Experiment 6, B/H = 0.133, outside vertical center average heat flux = 380 W/m^2, $T_{inlet} - T_{ambient}$ = 3 ^oC

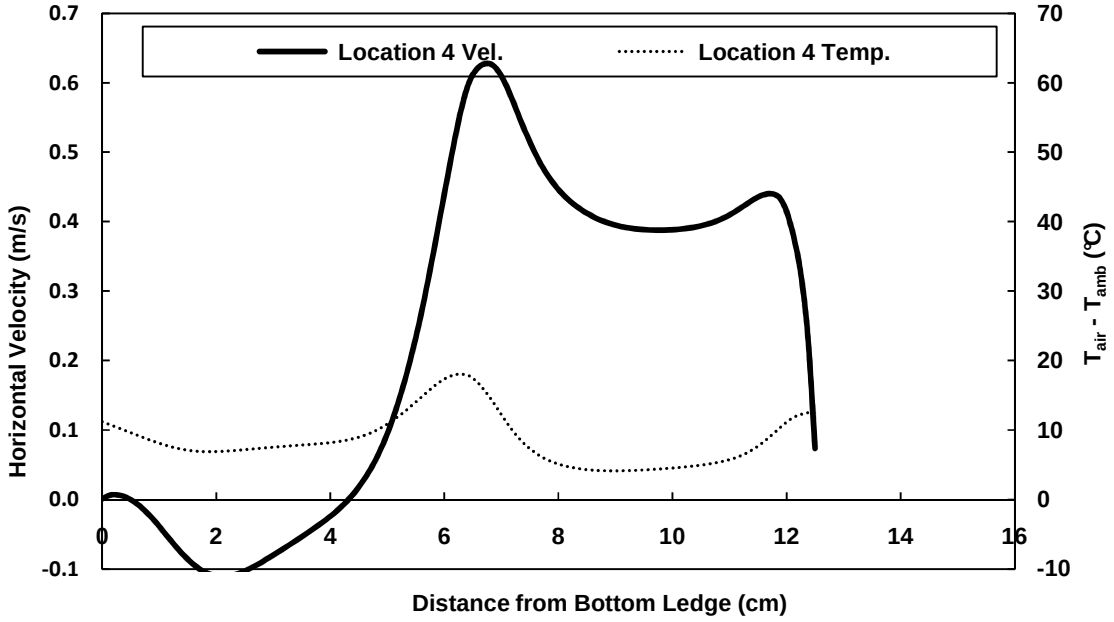

Figure 4.8: Numerical horizontal velocity and temperature profiles for Experiment 6, B/H = 0.133, outside vertical center average heat flux = 380 W/m^2, $T_{inlet} - T_{ambient}$ = 3 ^oC

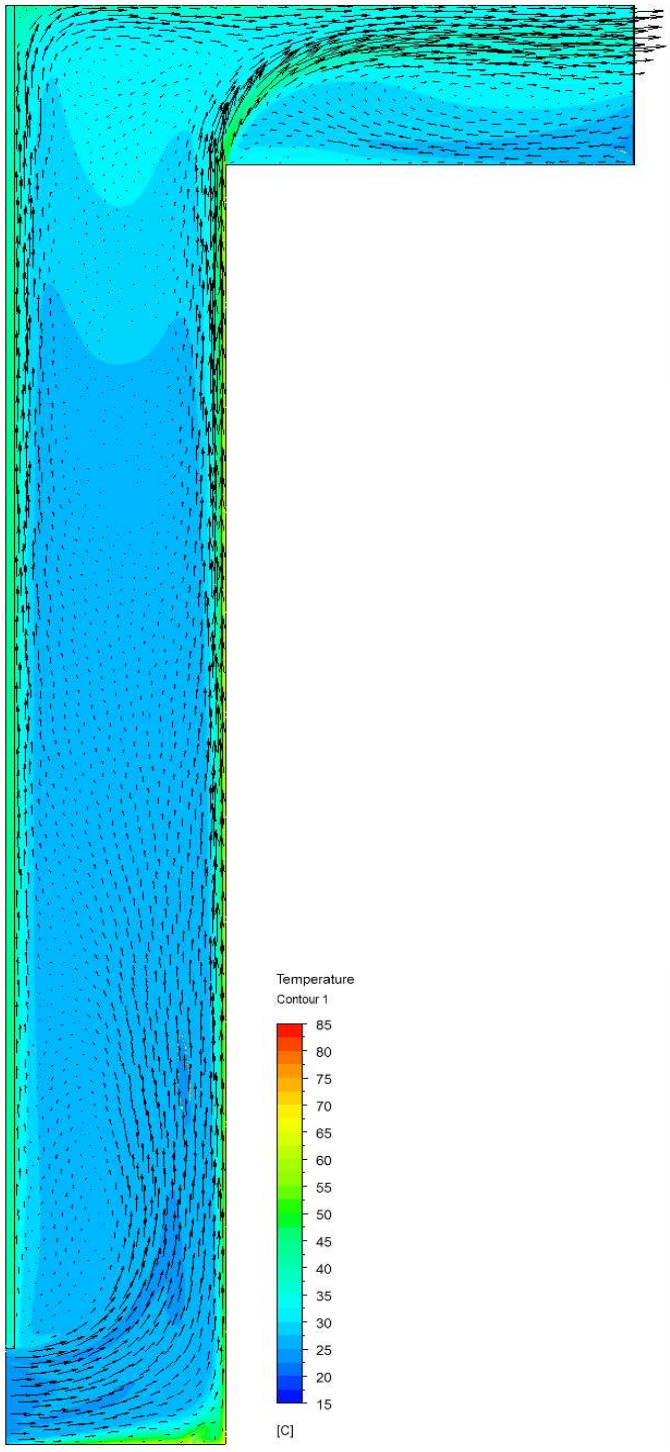

Figure 4.9: Numerical velocity vectors on top of temperature contour plot for Experiment 6 with $T_{inlet} = T_{ambient}$

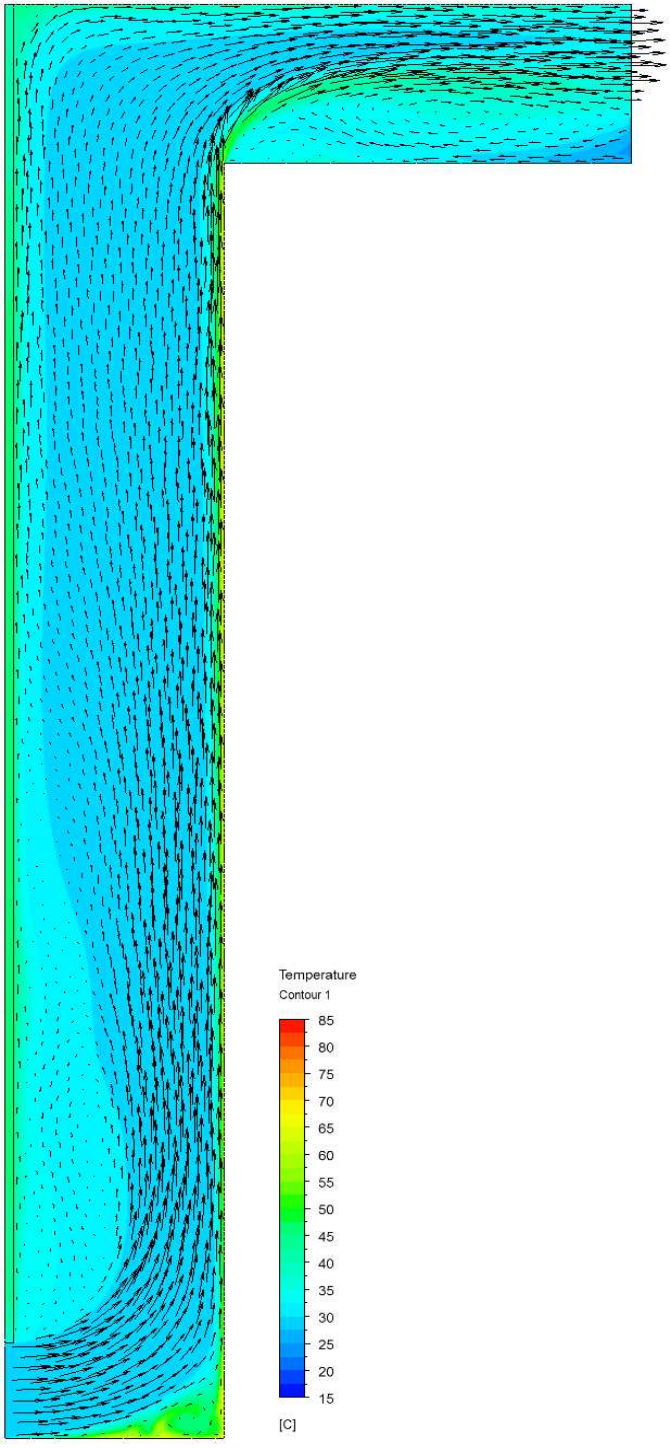

Figure 4.10: Numerical velocity vectors on top of temperature contour plot for Experiment 6 with $T_{inlet} - T_{ambient} = 3\ ^{o}C$

The same methodology of increasing the numerical inlet temperature to match the mass flow rate between the numerical and the experimental was applied to all six experiments. The mass flow rate can be compared between the numerical and experiment with a given increase in inlet temperature as seen in Table 4.2. The mass flow rates can be perfectly matched by changing the inlet temperature. The trend for the required inlet temperature that makes the mass flow rate match follows the physics of the experimental set up. Experiments 1, 2 and 3 had a higher heat flux applied so there was more energy to heat the bottom ledge relative to experiments 4, 5 and 6. This is why the inlet temperature is higher in experiments 1, 2 and 3. The inlet temperature drops as the B/H aspect ratio gets larger and more mass flow goes through the cavity. The constant heat input from the bottom ledge is transferred in to a larger mass of air as the B/H aspect ratio gets larger. Following an energy balance, when the same amount of energy is transferred into a larger mass the increase in temperature of the mass is less than the increase for a smaller mass. So given the trends in the inlet temperature following explainable physics more confidence can be placed in the numerical model.

A spot check of the inlet temperature was done for Experiment 2. A thermocouple was placed at the inlet plane, 5.0 cm above the bottom ledge. To prevent heating from solar radiation the thermocouple was shaded. However, the shading device would have disturbed the flow into the inlet, changing the flow pattern the thermocouple was trying to measure. This would change the temperature measured compared to the non-disturbed flow case. The thermocouple in this location reached a steady state value of 29.8 ^{o}C and the ambient air temperature was 23.6 ^{o}C, giving a 6.2 ^{o}C increase in the inlet temperature measured at this location. This does show experimentally that there was an

increase in air temperature at the inlet. However, this value is not likely to represent the mass flow averaged inlet temperature as both the temperature profile and the velocity profile are required for that value. Due to the bottom ledge being close to the ground, a traverse could not be placed between the bottom ledge and the ground to get the temperature and velocity profile at the inlet. An increase of 4 ^{o}C in the inlet temperature above the ambient was required for the numerical mass flow rate to match the mass flow rate calculated for Experimental 2. This is close to the single value of 6.2 ^{o}C measured in the experiment. This verifies that the numerical and experimental inlet temperature increase above the ambient is comparable.

Table 4.2: Experimental and numerical mass flow with inlet temperature increase comparison

Experiment	Mass Flow Experimental (Kg s^{-1} m^{-1})	Mass Flow Numerical (Kg s^{-1} m^{-1})	Difference (%)	T_{inlet} -T_{amb} Experimental (^{o}C)
1	0.0348	0.0313	9	7
2	0.0361	0.0370	2	4
3	0.0395	0.0361	8	3
4	0.0295	0.0308	4	6
5	0.0302	0.0315	4	3
6	0.0332	0.0345	4	3

The surface temperatures were also collected with hopes of assisting in validating the numerical model. A comparison of the centered vertical surface temperatures for Experiment 6 between the experimental data and the numerical simulation that had the closest mass flow rate, T_{inlet} - T_{amb} equalling 3 ^{o}C, can be seen in Figure 4.11. The numerical and experimental trends are very close, however the numerical is offset by an almost fixed amount which is well beyond the experimental uncertainty. There are a few possible reasons for the numerical predicting surface temperatures higher than the experiment. The assumed natural convection heat transfer coefficient on the outside of

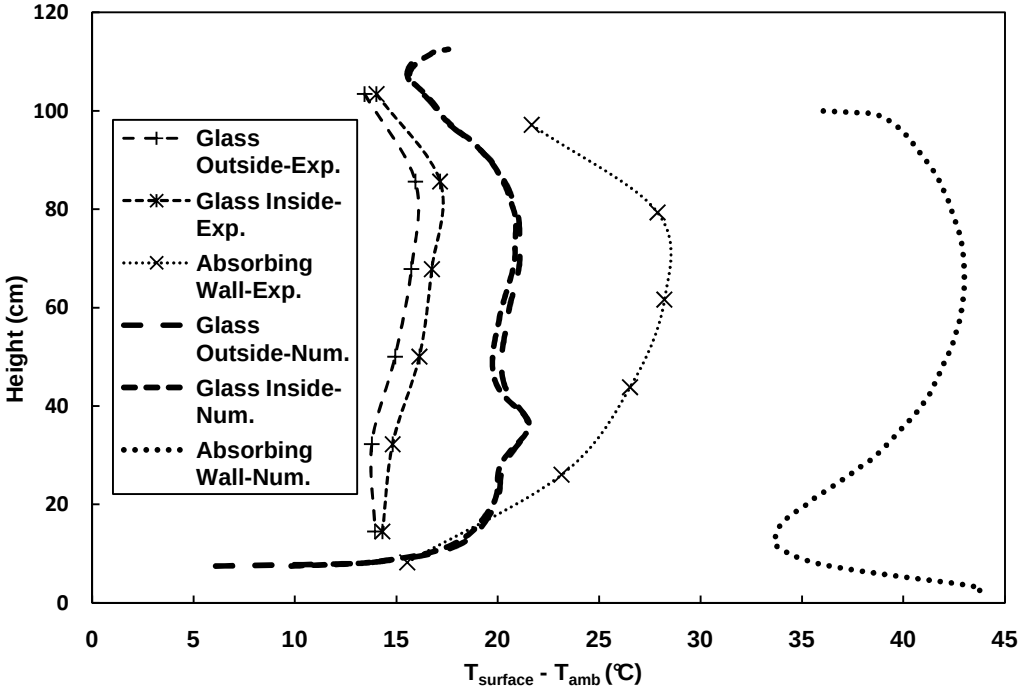

Figure 4.11: Central vertical surface temperature comparison for Experiment 6, between the experimental and the numerical simulation, with T_{inlet} - T_{amb} equalling 3 ^{o}C

the glass may be too low for what happens in the experiment, resulting in lower temperatures experimentally in the glass. The assumption of the solar radiation energy

absorbed in the glass may be too high. The absorbing wall is assumed to be perfectly insulated in the numerical case, when the experimental would have some heat transfer through the insulation, resulting in a lower temperature experimentally. Another unknown factor is the convection heat transfer coefficient off the absorbing wall and the inside of the glass. The numerical model may be calculating to low of a heat transfer coefficient compared to the real case. Given the large number of possible reasons for the temperature difference between the numerical and experiment, it is clear more experimental investigation would be required to clarify the assumptions used in the numerical model.

To improve the confidence in the numerical model another parameter was examined once the mass flow rate was matched between the numerical and the experimental data by changing the inlet air temperature. The temperature difference between the numerical mass flow averaged exit temperature and the imposed numerical temperature that the air exits into at the outlet, which is representative of the ambient air temperature, is compared with the experimental mass flow averaged exit temperature increase above the room temperature in Table 4.3. It can be seen that except for the experiments with a B/H aspect ratio of 0.044, the mass flow averaged exit temperature above the room temperature was within 1 ^{o}C for the experimental measured results compared to those predicted by the current numerical set up. This adds the more confidence to the numerical model being able to predict the performance parameters accurately.

It has been shown that the numerical model is capable of predicting the major outputs of interest for SAW operation, mainly mass flow rate and thermal efficiency. However, given that there are still unknown values in the experiment that were assumed

in the numerical set up, and that the numerical simulations with B/H aspect ratio of 0.044 have a much larger temperature increase discrepancy and the reason not known, more work can be done to improve the confidence in the validation of the numerical model.

Table 4.3: Experimental and numerical mass flow and temperature increase comparison

Experiment	$T_{exit} - T_{amb}$ Experimental (^oC)	$T_{exit} - T_{amb}$ Numerical (^oC)	Difference (%)	$T_{inlet} - T_{amb}$ Experimental (^oC)
1	16.0	20.5	28	7
2	13.4	13.1	2	4
3	12.4	12.1	2	3
4	10.1	12.8	27	6
5	9.8	10.5	7	3
6	8.8	9.4	7	3

4.9.1. Effect of Inlet and Outlet Bends on the Numerical Results

Due to the independence of the mass flow on the B/H aspect ratio for the numerical results when the inlet temperature was the same as the ambient, quantifying the pressure drop due to the inlet and outlet bends was of interest. To quantify the increase of pressure drop due to the flow turning at the inlet and outlet in the current supply mode configuration, the current setup was compared with a simple parallel plate configuration. An average heat flux of 400 W/m^2 was applied to one wall of the parallel plate cavity. This is the same average heat flux that was applied in the numerical supply

mode setup of for Experiments 1, 2 and 3. All the boundary conditions were the same between the parallel plate case and the supply mode including the glass domain volumetric heating and heat conduction. The same infrared radiation heat transfer model was used in both numerical cases. The only difference was height of parallel plate cavity and the location of the inlet and outlet. The height of the parallel plate cavity was 1.0 m high as this is the same height that energy is added on the supply mode cavity. The height of the supply mode is 1.125 m due to the extra height of the horizontal outlet. The only effect on the mass flow rate through the cavity between the two configurations should then be the pressured drop added by the flow bending around the inlet and outlet in the supply mode. A comparison between the numerical results can be seen in Figure 4.12. The numerically calculated mass flow rate for the parallel plate configuration is predicted to be considerably higher than the results for the numerically calculated supply mode configuration. This difference is likely due to the added pressure drop in the supply mode configuration from the flow having to turn around the inlet and outlet and the recirculation zones these bends induce. Also the mass flow rate for the parallel plate configuration is numerically predicted to increase with higher B/H aspect ratio. The numerically predicted mass flow rate for the supply mode configuration does not change with the B/H aspect ratio for this range. This numerical comparison shows that there is likely a large increase in pressured drop due to the inlet and outlet bends in the supply mode configuration over the parallel plate configuration, and this inlet and outlet pressure drop increases proportional with increasing B/H aspect ratio.

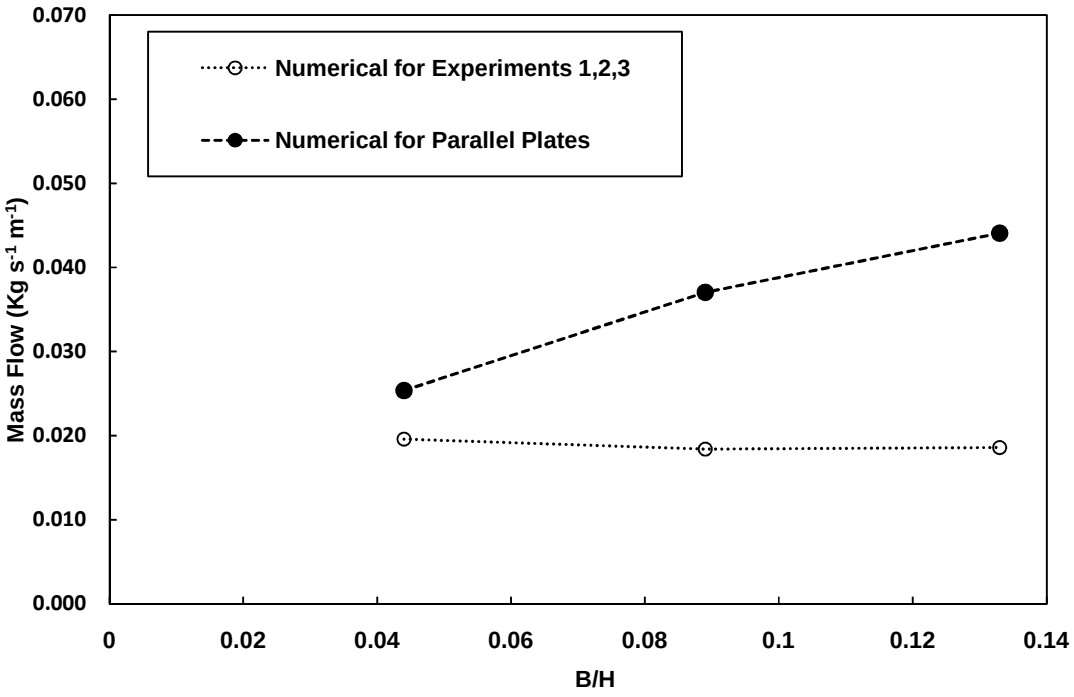

Figure 4.12: Numerical mass flow rate comparison between parallel plate cavity and the supply mode for the same boundary conditions for Experiments 1, 2 and 3 with $T_{inlet} = T_{ambient}$

4.10 Numerical Comparison with Previous Experimental Work

The numerical results for the inlet temperature equalling the ambient temperature are compared to previous experimental work shown in Figure 4.13. Again this was done by using the correlations developed from previous experimental work.

The work of La Pica et al. (1993) was used as it was an experimental setup of a indoor air curtain which has the most similar boundary conditions as the current experimental work. Ryan and Burek's (2010) work was used as it is the most comprehensive study to date, allowing for adjustment of the height to be included.

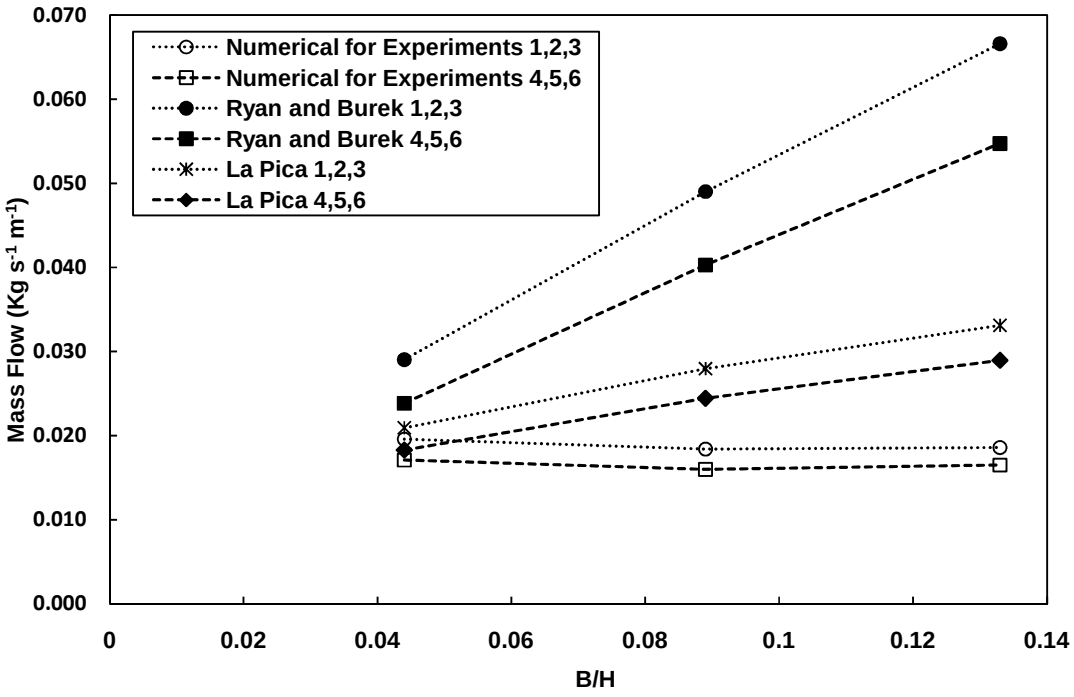

Figure 4.13: Comparison of the numerical model for $T_{inlet} = T_{ambient}$ with previous experimental researchers of Ryan and Burek (2010) and La Pica et al. (1993)

The numerical results where the inlet temperature is the same as the ambient temperature compares well with the pervious experimental work. The numerical mass flow rate is lower for all of Ryan and Burek's experimental results as expected. This is because Ryan and Burek's work was on a parallel plate cavity which as discussed in experimental results chapter has lower pressure drop and hence would have a higher mass flow rate for the same driving force. The numerical results are very similar to La Pica et al. as expected since the boundary conditions are almost the same. As was expected when the preheating of the air on the bottom ledge was removed from the numerical results, the results became more comparable with the experimental work that did not have any preheating. The discrepancy between the numerical results and the

experimental is that the numerical does not show increase in mass flow rate for an increasing B/H aspect ratio. Experimental results suggest there should be some dependence of the mass flow rate on the B/H aspect ratio. A reason for the numerical not showing this dependence could be the large numerically calculated pressure drop from the inlet and outlet bends as discussed in the prior section. Other uncertainties could also contribute to the difference between numerical and experimental results.

4.11 Correlation Developed from the Current Numerical work

The flow rate correlation based on current numerical work, where the inlet temperature is the same as the ambient temperature, for a solar thermosiphon in the supply mode is:

$$Re = 0.1259\, {Ra_H}^{0.310} \left(\frac{B}{H}\right)^{-0.047}$$

The correlation coefficient R^2 is 0.94, showing very good fit with the numerical data. Unlike the correlation developed from the experimental results this numerical correlation is not dependant on the preheating boundary condition. This makes the numerical correlation more robust than the experimental correlation. However, due to the numerical results not showing a dependence of the mass flow rate on the B/H aspect ratio, which all experiments have indicated there is including the current one, the accuracy of this correlation for B/H aspect ratios different from 0.044 is questionable. Again like the experimental correlation, the numerical correlation would over predict the flow rate in real solar thermosiphons in supply mode, as the inlet temperature in the real case is lower than the air temperature at the outlet.

Chapter 5

5. Practical Implementation

5.1 Case Study of SAWs

To give an indication of what the numerical results mean in a real world situation a case study was developed for a office building located in Ottawa. A 45 m by 45 m square floor plan that was 25 stories was assumed, with a capacity for 5000 people. If there is three meters per story, and no shading on the building, there is 3,375 m^2 of south facing area exposed to the sun. Based on ASHRAE Standard 62.1 (2007), 20 CFM (10 L/s) per person is required in an office building to maintain the current standard of air quality. This gives a ventilation load of 50,000 L/s during occupied hours. The one meter high SAW would be placed in the spandrel areas, and given that the stories are three meters high, the one meter high SAWs will cover 30% of the south facing area.

Having a SAW operating in supply mode in the winter time is the most advantageous set up, as this provides fresh air as well as heating the fresh air. A day in January was selected to be the representative day for this case study. Reported by ASHRAE Fundamentals Handbook (2009) the average temperature for Ottawa is -10 ^oC in January. Assuming no humidity, the energy requirement to heat the 50, 000 L/s of outside air to 21 ^oC is 1.822 MW. With 30% of the south facing area being used and an average heat flux of 380 W/m^2 for a 7.5 hour period there is a max potential of offsetting 0.385 MW or 21% of the thermal load for ventilation.

By changing the inlet temperature in the numerical model to account for the cooler outside temperature, the current numerical model can be used to predict the

performance of the system. The average daily heat flux on a perfectly clear day was used, 380 W/m^2 on the outside of the glass. The B/H aspect ratio was 0.10. The flow rate turned out to be 0.0041 Kg/s per meter width with a mass flow averaged temperature increase of 56 ^{o}C. Multiplying the mass flow by the 30% of the area used gives the total average flow rate, which is 3,206 L/s or 6% of the ventilation load. Multiplying the temperature increase by the mass flow rate to find the amount of thermal load for ventilation that is offset by the SAW gives 0.217 MJ or 12%. A SAW in the indoor air curtain mode with the same thermal efficiency would also be able to provide the same amount of offset for the thermal load for ventilation.

The case study shows that a SAW in supply mode does have the potential to offset some of the ventilation load when the conditions used for deriving this case study are met. However, these optimal conditions are not always met and there are many practical implementation problems that must be overcome for a SAW in supply mode to perform at this expected level.

5.2 Practical Implications for the operation of SAWs

Some practical implications can be drawn from the analysis of solar thermosiphons. The largest practical reason for not implementing a solar thermosiphon is controlling the air flow rate and direction. With no external pressure on the system, and with solar radiation, the supply mode can provide desired warm fresh air in winter time passively. When these conditions are not met, and there is no control of the flow rate and direction, a SAW can be detrimental to the energy efficiency of a building. A SAW setup for supply mode can operate in exhaust mode, allowing warm air to exit the

building in winter time, much like a open window would, increasing the heating load of the building. There are many causes of this backwards flow. External pressures on the SAW such as being on the leeward side when wind is blowing on a building, stack effect above the neutral pressure line in a building, and a mechanical ventilation system that is pressurizing the building will force air to exhaust out through SAWs when the desired is to supply hot air with them. Also when no radiation is incident SAW, such as night time on the, the warm inside air that contacts the glass will cool and fall, resulting in exhaust by sucking air out of the building.

The simple solution to preventing SAW from running backwards is to install a one way valve, only allowing flow into the building not out. Implementing such a valve becomes quite the problem, as the pressure generated by SAWs to drive flow into the building is very minimal, so the valve would need to be very sensitive to small pressures. Implementing a pressure activated one way valve increases the pressure drop in the system, resulting in lower flow rates, reducing the benefit of the system. Due to the wind being variable, the one way valve has to be very responsive in closing fast to prevent back flow of the air. Fast responding valves to low pressures need to have very low inertia, making the valve light and flimsy, likely leading to maintenance problems if not properly designed. Also these valves must span large widths, making large aspect ratios, reducing their rigidity. Putting more than one valve across the width span of a SAW is possible, but the area between valves will not allow air flow, and increasing the pressure drop of the whole system reducing the flow rate.

The external pressures that will increase flow rate through a SAW in supply mode such as being on the windward side when wind is blowing on a building, stack effect below the neutral pressure line in a building, and a mechanical ventilation system that is

depressurizing the building, are not always desirable. Although the ventilation rate in the building will have gone up, a beneficial feature, the temperature of the air entering the building can be quite different from the desired temperature, resulting in discomfort to the occupants near the SAW outlet. Controlling this is not as simple as a one way valve. A valve must operate based on the exit air temperature of the SAW. This posses a considerable problem as the maximum desirable flow rate is that which allows the fresh air to be heated up to the desired conditioned space temperature. A flow rate higher than this will result in the fresh air being cooler than the conditioned space. So given the external pressure can change, particularly with wind, the temperature controlled valve has to change the pressure drop so that the desired flow rate is maintained. This requires a control system, adding to the complexity of implementing a SAW in supply mode.

The occupants in the conditioned space want to be at a temperature they find comfortable. One of the problems for SAWs in supply mode is the temperature and humidity of the air they deliver. It has been mentioned that for no other external pressure forces, the supply mode will only deliver air that is hotter than the air it is exiting into. This removes any worries of condensation developing during the normal operation of the SAW, but condensation can be a concern in periods the SAW is not heated, leading to the related mould problems. The air supplied being hotter than what it is exiting into removes the worry of chilling the occupants with this passive method, which is a major concern for active transpired solar air heating systems. However, there is a potential for overheating the occupants that are close the thermal envelope. So where and how the fresh supply air enters the building is of importance. Humidity being too low may also be a problem as cold air does not hold much moisture and when heated will be even less

humid. Since this air is warmer, it will tend to rise and stratify on the ceiling, and typically be out of contact with the occupants. While rising and stratifying along the ceiling, this air will mix with the air in the room, cooling the supply air from the SAW but raising the overall temperature of the room. So the degree of discomfort from overheating decreases the further the supply air enters into the building. The depth into the building this fresh supply air goes depends how the air is exiting the building, and unless the air is being drawn up a central column to exit the building is not likely to penetrated deep into the building without the help of a mechanical ventilation system.

Since buildings cannot be substantially pressurised, mass flow into the building must equal mass flow out of the building. So this means the same amount of air that is entering the SAW in supply mode must be leaving the building someplace else. For a typical commercial building, this would be accomplished by return air ducts if the mechanical ventilation system is on. If no return system is on, then the SAWs actually have to pressurize the building, and drive flow out ventilation ducts, or holes in the thermal envelope. For very airtight buildings with no vents open, this could stop the flow of air through SAWs, as no air can be removed for the fresh air to replace it. This complexity of the pressure and flow rates into and out of the building, makes it difficult to integrate SAWs into the building envelope, but will have a profound effect on the flow rates that can be provide by SAWs in supply or exhaust mode.

The one constant is that thermal energy can still be provided by the SAW no matter how small the flow rate, as the lower flow rates will result in higher absorbing wall temperatures and hence higher exit air temperatures. Of course with higher cavity temperatures comes the ability to generate more hydrostatic pressure to drive the flow. The limiting condition for this is that the flow is stopped, most likely by a valve. The

location of this blockage will matter. For supply mode, if the blockage is at the bottom inlet, the air in the cavity can still rise up and exit into the building at the top, with the colder air being sucked into the top of the cavity. If the blockage is at the top of the cavity, the SAW will be stagnated, and this is most likely to occur in the summer when no heating is desired from the SAW. Here the absorbing wall will continue to heat up, heating the air in the cavity, which will rise to the top of the cavity, then will come into contact with the cooler window glass and fall as it becomes more dense, creating recirculation in the cavity. The absorbing wall will heat up till the heat lost off it due to radiation and convection to the outside and conduction to the inside balances the heat coming in. If the glazing is well insulated and the outside temperatures are high, the absorbing wall can reach temperatures well over 100 ^{o}C just like a solar cooker. This can cause fire risk, thermal stress problems as well as increase the heat going into the building through conduction in the summer time which is undesirable. These cost maybe out weight any benefit the SAW provides in the winter time. To reduce the cavity temperatures due to stagnation, one can shade the window from the outside, which reduces the heat flux on the absorbing wall to near zero, or to have a vent at the top on the outside to allow the cavity to run in the outdoor air curtain mode, cooling the absorbing wall with the outdoor air. The outer shading provides the most benefit in the summer from an energy standpoint, however may not be aesthetically pleasing, and can difficult to implement on curtain wall buildings.

With the validation of the current numerical model a concern is brought up about the practically of the supply mode of a solar thermosiphon operating at its most advantageous time, in winter. The case study for the optimal conditions showed that only 6% of the mass flow for ventilation could be met. Given the fact that not every day is

always sunny, the ventilation potential of the decreases when averaged over a month. Just from the number of cloudy days in Ottawa, which only allow diffuse radiation to fall on the SAW, the monthly average of the mass flow ventilation load that could have came from the SAW in supply mode is 4%. Taking into account the practical requirements of a valve, a screen cover, and possibly a filter, the pressure drop will increase in the cavity, and we can expect the flow rate to decrease even more.

Due to the low flow rates of a practically implemented SAW in supply mode in winter time, it is unlikely a SAW in supply mode would justify the energy saved in not mechanically pumping the ventilation air into the building compared to the extra energy needed due to losses of the SAW during non sunny periods, and certainly would not justify the extra costs of the control system. The much more practical way to implement a SAW is the indoor air curtain mode, like a Trombe Wall. In this mode the solar thermosiphon would still provide significant thermal energy which is of value and all the concerns with external pressure forces causing loss of conditioned air would be removed, removing the need for complex control systems, and a simple one way valve would work to reduces cooling of the building in non sunny periods. The thermal energy from the indoor air curtain mode would be used to replace the heat lost by conduction through the walls, and if not all the energy was used for that, the remaining energy would heat the return air going to the mechanical ventilation system. Since most return air is mixed with incoming ventilation air, or sent through a heat recovery ventilator, the ventilation air will still be partially preheated by the solar thermosiphon, reducing what is likely fossil fuel derived energy to fully condition the incoming ventilation air. So the indoor air curtain mode will provide the same thermal energy as the supply mode, and not have the risk of allowing for exfiltration of already conditioned air as the supply mode

wound. So the supply mode's small benefit of reducing mechanical fan energy by naturally pumping a small amount of fresh air into the building, does not justify the cost of the control system to reduce the many negative side effects that could lead to the SAW wasting more energy than it saves when the indoor air curtain could be used.

As with the supply mode, the indoor air curtain has the potential to overheat building occupants close to the SAW when it is sunny out. To prevent this the mechanical ventilation system has to be designed to either mix the warm air coming from the solar thermosiphon or suck it into the return lines right away. Also, there is still the same concern with the indoor air curtain heating the building in the summer when it is not required if the thermal energy it is designed to gather is not dissipated in some way. The passive solar method of a solar thermosiphon without shading will result in more air-conditioning energy use to remove heat from the building in the summer compared to a active transpired solar air heater which are located on the outside of the thermal envelope. So from a year round perspective an active transpired solar air heater will gather the same amount of thermal energy as a SAW, however the active transpired solar air heater is not going to increase the cooling load as much in the summer time, making it more energy beneficial than a passive system.

The only time a passive solar thermosiphon will be better than active transpired solar air heater is when ventilation is not needed, as active systems need to drawn in fresh air to work, making the indoor air curtain mode the configuration of choice. The need for thermal energy but not ventilation would only occur in periods of low to no occupancy, such a residential homes during the weekdays, and office buildings on the weekends.

These discussed practical implications bring up considerable concern about the benefit of solar thermosiphons, particularly the supply mode. If not addressed properly it is quite possible for solar thermosiphons to end up using more fossil fuel derived energy than they offset. From the case study and this discussion it has been shown the benefit of the ventilation from a SAW in supply mode is very minimal. The indoor air curtain mode of a solar thermoshipon is much easier to implement practically while still providing the same thermal heating benefit as a supply mode.

Chapter 6

6. Summary and Conclusions

An investigation of the benefit of using SAWs in buildings has been carried out. From the literature review done it was found there was no comprehensive correlations that accounted for the various parameters that affect the performance of SAWs especially in supply mode. These correlations are needed for performing a year round building energy simulation that would calculate the annual benefit of SAW. It was then decided a CFD parametric study would be done to determine the correlations needed for a year round building energy simulation of a SAW. A numerical model was developed with the ANSYS CFD software package. To have confidence in the CFD numerical model it was validated with results from a new comprehensive experiment. The experiment included radiation as the heat source, a feature which has not be used in pervious experiments investigating solar thermosiphons. The testing apparatus allowed for adjusting geometrical parameters such as the spacing between the glass and the absorbing wall, the inlet and outlet height, and also changing the radiation intensity. These parameters have been noted by previous experimental researchers to have an effect on a solar thermosiphons performance.

Six configurations were tested with the experimental apparatus. The average outside of the glass vertical center line radiation intensities were 600 W/m^2 and 380 W/m^2 each with three B/H aspect ratios of 0.044, 0.089 and 0.133. The thermal efficiency only increased 1% with a higher radiation intensity, and remained constant for the varying B/H ratio. A correlation for the flow rate was developed from the experimental data. The mass flow increases with the heat flux to the power of 0.40. The

mass flow increases with the B/H ratio to the power of 0.10. The correlation developed from experimental results is limited to accurately predicting the performance of solar thermosiphons with the same boundary conditions. The boundary conditions that are not typical in a solar thermosiphon that are included in the correlation developed from experimental results are preheating of the bottom ledge and the three dimensional effects caused by the non-uniform heating from the illumination system.

The numerical model was developed to include effects such as thermal radiation heat transfer in the cavity, glass conduction and volumetric heating all which have not been included in previous numerical models of solar thermosiphons. The inputs from the experimental setup were used in the numerical model, so that a validation could be done. Some inputs into the numerical model had to be assumed as they were not measured in the experiment. The most significant of these was the mass flow averaged inlet temperature. The lack of knowing inlet air temperature in the experiment was overcome by comparing the mass flow averaged exit temperature with the ambient room temperature. Once the inlet temperature was adjusted in the numerical model good agreement was found between the numerical and experimental for the important parameters such as mass flow rate and efficiency. Since solar thermosiphons typically do not have heating of the air before the inlet a correlation was developed from the numerical results where the inlet temperature equalled the ambient temperature. This correlation compared better with previous experimental work than the current experimental work that had preheating. However, the numerical correlation did not predict that the mass flow rate was dependant on the B/H aspect ratio when all experimental work, including the current experimental work, has shown this

dependence. Therefore more work needs to be done before numerical model can be validated and then used to generate correlations for year round energy simulations.

The numerical model was used in a case study for a office building located in Ottawa for the month of January. This case study showed the potential of a SAW in supply mode under optimal operating conditions. A discussion was done on the performance of SAWs in non-optimal operating conditions. The discussion on the practical implementation of solar thermosiphons in supply mode showed that extensive and complex control systems are need to provide the small ventilation potential of the supply mode, which easily can lose more energy than it saves without the control system. The indoor air curtain mode of a solar thermosiphon was able to provide the same thermal heating benefits as the supply mode, but without the complex control system needed to prevent infiltration and exfiltration in the supply mode. SAWs of all types could also increase the cooling load in the summer time if not managed properly, reducing their annual benefit.

Chapter 7

7. Recommendations for Future Work

Keeping in mind the goal is to reduce fossil fuel use in buildings, the future research should focus around this. The current study on the supply mode demonstrated the small amount of fresh air that could be provided by this mode. When looking at mechanical ventilation, the energy required to heat air is far greater than the energy required to pump it into the building. Most energy used to pump air in a mechanical ventilation system is to provide recirculation of air throughout the building through all the duct work, very little energy is used to draw air in from outside. Since SAWs are located on the outside of the building, and due to thermal stratification, they are unlikely to mix the fresh air they drawn in and provide it to most occupants in the building. So without considerably changing standard building design, a mechanical ventilation system is needed to mix the fresh air SAW's provide, requiring most of the energy for recirculation still be used. So unless the research on changing the geometric parameters is going to result in flow rates than where 10 times higher what was found in the current work and the ability to provide mixing throughout the building, optimizing for mass flow should not be a concern compared to optimizing for thermal efficiency. On top of this, optimizing for mass flow at a zero pressure differential between the inside and outside is quite pointless due to other variable pressure forces that are going to effect the flow rate much more than the geometry ever will. The only time geometry will have substantial effect on flow rate will be when there are no external forces, which only happens in the indoor and outdoor air curtain modes. So continuing experimental research on the supply mode to

find the optimal mass flow geometry has little practical significance, other than to compare a supply mode's optimal spacing to the optimal spacing of other solar thermosiphons.

The fresh air provided by a SAW in supply mode is no different than the that provided by infiltration through holes in the thermal envelop of the building. The fresh air from both these sources will not likely become properly mixed to provide benefit to the occupants of the building without a mechanical ventilation system. The only difference in fresh air provided is when it enters the building. SAWs in supply mode with a one way valve should only provide fresh air during the day, when it is expected the building is occupied and ventilation is required. Infiltration happens all the time, so during the day this is beneficial as fresh air is required for a occupied space, however at night time, when no one occupies the building and ventilation is not required, infiltration becomes an unnecessary heating load. However, SAW in supply mode have the same problem in non-occupied periods such as the weekend. Here the SAW will be heating up fresh air when it is not required in the building, providing little to no benefit at this time. If the indoor air curtain mode was used, it would offset thermal heating requirements in the building in non-occupied times. It is almost without a doubt that the thermal energy offset by the indoor air curtain in these non-occupied times, would be greater than the ventilation pumping energy not used when implementing the supply mode during occupied times.

So given that higher thermal efficiencies of solar thermosiphons will offset more external energy than higher flow rates will, the focus should be on finding ways to reduce losses. From the outset this seems quite trivial, as more insulation will reduce losses of the back and sides. With almost any level of insulation what becomes more important for

utilizing solar energy is the optical properties of the system. Optical properties have be studied in great detail in standard flat plate solar thermal collectors and the findings in this field would be directly applicable to the current study of solar thermosiphons. So having dealt with conductive and radiation losses, all there is left is convective losses. The outside surface is exposed to the weather, and beyond the control of the designer, so what is left is the convection on the inside of the cavity. From the current work and other studies changing the spacing between the glass and the absorbing wall had little effect on the thermal efficiency. So from a thermal efficiency point of view, the effects of changing different parameters have all be research and found, all that is left to do is quantify the exact thermal efficiency for a given set of parameters. The summation of this would be a multivariate analyse of all the important parameters leading to correlations for implementation in year round building energy simulation.

As discussed before in the practical implication section, the indoor air curtain mode of a solar thermosiphon is much more likely to offset more external energy used in buildings than the supply mode. The indoor air curtain is much easier to implement in a practical sense and research of it is much simpler as there is essential no pressure difference between the inlet and outlet, and the temperatures of the air at the inlet and outlet are the same. If it wasn't for the location of the inlet, the current study would have been for the indoor air curtain. As mentioned in the experimental results section, results found in the current work were all almost the same as other researchers that investigated the indoor air curtain. This is because the boundary conditions were applied. Researching the indoor air curtain would be the easiest to implement with the current equipment, as only adjustments to the testing apparatus frame need to be done. Continuing research of the supply mode would required varying both the external

pressured difference applied across the SAW, and the inlet and outlet temperatures, which are much more technically challenging and expensive to implement. The one feature that would not be accounted for with the current equipment when performing experiments with the indoor air curtain mode, would be the outside temperature cooling the glass.

Experimentally researching the effect the of the difference between inside and outside temperature on the mass flow rate in supply mode will also have little practical significance as the external pressure forces will have a larger influence, and it is already known the bigger the temperature differential the lower the flow rate. Experimentally applying a pressure difference across the inlet and outlet of a SAW in supply mode and determining the efficiency and mass flow rate, would be useful as the pressure difference will have a large effect on the performance of the SAW. This data would be very necessary in a year round energy simulation, but work would have to be done to find how the external pressures of wind, stack effect and mechanical ventilation would add up to find the imposed pressure difference on the SAW.

Constructing a test facility to test the supply mode with different inlet and outlet temperatures and different external pressure differentials applied would also allow for testing the exhaust mode, a solar chimney, which could be used in the shoulder seasons of spring and fall. The requirement for the exhaust mode to be beneficial is the outdoor air being cooler than the inside air, and the internal gains in the building heating up the inside air above the desired temperature. Here ventilation and cooling can be provided passively. The application of this is very limited, as the cooling demands are very limited in these seasons. Also the flow rate would not be determined so much by the geometry and incident solar radiation, but by the external pressure forces of wind, stack effect and

mechanical ventilation, just like the supply mode. So in fact the exhaust mode will provided the same benefit as a regular operable window. The only time the exhaust mode will be better than a regular window, is on a sunny day, with no wind, located at the neutral pressure line of the building, with the mechanical ventilation system shut off. Here the solar thermosiphon can pump air out of the building when a open window cannot, but clearly this is a very limited application to have all these requirements met. The correlations found for the supply mode would almost be directly comparable to those of the exhaust mode, much like the correlations of the indoor air curtain mode would be the same as the outdoor air curtain mode.

Actually implementing a practical one way valve, screens or filters and seeing their effect on the performance on a solar thermosiphon would be beneficial as estimations to the reduction in flow rate could be made.

Almost as important as studying the performance of SAW in supply mode at optimal operating conditions, is studying them at non-optimal operating conditions such as night time, and summer time. This is because the increase in energy load during these non-optimal times could out weight the energy saved in optimal operation conditions. Correlations for the performance during the non-optimal operation conditions are required in a year round energy simulation, to fully account for the impact on the total energy used due to implementing SAWs.

It should be understood by now that to have a larger reduction in external energy used, a SAW would need to operate in different modes at different times of the year, so that the savings in one time of the year are not offset by losses at another time of the year. An example of this is the indoor air curtain in the winter time to add thermal energy to the building passively, but operating in the outdoor air curtain mode in summer to

prevent excess thermal energy the SAW absorbs from increasing the cooling load of the building. Research of a SAW with this switching capability could be done to get an accurate account for the effect of the additional inlets and outlets that are not always used. However, as mentioned before the correlations developed for an indoor air curtain would be similar to those for a outdoor air curtain mode, as all the boundary conditions are the same besides the absolute temperature of the air that goes through the channel, and the position of the inlets and outlets.

The best benefit would have a solar thermosiphon that could operate in all 4 modes. Although not all that technically challenging to build, what would be the difficulty is the switching between modes based on building demands and weather conditions. Given the rapid change in weather conditions, relying on a human to implement the change is not practical, and as such a highly automated system would be required.

If the supply mode is going to be continued to be researched in the current research group a few suggestions will be made. As noted before the time to perform one numerical simulation is much shorter than performing an experiment. With the current testing equipment to get all the temperature and velocity profiles it easily took ten times longer than running a numerical simulation. However, the numerical model could still benefit from some more experimental data to improve the validation.

To improve the accuracy of the experimental setup, either the bottom ledge that preheats the air inlet air must be removed and the solar radiation from the illumination system that falls there be removed from affecting the inlet temperature, or measurement of the mass flow averaged inlet temperature be taken. This would removed the inaccuracy of guessing the inlet temperature in the numerical model. Also the losses should be quantified. This not only includes those conducted through the sheet metal,

but also that which is conducted through the glass. Having this data would allow for a increase in confidence in the numerical model if it was still able to predict the same mass flow and temperature increase as the experimental measurements found.

The current numerical model does not model solar radiation, so the change in optical properties with changing glazing is not accounted for. So experimental tests should be done with different window panes to find the effect of the change of the optical properties which is beyond the current numerical model to account for.

Applying a pressure difference between the inlet and outlet should be done as this will have more influence on the mass flow rate than any other parameter. Only a few data points would be needed to validate that the numerical model could predict the pressure difference's affect on the performance.

Applying a different air temperature at the inlet than the outlet would only help to validate the numerical model for that range. As it is, the current experimental setup by having the bottom ledge preheating the air, allowed having a different inlet and outlet temperature. The numerical model was validated with this. So in essence varying the inlet temperature compared outlet as already been done, however the range was very limited. As mentioned before the effect on the mass flow of this air temperature difference as well as the effect of the geometry are going to be swamped by external pressure forces.

Appendices

8.1 Appendix A - Velocity Measurement Conversion

The conversion from voltage to velocity is based on the Log Square transfer function.

$$LSQ = \ln^2(1 + gV)$$

Where g is the gain factor optimized for a specific probe type. For the omnidirecitonal probe, g is set as 150.

$$LSQ = A_0 + A_1 e + A_2 e^2 + A_3 e^3 + ..$$

Where A values are found from the manufacturer provided calibration, and e is the measured voltage. The resulting equation can then be written.

$$V_e = \left[exp\left((A_0 + A_1 e + A_2 e^2 + A_3 e^3 + ..)^{1/2}\right)\right]/g$$

The pressure is then accounted for by the following.

$$V_p = V \frac{p}{101.325\ kPa}$$

Where p is the measured atmospheric pressure. The correction for humidity and temperature is finally applied.

$$V = V_p \left(1 + f\left(r \times f(T)\right)\right)$$

Where f is a manufacturer provided calibration function for the respective values, r is the relative humidity and T is the measured temperature. This will result in an instantaneous velocity reading. To account for the turbulent nature of the flow many in instantaneous voltage readings need to be taken, and converted to velocity, then averaged to get a mean velocity reading at that location.

8.2 Appendix B - Pyranometer Readings

The following shows the pyranometer readings with the coordinates zero and zero referring to the location centered between the vertical height and horizontal width between the four bulbs. Two set ups, seen in Figure 8.1 and 8.2, had a smaller spacing between measurements used for the horizontal center line readings to see if there was variations from the courser gird. Figure 8.2 shows the decrease in the measured heat flux due to the shading caused by the thermocouple wire used to measured the surface temperature of the glass. This shows that there could be differences between what is measured in the courser grid and the actual heat flux on the surface. The occasional reading for the behind glass measurements that is well below the rest of the readings is attributed to shading from the thermocouple wire. The heat flux on the bottom ledge was also measured on a center line and can be seen in Figure 8.9.

Table 8.1: Pyranometer readings (W/m^2) on outside of glass for L = 1 m

Spacing (in)	14	10.5	7	3.5	0	-3.5	-7	-10.5	-14
17.5		427	469	516	526	527	482	438	
14	442	467	509	568	572	570	539	488	496
10.5	478	504	553	627	616	616	600	545	548
7	514	539	600	669	649	653	647	580	576
3.5	528	556	614	678	654	669	668	606	598
0	531	559	607	678	657	662	664	600	584
-3.5	512	545	584	666	647	646	652	597	568
-7	499	535	578	656	644	636	649	585	558
-10.5	467	510	542	630	617	611	618	552	525
-14	436	473	503	580	578	572	575	515	488
-17.5	405	433	464	532	543	524	547	483	459

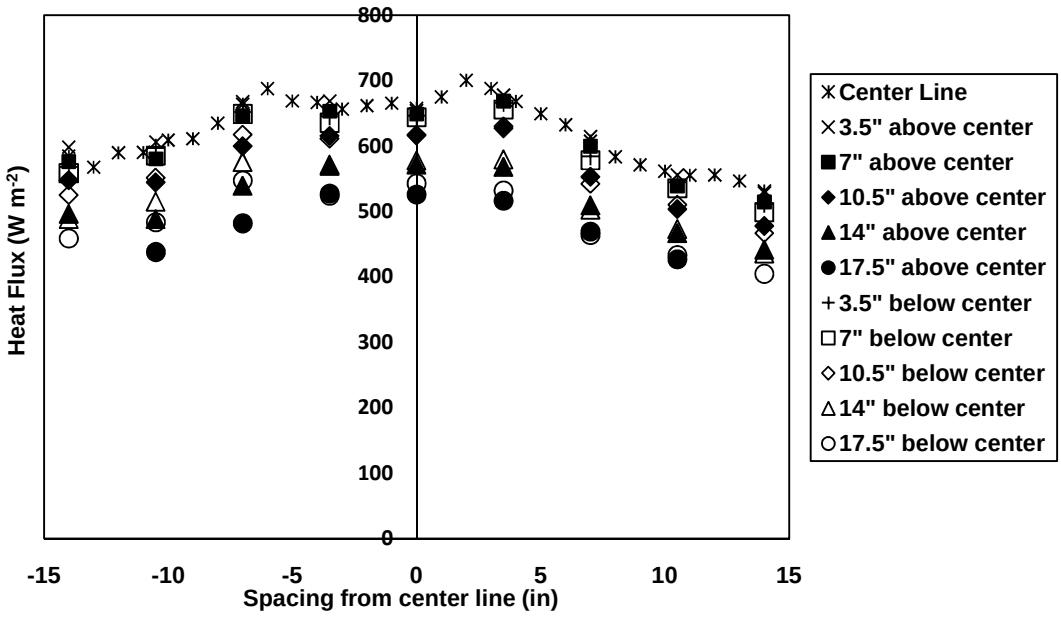

Figure 8.1: Pyranometer readings on outside of glass L = 1 m

Table 8.2: Pyranometer readings (W/m^2) 10 cm behind glass for L = 1 m

Spacing (in)	14	10.5	7	3.5	0	-3.5	-7	-10.5	-14
17.5	319	291	307	321	347	342	305	290	282
14	324	311	331	347	313	371	339	319	324
10.5	363	338	355	371	395	394	367	345	358
7	371	358	381	397	406	417	399	376	390
3.5	414	384	405	416	439	439	422	394	400
0	418	381	406	420	430	444	429	402	398
-3.5	420	380	408	427	449	446	435	406	381
-7	399	367	390	413	436	437	425	392	322
-10.5	387	356	374	400	424	431	419	384	367
-14	367	346	363	393	422	423	409	374	364
-17.5	207	319	349	364	368	410	390	360	323

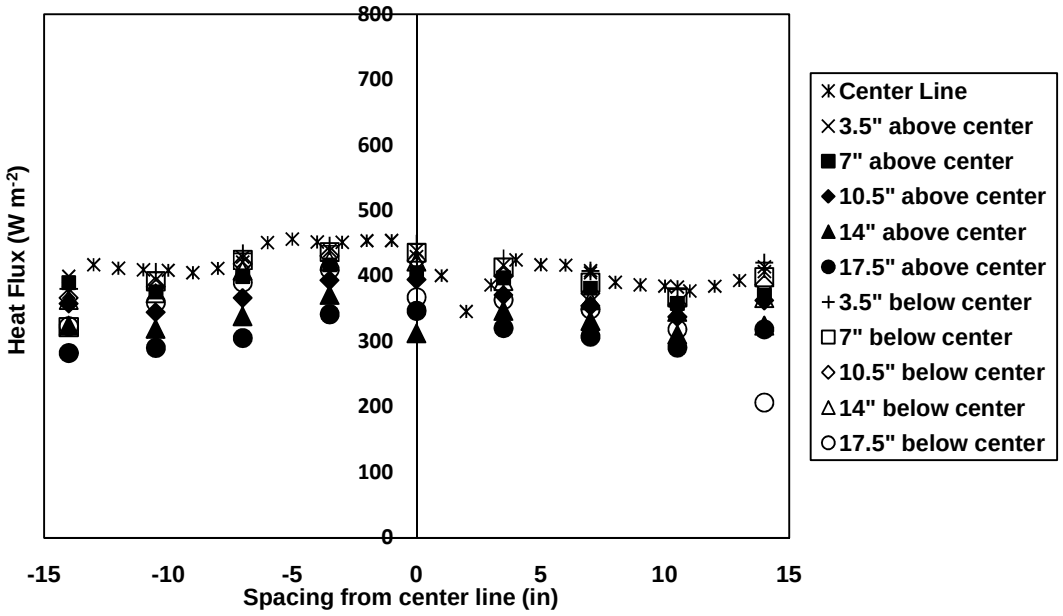

Figure 8.2: Pyranometer readings 10 cm behind glass for L = 1 m

Table 8.3: Pyranometer readings (W/m^2) 5 cm behind glass for L = 1 m

Spacing (in)	14	10.5	7	3.5	0	-3.5	-7	-10.5	-14
17.5	306	328	361	391	324	413	370	349	351
14	325	351	389	413	432	432	396	369	344
10.5	369	338	355	371	395	394	367	345	358
7	359	380	428	451	473	471	450	413	394
3.5	368	385	437	459	478	476	458	423	405
0	366	391	434	464	474	483	464	432	406
-3.5	345	381	410	448	465	464	451	414	388
-7	338	372	399	440	453	452	444	402	378
-10.5	321	352	385	422	437	438	427	382	248
-14	313	334	362	394	410	409	397	353	313
-17.5	290	306	338	369	392	383	376	331	320

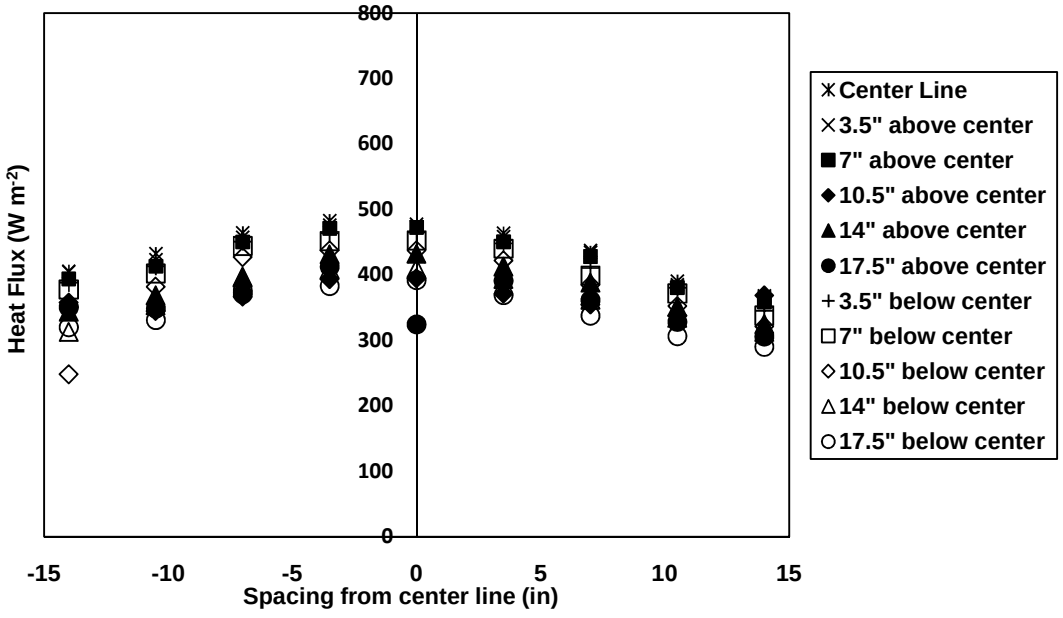

Figure 8.3: Pyranometer readings 5 cm behind glass for L = 1 m

Table 8.4: Pyranometer readings (W/m^2) 15 cm behind glass for L = 1 m

Spacing (in)	14	10.5	7	3.5	0	-3.5	-7	-10.5	-14
17.5	273	293	308	325	363	364	326	305	296
14	297	324	344	358	386	384	348	326	314
10.5	304	335	356	370	395	399	375	343	336
7	314	346	370	384	415	416	392	358	358
3.5	322	345	373	382	360	416	396	369	358
0	318	342	373	360	420	420	398	369	357
-3.5	310	330	362	343	413	411	390	359	352
-7	299	320	355	331	400	402	381	344	339
-10.5	287	309	347	325	394	393	369	329	328
-14	274	295	323	270	361	374	353	313	309
-17.5	265	287	308	282	357	357	338	304	294

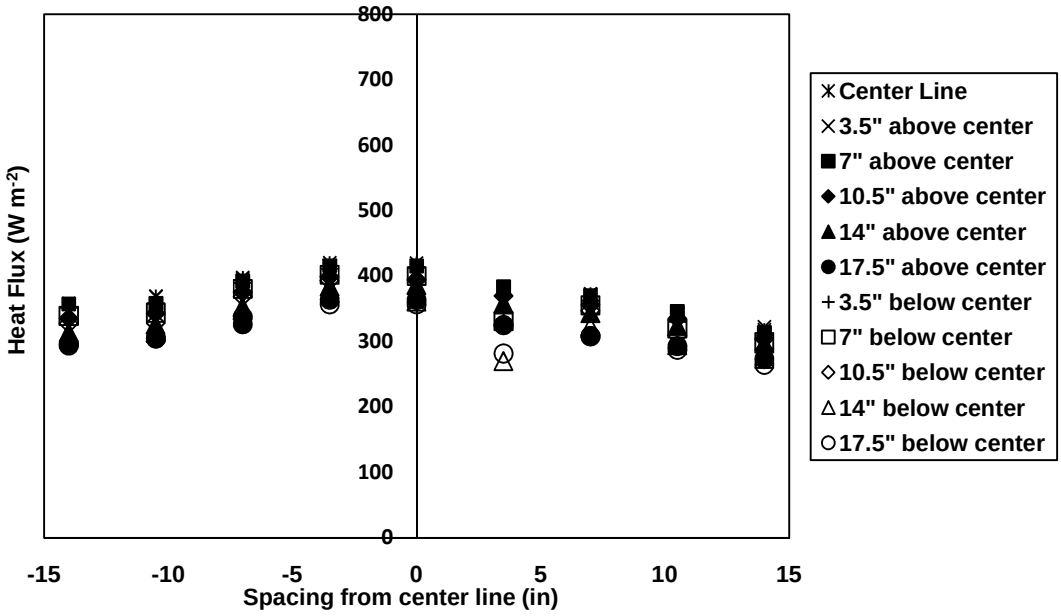

Figure 8.4: Pyranometer readings 15 cm behind glass for L = 1 m

Table 8.5: Pyranometer readings (W/m^2) on outside of glass for L = 1.38 m

Spacing (in)	14	10.5	7	3.5	0	-3.5	-7	-10.5	-14
17.5		284	299	320	363	355	315	285	
14	284	305	321	341	381	379	339	305	310
10.5	282	312	328	339	390	391	352	317	317
7	305	323	335	343	392	394	354	331	334
3.5	312	331	342	352	398	400	367	329	336
0	313	337	353	363	408	406	379	339	345
-3.5	302	319	338	349	394	393	362	320	324
-7	290	305	329	341	382	388	357	317	320
-10.5	282	301	323	335	376	380	352	308	302
-14	268	288	308	322	363	363	337	293	290
-17.5	264	283	300	311	345	353	324	280	280

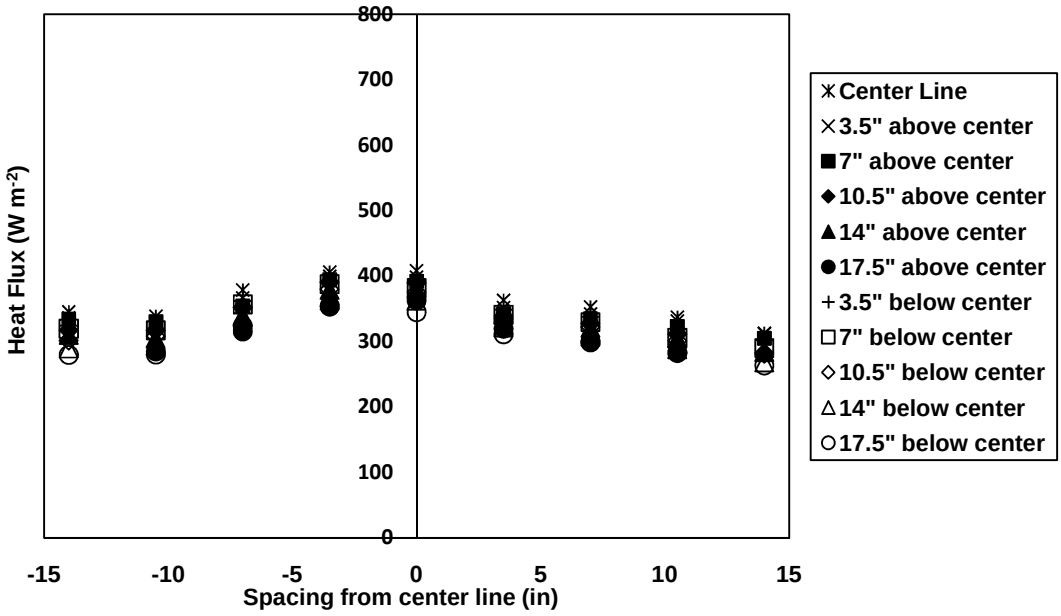

Figure 8.5: Pyranometer readings on outside of glass for L = 1.38 m

Table 8.6: Pyranometer readings (W/m^2) 10 cm behind glass for L = 1.38 m

Spacing (in)	14	10.5	7	3.5	0	-3.5	-7	-10.5	-14
17.5	201	209	216	225	226	266	237	212	200
14	207	214	223	229	262	269	238	212	202
10.5	214	218	225	229	214	271	244	220	208
7	218	224	231	236	271	279	254	225	217
3.5	220	228	237	240	272	284	259	231	223
0	223	233	241	245	279	289	263	236	228
-3.5	216	228	238	245	280	284	262	231	224
-7	207	221	231	239	271	277	253	223	217
-10.5	200	214	224	232	264	272	252	218	211
-14	194	208	218	227	258	266	246	209	205
-17.5	184	198	212	219	250	258	238	204	198

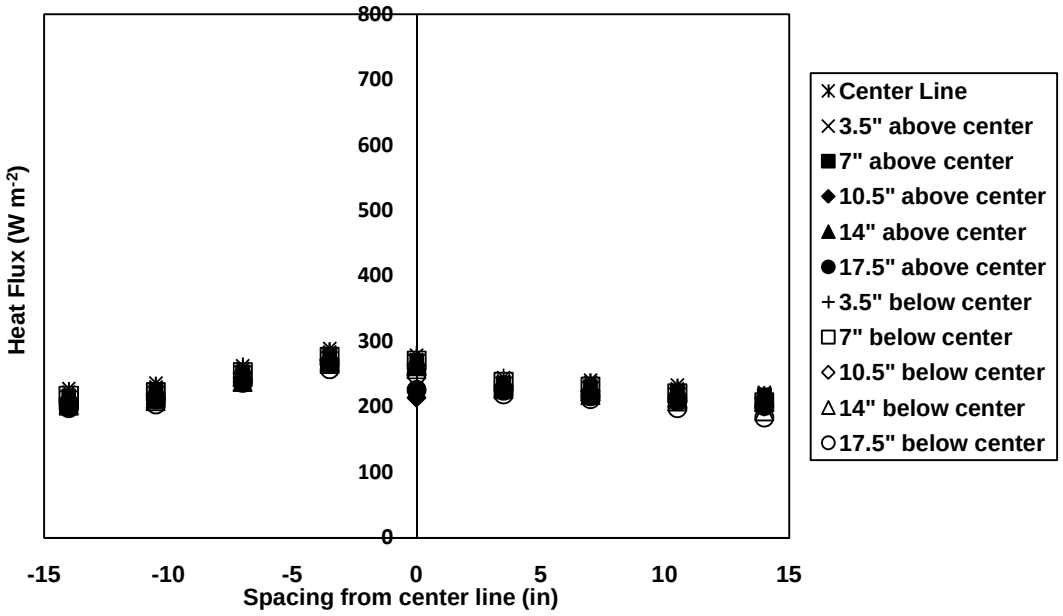

Figure 8.6: Pyranometer readings 10 cm behind glass for L = 1.38 m

Table 8.7: Pyranometer readings (W/m^2) 5 cm behind glass for L = 1.38 m

Spacing (in)	14	10.5	7	3.5	0	-3.5	-7	-10.5	-14
17.5	218	227	234	242	238	287	254	227	220
14	221	229	241	246	279	287	256	228	218
10.5	227	234	243	248	266	290	261	234	226
7	229	239	247	248	285	296	271	243	235
3.5	231	243	252	253	288	300	273	245	237
0	232	246	255	258	290	303	279	249	242
-3.5	226	241	250	255	293	298	274	244	238
-7	219	231	243	252	286	290	268	236	230
-10.5	211	222	238	244	280	286	264	229	204
-14	203	218	232	236	271	279	254	220	210
-17.5	196	211	224	229	263	270	247	215	209

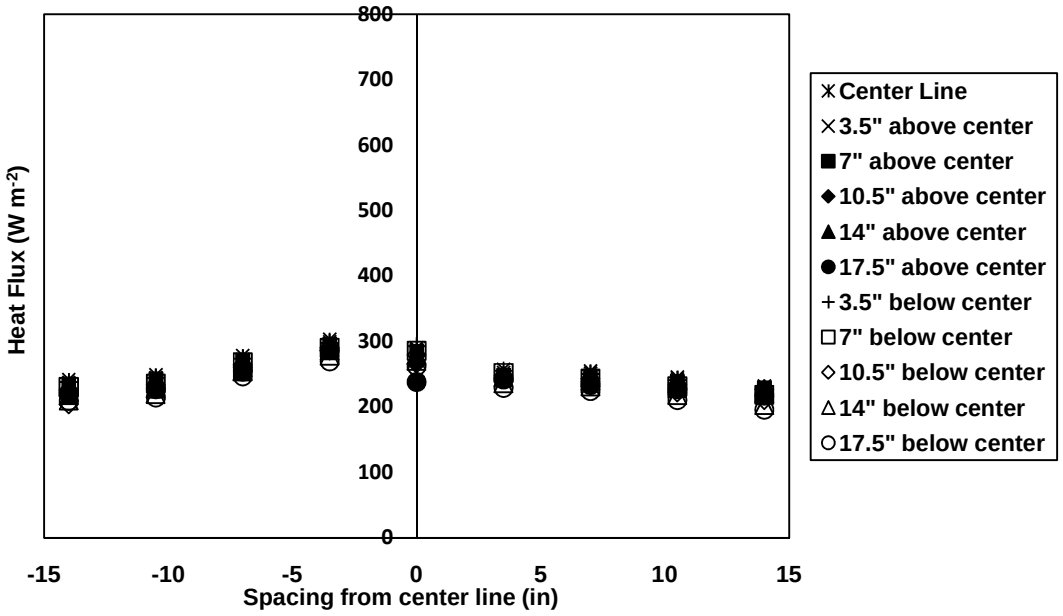

Figure 8.7: Pyranometer readings 5 cm behind glass for L = 1.38 m

Table 8.8: Pyranometer readings (W/m^2) 15 cm behind glass for L = 1.38 m

Spacing (in)	14	10.5	7	3.5	0	-3.5	-7	-10.5	-14
17.5	189	190	201	212	209	246	220	197	188
14	197	204	211	220	246	257	228	204	194
10.5	202	207	212	219	242	261	236	211	202
7	211	217	222	227	258	268	244	218	209
3.5	218	221	228	232	263	273	252	223	217
0	221	225	233	236	270	279	254	227	222
-3.5	208	215	223	229	266	271	248	220	213
-7	206	209	219	225	260	265	243	214	208
-10.5	196	204	213	221	255	260	241	208	204
-14	188	196	206	212	246	252	237	203	198
-17.5	181	192	202	204	240	245	227	195	191

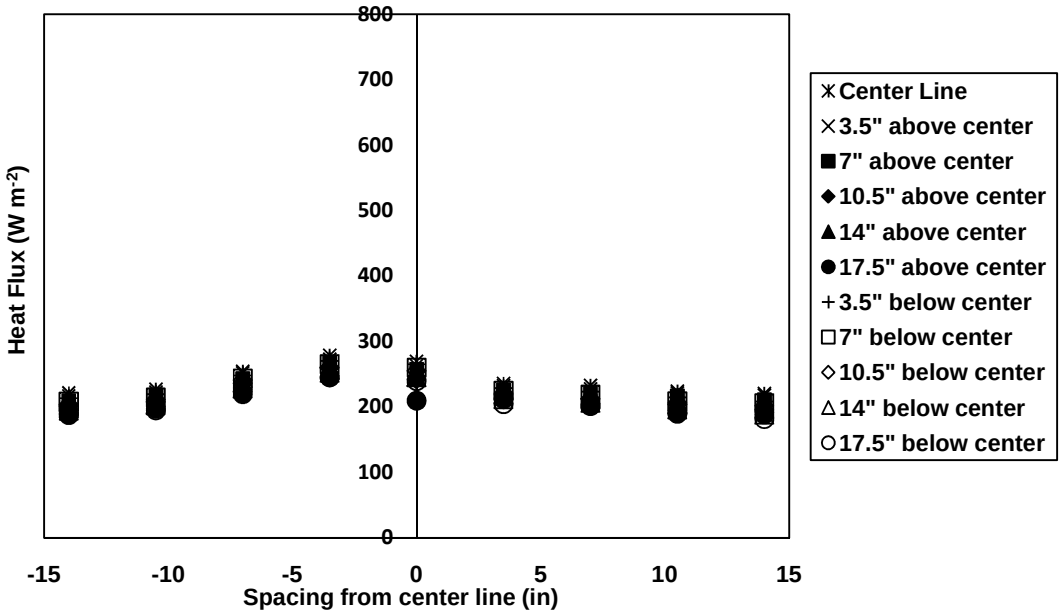

Figure 8.8: Pyranometer readings 15 cm behind glass for L = 1.38 m

Table 8.9: Pyranometer readings on horizontal center line on bottom ledge

Spacing from front of illumination system (cm)	Heat flux measured (W/m^2)
65	337
70	343
75	333
80	310
85	287
90	264
95	244
100	223
105	207
110	191
115	172
120	160
125	149
130	135
135	127
140	117
145	108
150	101
155	95

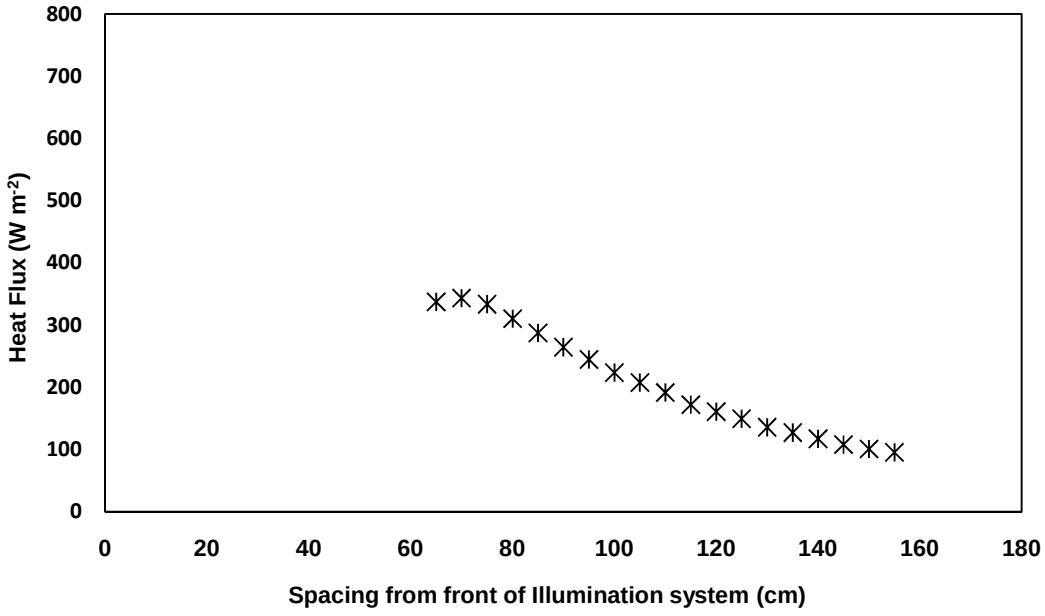

Figure 8.9: Pyranometer readings on horizontal center line on bottom ledge

8.3 Appendix C - Two Dimensional Mesh Visualization

The following figure represents the mesh used in the numerical model.

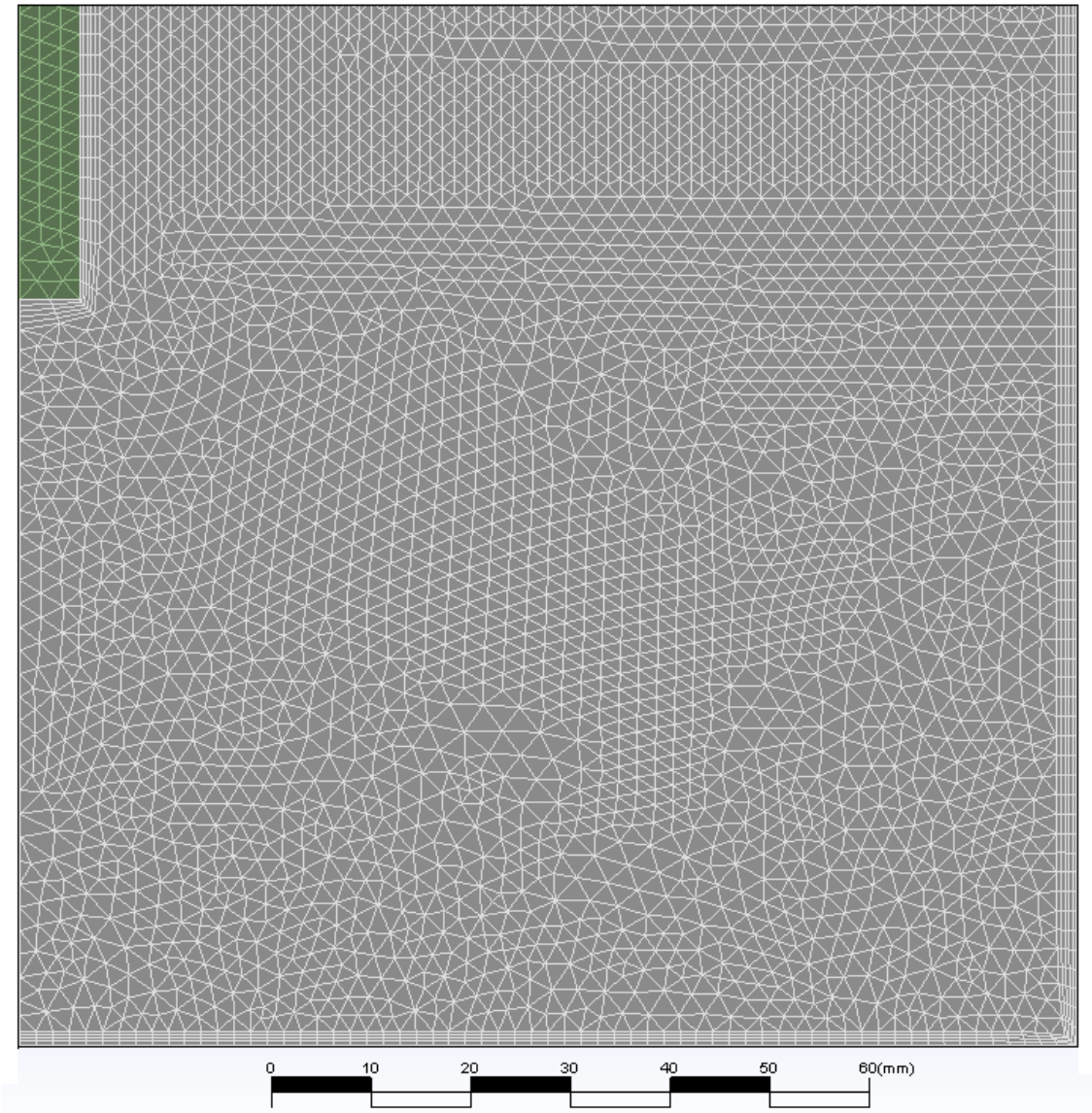

Figure 8.10: Mesh at inlet for Experiment 2, 180,000 nodes

8.4 Appendix D - Numerical Results

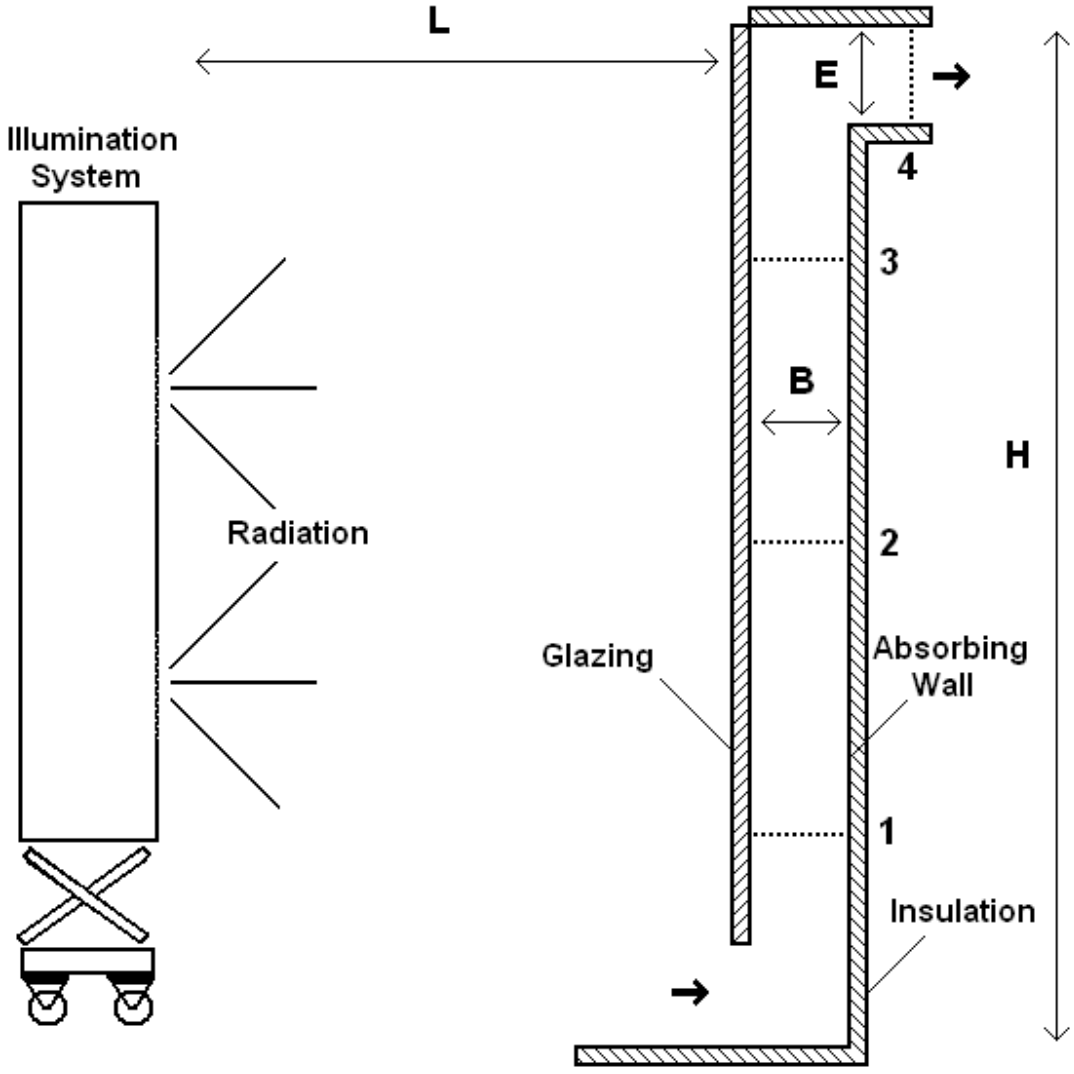

Figure 8.11: Experimental Setup

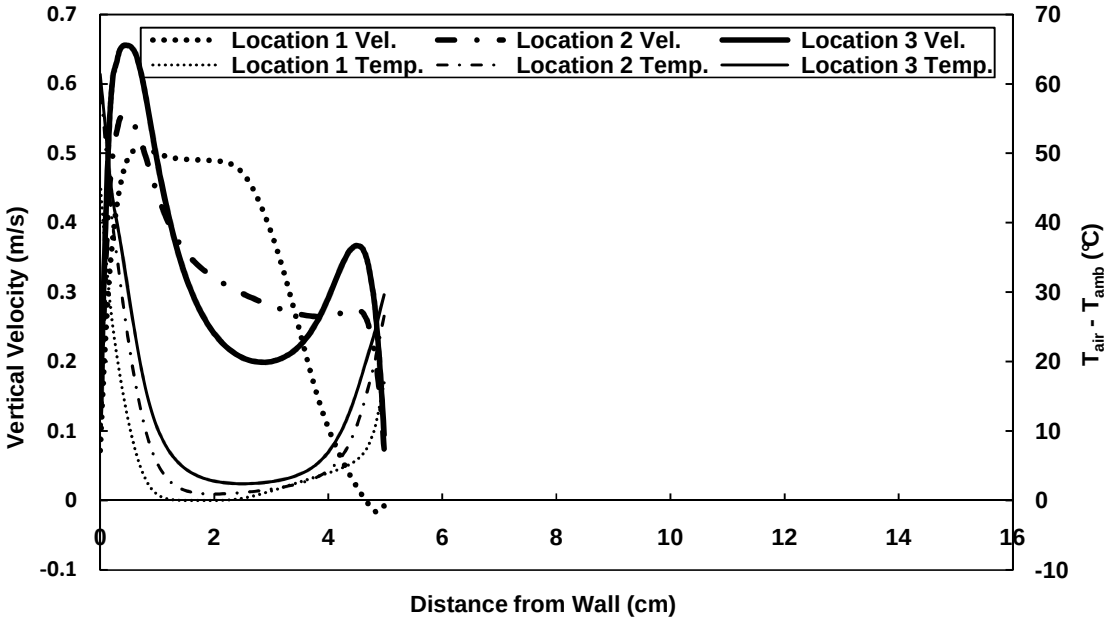

Figure 8.12: Numerical horizontal velocity and temperature profiles for Experiment 1, B/H = 0.044, outside vertical center average heat flux = 600 W/m^2, $T_{inlet} = T_{ambient}$

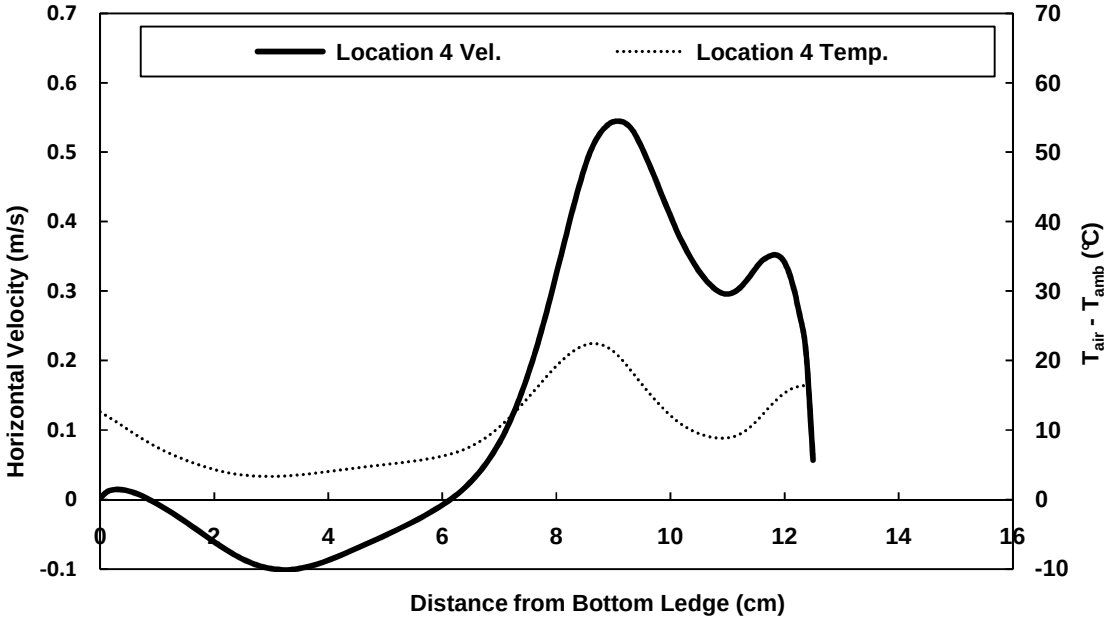

Figure 8.13 Numerical vertical velocity and temperature profiles for Experiment 1, B/H = 0.044, outside vertical center average heat flux = 600 W/m^2, $T_{inlet} = T_{ambient}$

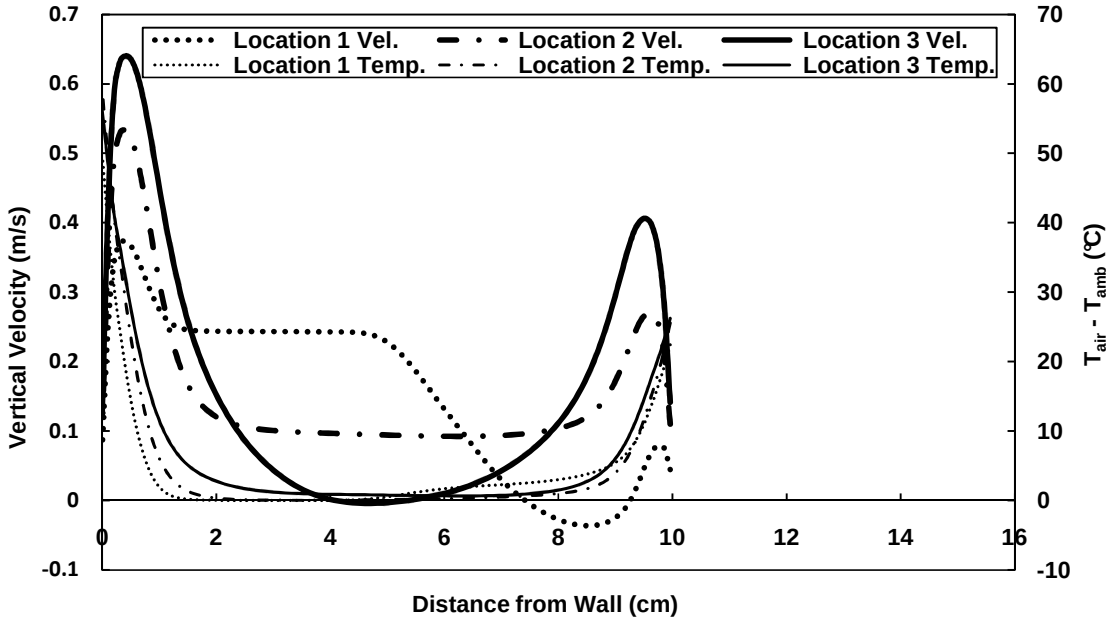

Figure 8.14: Numerical horizontal velocity and temperature profiles for Experiment 2, B/H = 0.089, outside vertical center average heat flux = 600 W/m^2, $T_{inlet} = T_{ambient}$

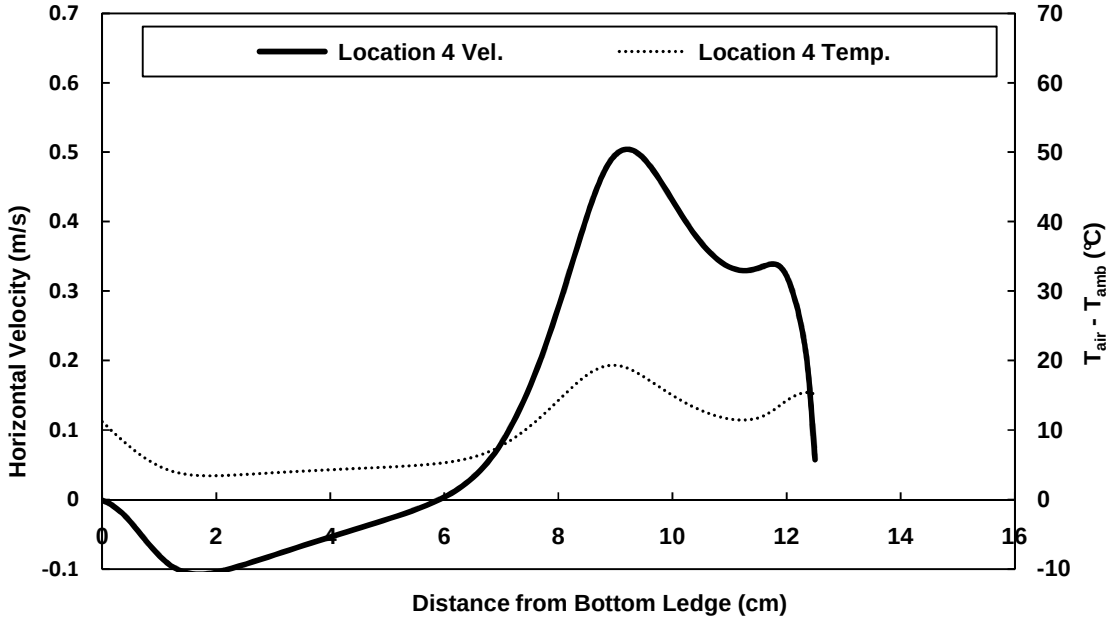

Figure 8.15 Numerical vertical velocity and temperature profiles for Experiment 2, B/H = 0.089, outside vertical center average heat flux = 600 W/m^2, $T_{inlet} = T_{ambient}$

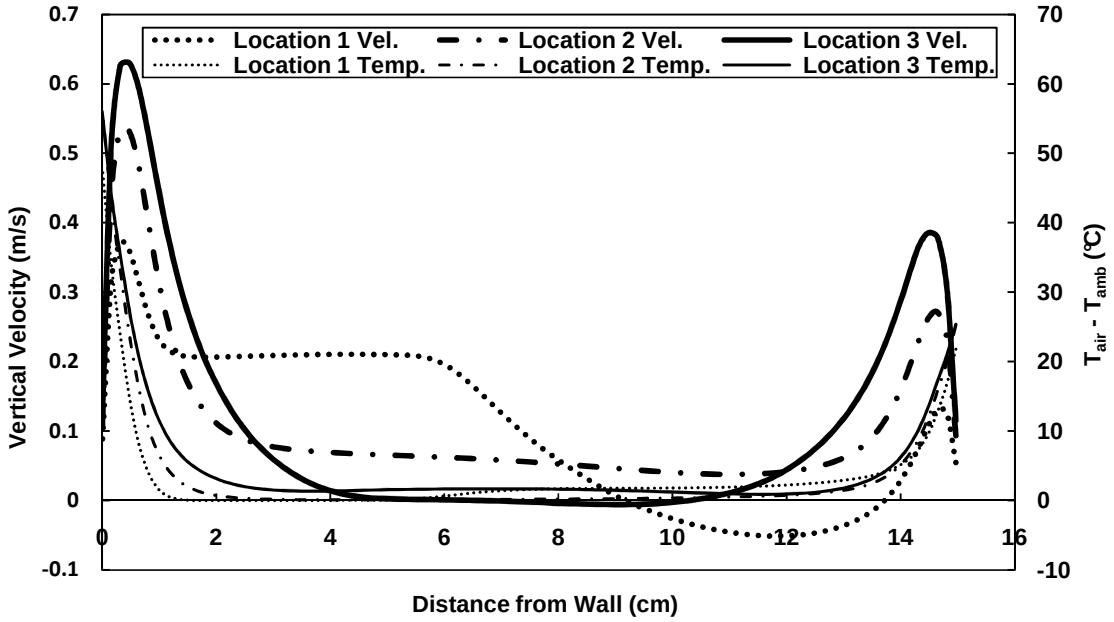

Figure 8.16: Numerical horizontal velocity and temperature profiles for Experiment 3, B/H = 0.133, outside vertical center average heat flux = 600 W/m^2, $T_{inlet} = T_{ambient}$

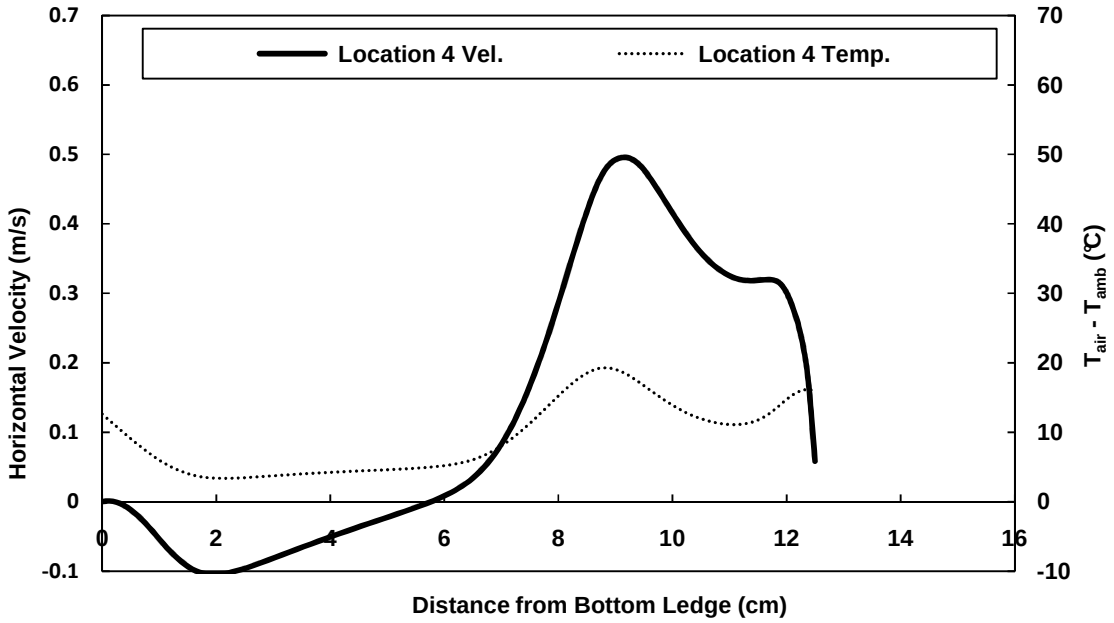

Figure 8.17 Numerical vertical velocity and temperature profiles for Experiment 3, B/H = 0.133, outside vertical center average heat flux = 600 W/m^2, $T_{inlet} = T_{ambient}$

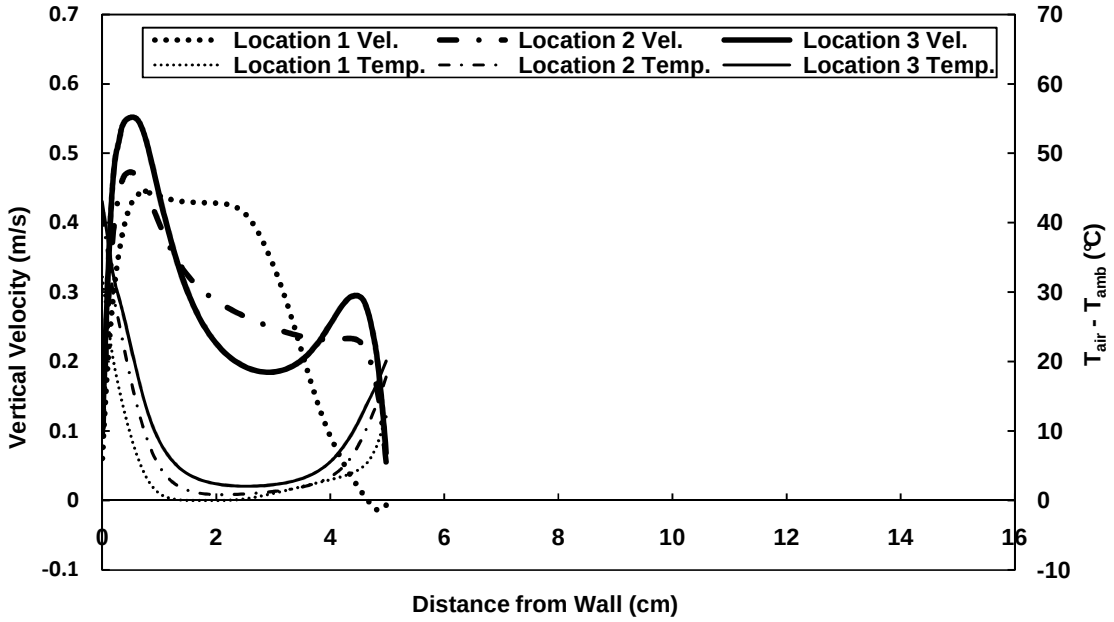

Figure 8.18: Numerical horizontal velocity and temperature profiles for Experiment 4, B/H = 0.044, outside vertical center average heat flux = 380 W/m^2, $T_{inlet} = T_{ambient}$

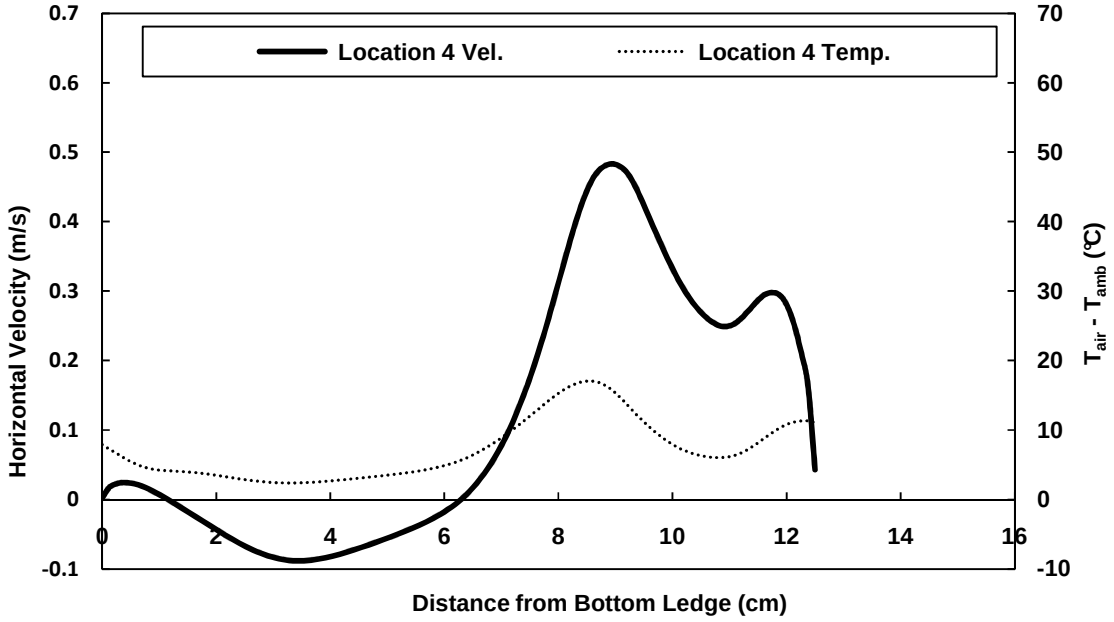

Figure 8.19 Numerical vertical velocity and temperature profiles for Experiment 4, B/H = 0.044, outside vertical center average heat flux = 380 W/m^2, $T_{inlet} = T_{ambient}$

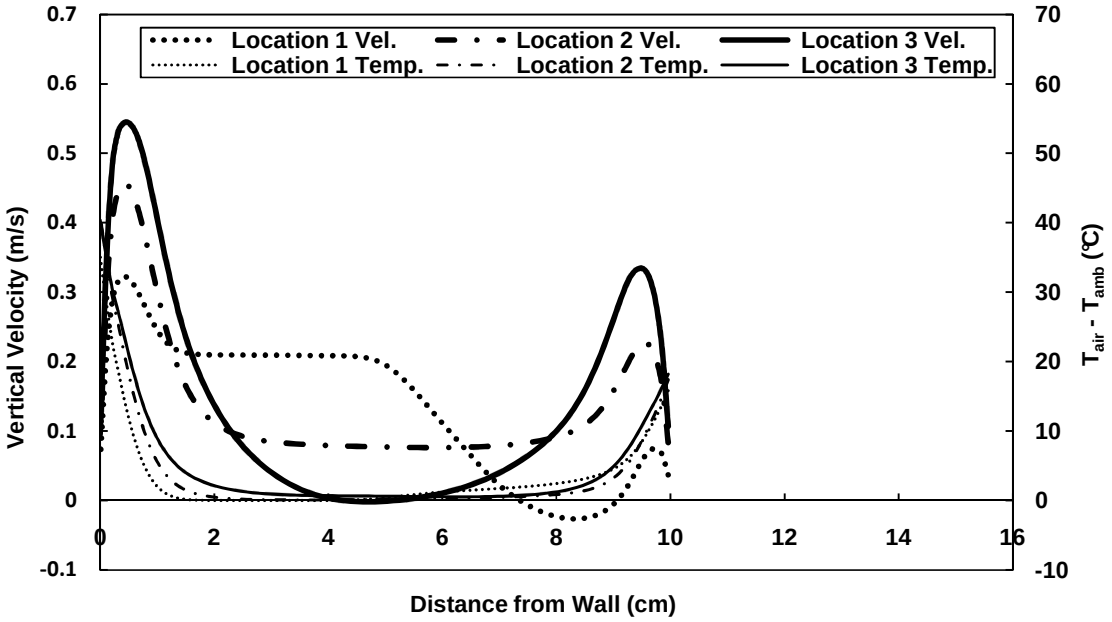

Figure 8.20: Numerical horizontal velocity and temperature profiles for Experiment 5, B/H = 0.089, outside vertical center average heat flux = 380 W/m^2, $T_{inlet} = T_{ambient}$

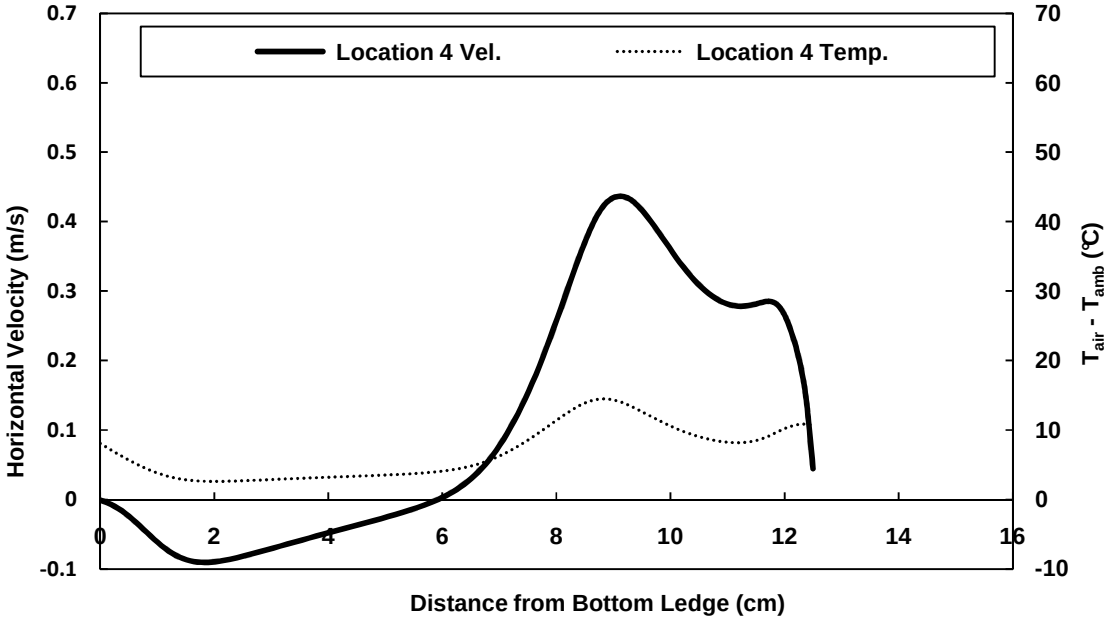

Figure 8.21 Numerical vertical velocity and temperature profiles for Experiment 5, B/H = 0.089, outside vertical center average heat flux = 380 W/m^2, $T_{inlet} = T_{ambient}$

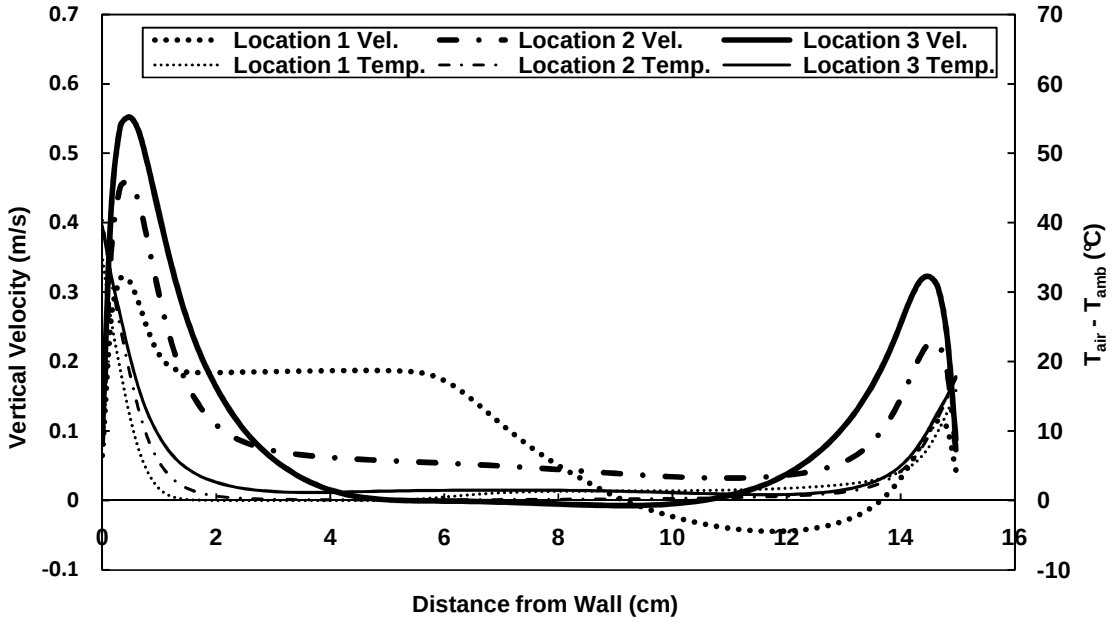

Figure 8.22: Numerical horizontal velocity and temperature profiles for Experiment 6, B/H = 0.133, outside vertical center average heat flux = 380 W/m^2, $T_{inlet} = T_{ambient}$

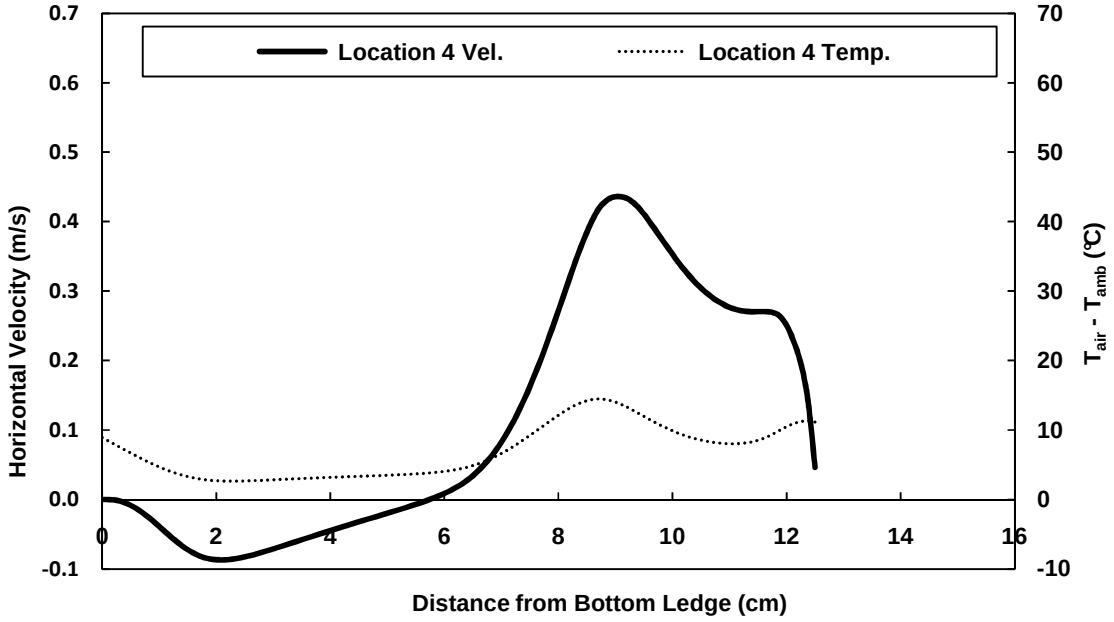

Figure 8.23 Numerical vertical velocity and temperature profiles for Experiment 6, B/H = 0.133, outside vertical center average heat flux = 380 W/m^2, $T_{inlet} = T_{ambient}$

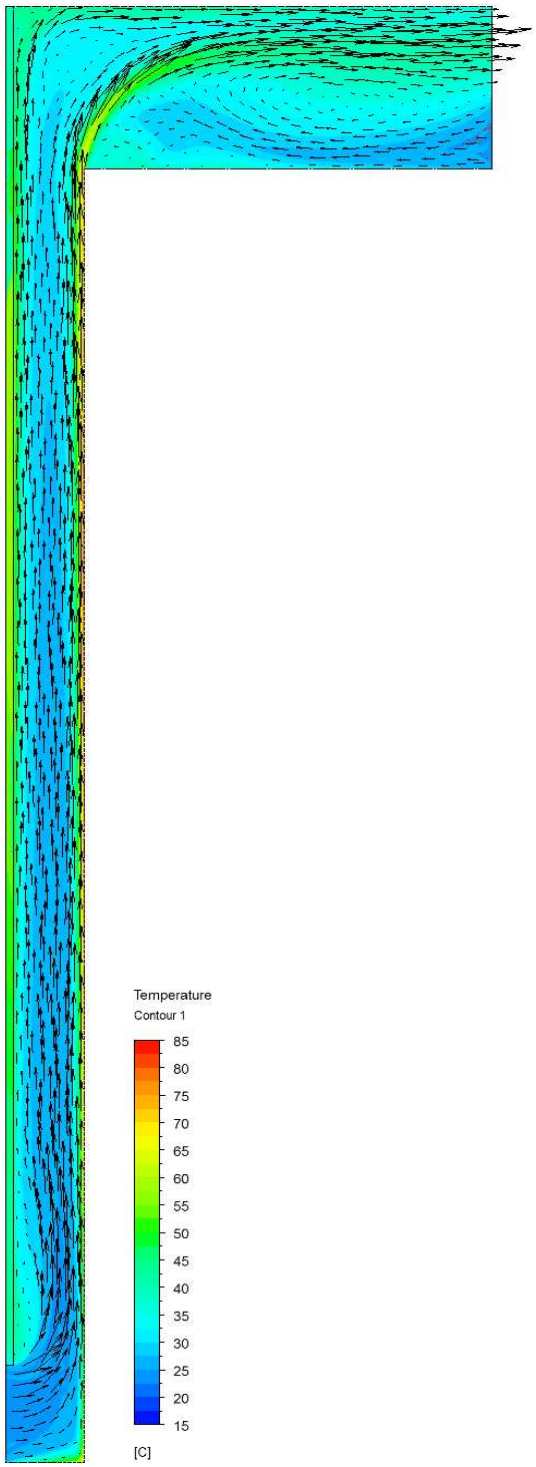

Figure 8.24: Numerical velocity vectors on top of temperature contour plot for Experiment 1, $T_{inlet} = T_{ambient}$

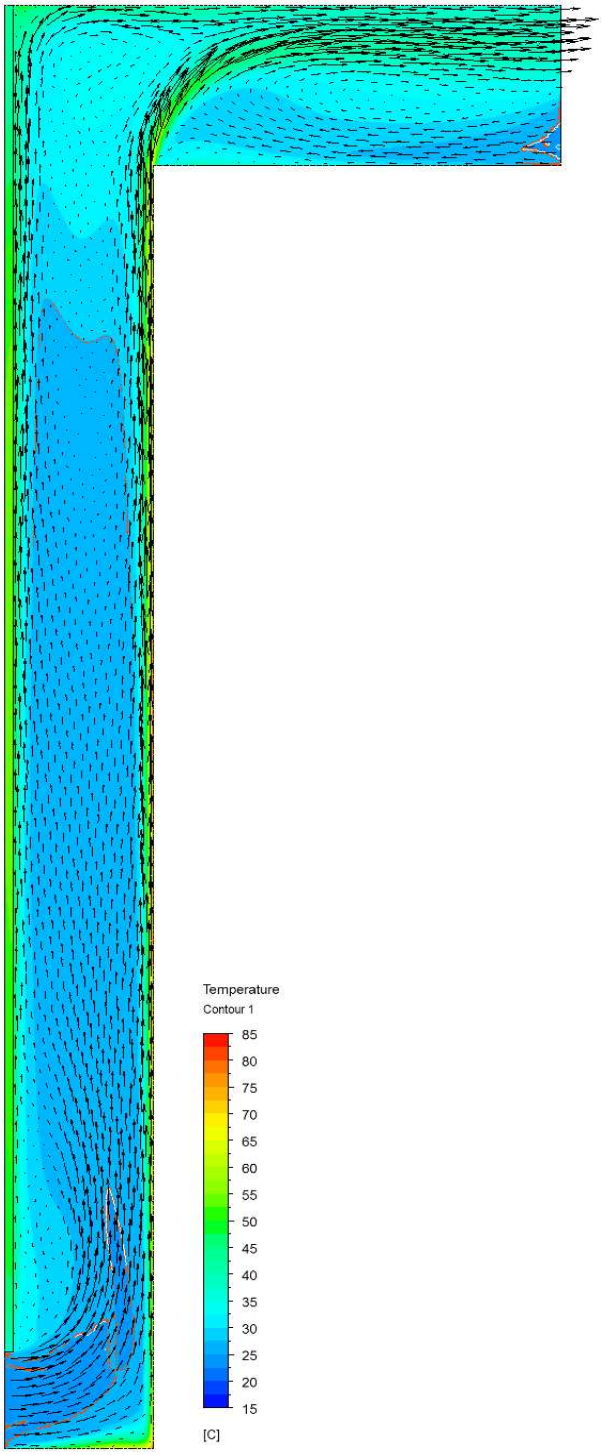

Figure 8.25: Numerical velocity vectors on top of temperature contour plot for Experiment 2, $T_{inlet} = T_{ambient}$

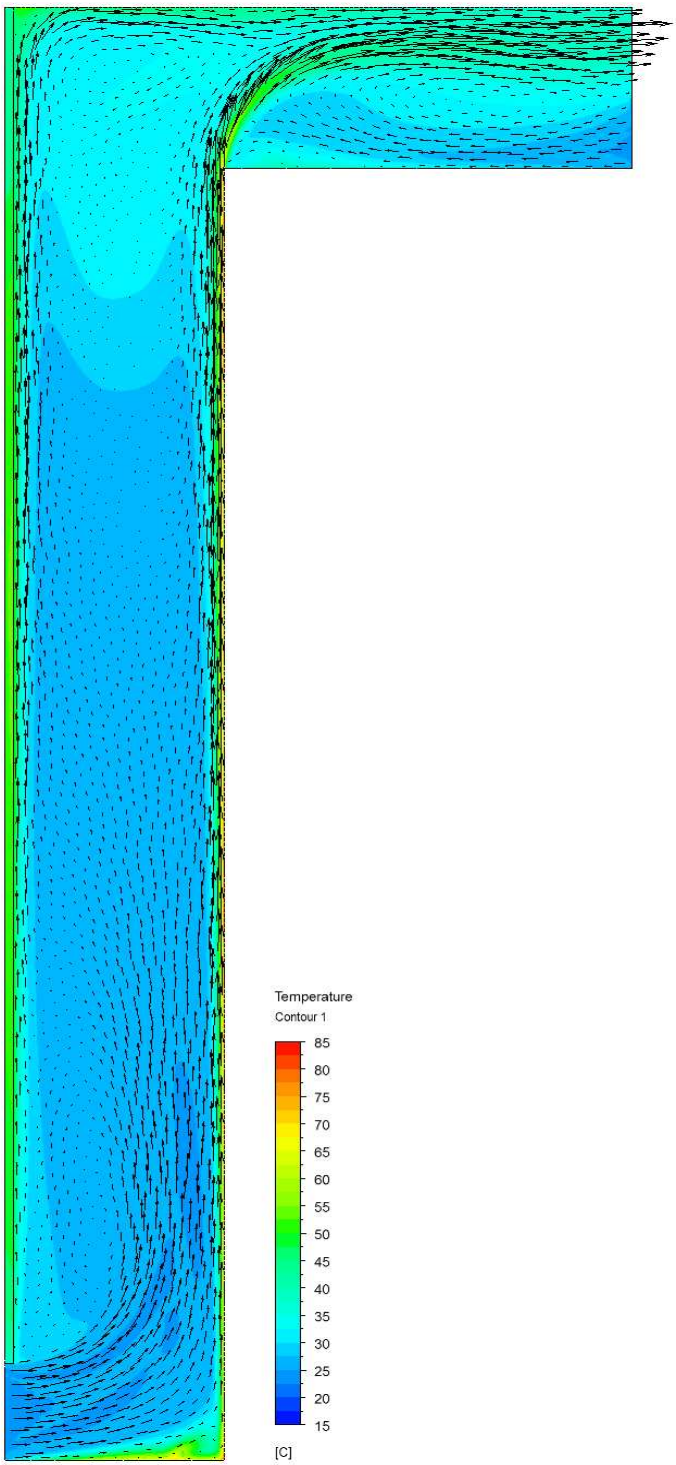

Figure 8.26: Numerical velocity vectors on top of temperature contour plot for Experiment 3, $T_{inlet} = T_{ambient}$

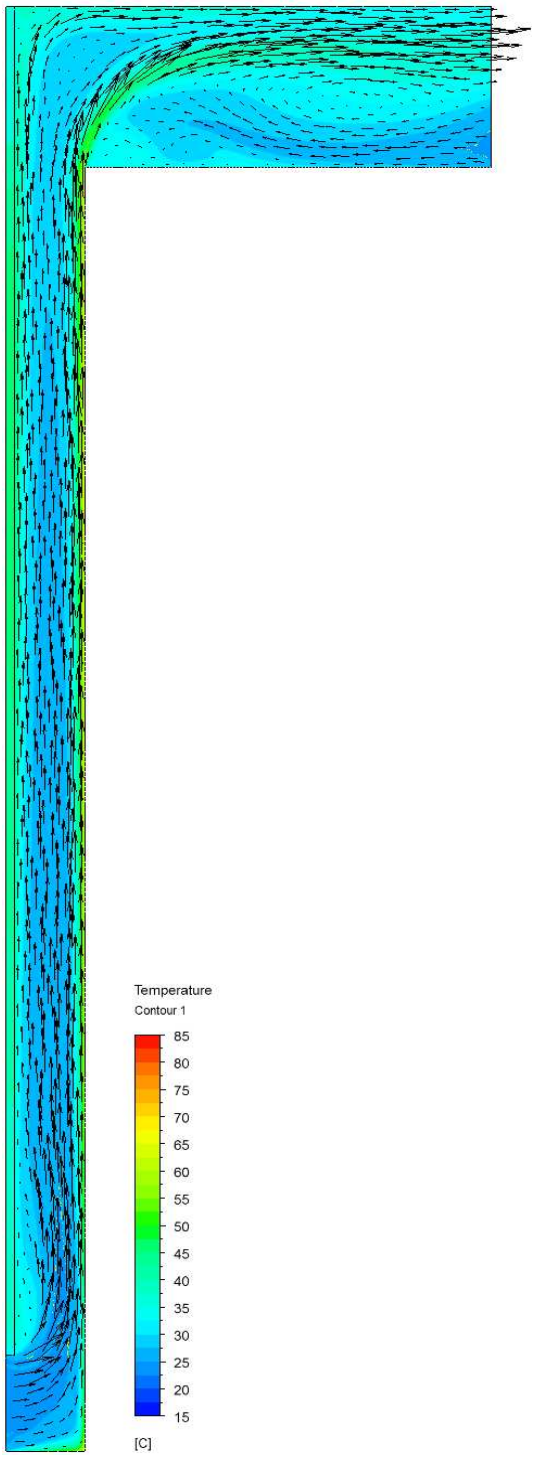

Figure 8.27: Numerical velocity vectors on top of temperature contour plot for Experiment 4, $T_{inlet} = T_{ambient}$

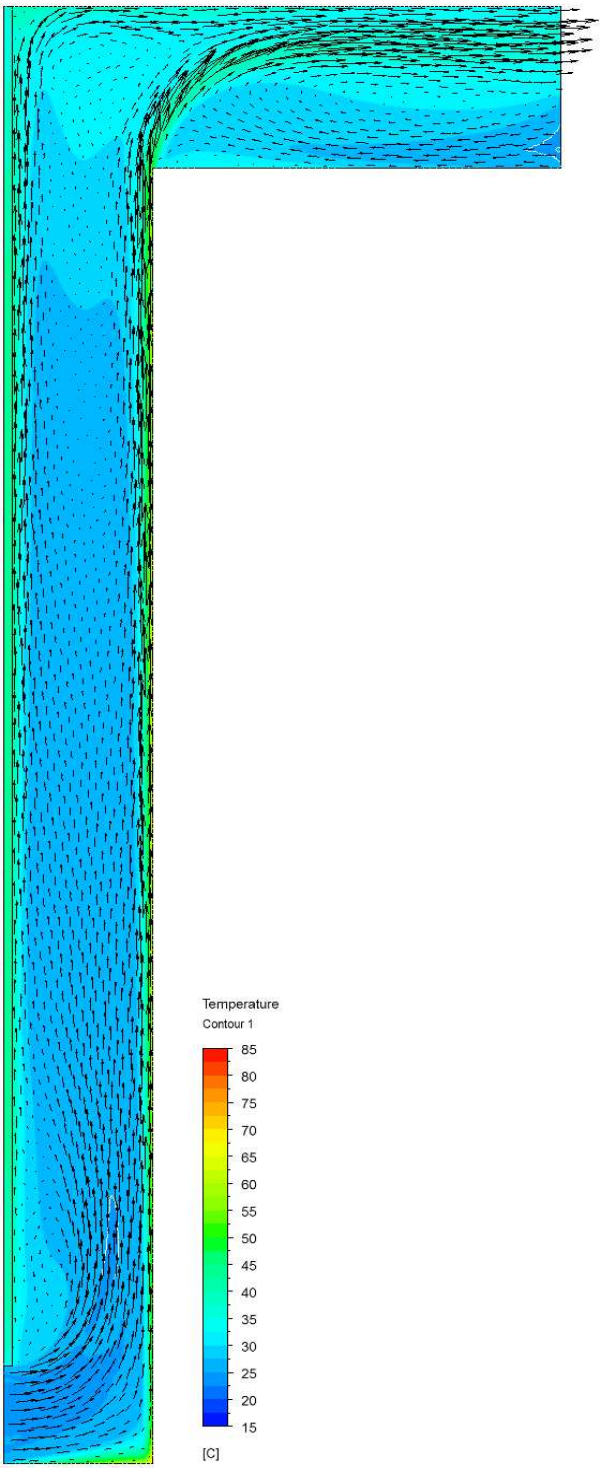

Figure 8.28: Numerical velocity vectors on top of temperature contour plot for Experiment 5, $T_{inlet} = T_{ambient}$

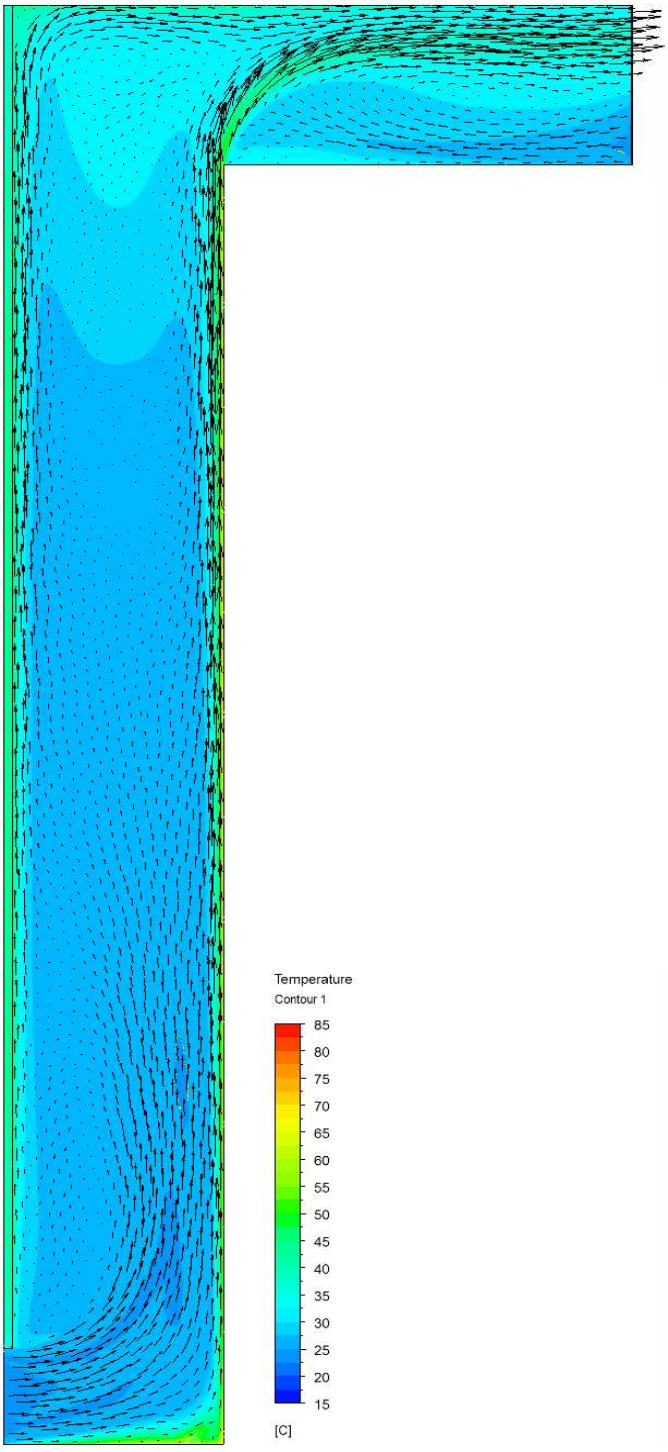

Figure 8.29: Numerical velocity vectors on top of temperature contour plot for Experiment 6, $T_{inlet} = T_{ambient}$

References

ASHRAE. 2007. Standard 62.1 - 2007: Ventilation for Acceptable Indoor Air Quality. American Society of Heating, Refrigerating and Air-conditioning Engineers Inc.

ASHRAE. 2009. *2009 ASHRAE Handbook - Fundamentals*. Atlanta, GA: American Society of Heating, Refrigerating and Air-conditioning Engineers Inc.

Ayinde, T. F., S. A. M. Said & M. A. Habib (2006) Experimental investigation of turbulent natural convection flow in a channel. *Heat and Mass Transfer,* 42**,** 169-177.

Badr, H. M., M. A. Habib, S. Anwar, R. Ben-Mansour & S. A. M. Said (2006) Turbulent natural convection in vertical parallel-plate channels. *Heat and Mass Transfer,* 43**,** 73-84.

Bouchair, A. 1994. Solar chimney for promoting cooling ventilation in southern Algeria. 81–93. Building Services Engineering Research and Technology.

Burek, S. A. M. & A. Habeb (2007) Air flow and thermal efficiency characteristics in solar chimneys and Trombe Walls. *Energy and Buildings,* 39**,** 128-135.

Natural Resources Canada, N. R. 2008. Energy Use Data Handbook. ed. O. o. E. Efficiency. Ottawa.

Chen, Z. D., P. Bandopadhayay, J. Halldorsson, C. Byrjalsen, P. Heiselberg & Y. Li (2003) An experimental investigation of a solar chimney model with uniform wall heat flux. *Building and Environment,* 38**,** 893-906.

da Silva, A. K. & L. Gosselin (2005) Optimal geometry of L and C-shaped channels for maximum heat transfer rate in natural convection. *International Journal of Heat and Mass Transfer,* 48**,** 609-620.

Duffie, J. A. & W. A. Beckman. 1974. *Solar Energy Thermal Processes*. New York, NY: John Wiley and Sons.

Fedorov, A. G. & R. Viskanta (1997) Turbulent natural convection heat transfer in an asymmetrically heated, vertical parallel-plate channel. *International Journal of Heat and Mass Transfer,* 40**,** 3849-3860.

Gan, G. H. (2006) Simulation of buoyancy-induced flow in open cavities for natural ventilation. *Energy and Buildings,* 38**,** 410-420.

Hernandez, V., D. Morillon, R. Best, J. Fernandez, R. Almanza & N. Chargoy (2006) Experimental and numerical model of wall like solar heat discharge passive system. *Applied Thermal Engineering,* 26**,** 2464-2469.

Lapica, A., G. Rodono & R. Volpes (1993) AN EXPERIMENTAL INVESTIGATION ON NATURAL-CONVECTION OF AIR IN A VERTICAL CHANNEL. *International Journal of Heat and Mass Transfer,* 36**,** 611-616.

Menter, F. R. (1994) 2-EQUATION EDDY-VISCOSITY TURBULENCE MODELS FOR ENGINEERING APPLICATIONS. *Aiaa Journal,* 32**,** 1598-1605.

Onbasioglu, H. & A. N. Egrican (2002) Experimental approach to the thermal response of passive systems. *Energy Conversion and Management,* 43**,** 2053-2065.

Ryan, D. & S. A. M. Burek (2010) Experimental study of the influence of collector height on the steady state performance of a passive solar air heater. *Solar Energy,* 84**,** 1676-1684.

Zamora, B. & A. S. Kaiser (2009) Optimum wall-to-wall spacing in solar chimney shaped channels in natural convection by numerical investigation. *Applied Thermal Engineering,* 29**,** 762-769.

Zamora, B. & A. S. Kaiser (2010) Thermal and dynamic optimization of the convective flow in Trombe Wall shaped channels by numerical investigation. *Heat and Mass Transfer,* 45**,** 1393-1407.